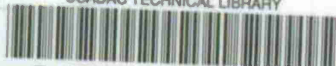


AD-A026871

USADAC TECHNICAL LIBRARY



5 0712 01016788 9

AD A 026871

TECHNICAL LIBRARY

TECHNICAL REPORT RL-76-18

QUANTIFICATION OF FLAWS IN FIBERED COMPOSITE STRUCTURES USING INTERFEROMETRIC FRINGE PATTERNS

B. R. Mullinix
Ground Equipment and Materials Directorate
US Army Missile Research, Development and Engineering Laboratory
US Army Missile Command
Redstone Arsenal, Alabama 35809

W. F. Ranson and W. F. Swinson
Auburn University
Auburn, Alabama

T. L. Cost
University of Alabama
University, Alabama

20 April 1976

Approved for public release; distribution unlimited.



U.S. ARMY MISSILE COMMAND

Redstone Arsenal, Alabama 35809

DISPOSITION INSTRUCTIONS

DESTROY THIS REPORT WHEN IT IS NO LONGER NEEDED. DO NOT RETURN IT TO THE ORIGINATOR.

DISCLAIMER

THE FINDINGS IN THIS REPORT ARE NOT TO BE CONSTRUED AS AN OFFICIAL DEPARTMENT OF THE ARMY POSITION UNLESS SO DESIGNATED BY OTHER AUTHORIZED DOCUMENTS.

TRADE NAMES

USE OF TRADE NAMES OR MANUFACTURERS IN THIS REPORT DOES NOT CONSTITUTE AN OFFICIAL INDORSEMENT OR APPROVAL OF THE USE OF SUCH COMMERCIAL HARDWARE OR SOFTWARE.

UNCLASSIFIED

SECURITY CLASSIFICATION OF THIS PAGE (When Data Entered)

REPORT DOCUMENTATION PAGE		READ INSTRUCTIONS BEFORE COMPLETING FORM
1. REPORT NUMBER RL-76-18	2. GOVT ACCESSION NO.	3. RECIPIENT'S CATALOG NUMBER
4. TITLE (and Subtitle) QUANTIFICATION OF FLAWS IN FIBERED COMPOSITE STRUCTURES USING INTERFEROMETRIC FRINGE PATTERNS		5. TYPE OF REPORT & PERIOD COVERED Technical Report
		6. PERFORMING ORG. REPORT NUMBER RL-76-18
7. AUTHOR(s) B.R. Mullinix W.F. Ranson W.F. Swinson T.L. Cost		8. CONTRACT OR GRANT NUMBER(s)
9. PERFORMING ORGANIZATION NAME AND ADDRESS Commander US Army Missile Command ATTN: DRSMI-RL Redstone Arsenal, Alabama 35809		10. PROGRAM ELEMENT, PROJECT, TASK AREA & WORK UNIT NUMBERS 53970M6350
11. CONTROLLING OFFICE NAME AND ADDRESS Commander US Army Missile Command ATTN: DRSMI-RPR Redstone Arsenal, Alabama 35809		12. REPORT DATE 20 April 1976
		13. NUMBER OF PAGES 96
14. MONITORING AGENCY NAME & ADDRESS (if different from Controlling Office)		15. SECURITY CLASS. (of this report) Unclassified
15a. DECLASSIFICATION/DOWNGRADING SCHEDULE		
16. DISTRIBUTION STATEMENT (of this Report) Approved for Public Release; distribution unlimited.		
17. DISTRIBUTION STATEMENT (of the abstract entered in Block 20, if different from Report)		
18. SUPPLEMENTARY NOTES		
19. KEY WORDS (Continue on reverse side if necessary and identify by block number) Nondestructive testing Fibered Composite Structures Interferometric Fringe Patterns Flaw Detection and Quantification		
20. ABSTRACT (Continue on reverse side if necessary and identify by block number) This study concerns the nondestructive detection and quantification of flaws and voids in thin, cylindrical, fiber reinforced, composite, structures. Three different types of flaws were investigated using real-time and double exposure optical holography, and Young's Fringe method of speckle interferometry. The theory for each technique and photographs of the fringe patterns are presented. The fringe density plots were made by both manual and computer methods and the flaw sizes were determined. The displacements and strains were computed. A computer program using conventional finite elements was used to theoretically		

DD FORM 1 JAN 73 1473 EDITION OF 1 NOV 65 IS OBSOLETE

UNCLASSIFIED

SECURITY CLASSIFICATION OF THIS PAGE (When Data Entered)

UNCLASSIFIED

SECURITY CLASSIFICATION OF THIS PAGE(When Data Entered)

BLOCK 20 (Concluded)

compute the displacements near the border of the flaws. A new crack tip element was suggested to improve the results in the region of the flaw border.

The results show that flaws in their fiber reinforced composite structures can be detected and the size determined by either optical holographic or speckle interferometric techniques.

UNCLASSIFIED

SECURITY CLASSIFICATION OF THIS PAGE(When Data Entered)

CONTENTS

	Page
Chapter 1. INTRODUCTION	3
Chapter 2. DEFINITION OF THE PROBLEM AND FINITE ELEMENT ANALYSIS	5
I. PROBLEM DESCRIPTION	5
II. ANALYTICAL METHODS	5
III. DISCUSSION	9
IV. A FINITE ELEMENT FOR BONDS, CRACKS, AND FLAWS.	10
Chapter 3. OPTICAL HOLOGRAPHIC ANALYSIS	15
I. GENERAL.	15
II. APPLICATION OF HOLOGRAPHIC INTERFEROMETRY TO THE SURFACE DEFORMATION MEASUREMENTS OF CYLINDRICAL SHELLS	15
III. SURFACE DEFORMATION MEASUREMENTS OF COMPOSITE CYLINDERS WITH INTERNAL FLAWS	25
IV. FLAW DETECTION IN FIBER GLASS EPOXY THIN WALLED PRESSURE VESSELS	28
V. THE PREPARATION AND USE OF A PHOTOPOLYMER SYSTEM FOR REAL-TIME HOLOGRAPHIC APPLICATIONS	49
Chapter 4. SPECKLE INTERFEROMETRIC ANALYSIS USING YOUNG'S FRINGES	77
I. GENERAL	77
II. FRAUNHOFER DIFFRACTION BY A RECTANGULAR APERTURE	77
III. FRAUNHOFER DIFFRACTION BY TWO NEAR-BY APERTURES	79
IV. INTERFERENCE PATTERNS FROM MULTIPLE APERTURES	82
V. FRINGE DATA ANALYSIS	87
Chapter 5. SUMMARY AND CONCLUSIONS	89
Chapter 6. PLANS FOR FUTURE RESEARCH	91
REFERENCES	93

ACKNOWLEDGMENT

The authors hereby express their sincere gratitude and deep appreciation to Captain C. S. Clarke and Mr. E. A. Murphree for their support on the laboratory work; Mr. S. P. Ryder for his efforts on the fringe analysis computer software; and to Mr. V. G. Irelan for his assistance with the electronics and lasers.

Chapter I. INTRODUCTION

Growth in the use of composite materials for structural applications has generated a concomitant need for the detection and evaluation of flaws inadvertently induced in such structures by manufacturing procedures. Such detection and evaluation procedures can be grouped, quite naturally, with other non-destructive test (NDT) methods used in the inspection and evaluation of homogeneous structures. It appears that recent advances in the fields of optical and acoustical holography may permit applications of these technologies to the NDT field.

In recent years, filament-wrapped composite structures have been utilized in small solid-propellant rocket motors and launch tubes with great success. Use of composite materials in this application has merit due to the high strength-to-weight ratio, the low cost of manufacture, and the ease of assembly of the rocket motor case and grain components. Due to the size and nature of such rocket motors and launch tubes production would occur in an automated fashion at very high rates. Obviously, such high production rates will require an automated system of quality control.

It has been found by experience that flaws are likely to occur in the manufacture of small rocket motor cases in the form of unbonded surfaces where bonds should be. These unbonded regions can occur for several reasons. For example, if the region is contaminated with a foreign substance such as water, grease, etc., the bond will not form. Also, failure to properly apply adhesive to the entire region will prevent the bond from forming. Such conditions are bound to occur occasionally in a mass-production-type operation. The problem is to detect such flaws, assess their significance, and discard the faulty motor case if conditions warrant.

Electro-optical devices associated with optical holography or speckle interferometry can be used for the detection of such flaws. The optical holographic technique is based upon the premise that the character of the surface displacements of a structure with a flaw are different when the structure is loaded than when it is not loaded. Such differences in character can be vividly detected interferometrically by comparing holograms of the loaded and unloaded flawed structure. These comparisons produce fringe patterns with distinct aberrations near a flaw [1].

At the present time, the experimental techniques for detecting flaws have been demonstrated qualitatively. Assessment of flaw sizes and shapes have been demonstrated.

The objective of this work was to determine the magnitude of the surface displacements of three hollow composite cylindrical pressure vessels in the vicinity of three intentionally created flaws (or flaw simulations). The ability of conventional finite-element method of structural analysis to model such structures is evaluated and suggestions are made for improvement.

Chapter 2 of this report defines the three fiber reinforced composite specimen containing known flaws including dimensional details and flaw sizes. Discussion of the application of a conventional finite element program to the composite specimen with flaws is included.

The theory and experimental analysis of optical holography as applied to the three specimens are included in Chapter 3. A technique for real-time optical holography demonstrates how the fringe pattern can be observed under loading conditions which are time dependent. This provides a rapid way to optimize the loading for a specific type of specimen. A method to determine the size and shape of flaws from the optical holographic fringe patterns is presented. The computer software for this technique was developed and a computer plot of "U" curves were utilized to locate and quantify the flaws.

Chapter 4 presents the theory and demonstrates the feasibility of a technique to locate and quantify flaws utilizing the speckle interferometric method with Young's Fringes.

The summary and conclusions of the entire effort are presented in Chapter 5. Chapter 6 includes the plans for future research.

Chapter II. DEFINITION OF THE PROBLEM AND FINITE ELEMENT ANALYSIS

I. PROBLEM DESCRIPTION

To aid in the task of developing an experimental technique for flaw detection in composite structures, three test structures were designed with simulated flaws placed in specific locations and with specific orientations. The simulated flaws were created by placing thin strips of Teflon plastic between the two helical wraps of filaments at the center of the walls of the hollow cylindrical structures. The Teflon strips were intended to inhibit bonding of the resin in the composite between layers at the location of the strips. Thus, the two center layers of the composite structure would be free to move relative to each other. The purpose of the two models designed for study was to permit a comparison to be made of experimental and analytical predictions of the displacements on the surface of the cylinders in the vicinity of the flaws. All models were manufactured with 60 degree helix wraps and details of each type specimen are shown in Figures 1, 2, and 3.

II. ANALYTICAL METHODS

The axisymmetric specimen shown in Figure 1 and the plane strain model in Figure 2 were analyzed using finite-element structural analysis computer programs. The surface deflections along lines parallel to the longitudinal axis for the axisymmetric case and circumferentially for the plane strain specimen were computed at points sufficiently far away from the ends to make the end-cap effects negligible. This approach was selected because it is applicable to complicated geometries or when various materials are used in the same structure, or both.

The particular finite element methods utilized were basically the same computer codes developed at the Rohm and Haas Company, Redstone Research Laboratories, Huntsville, Alabama [2]. The codes have been modified to some extent to include more efficient equation solution methods but are essentially the same as the original Rohm and Haas codes.

The finite element codes used in this study are based upon the theory of linear elasticity and utilize a simplex continuum element to model the structure. No provision is presently made for modeling joints or bonds which may slip or separate. It is assumed that no voids will ever occur between adjacent elements in the finite element model of the structure. Such behavior would occur in a real structure, e.g., when the bond between two adjacent material particles was unable to support a tensile stress. This is one limitation of the present finite element computer program used in this study; it is not capable of adequately describing the behavior of flaws, cracks or joints in a structure where material particles may slide or pull away from adjacent particles.

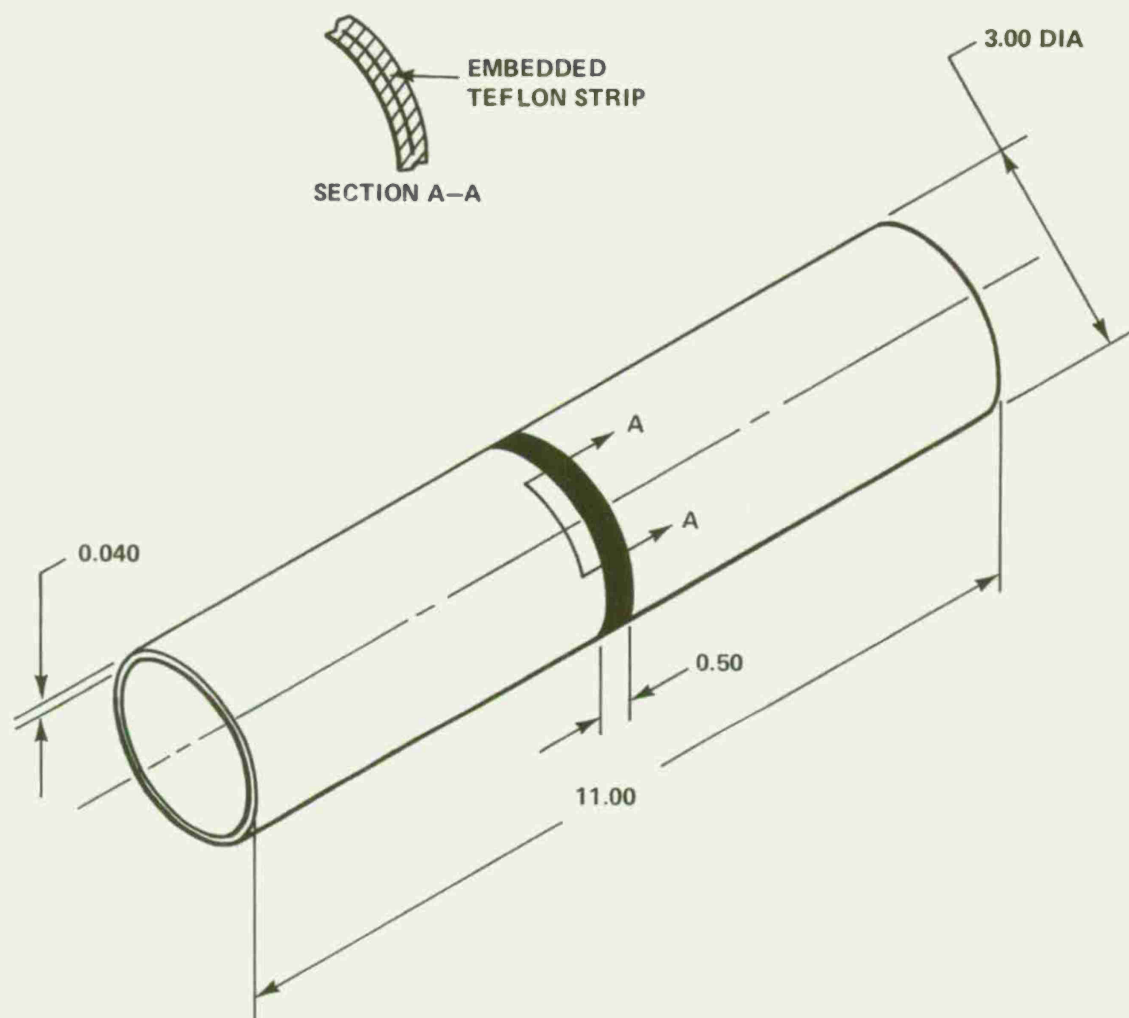


Figure 1. Composite cylinder with simulated circumferential flaw.

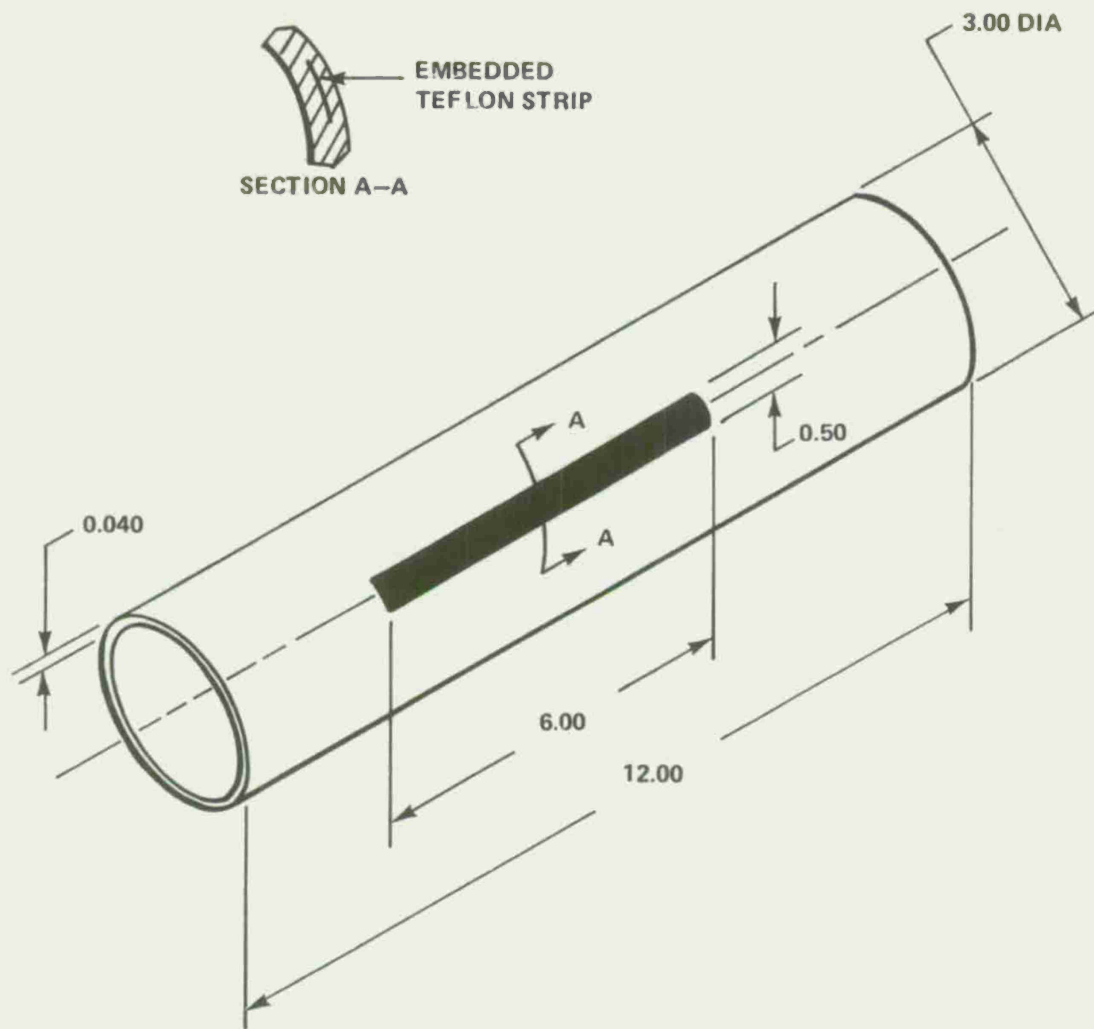


Figure 2. Composite cylinder with simulated longitudinal flaw.

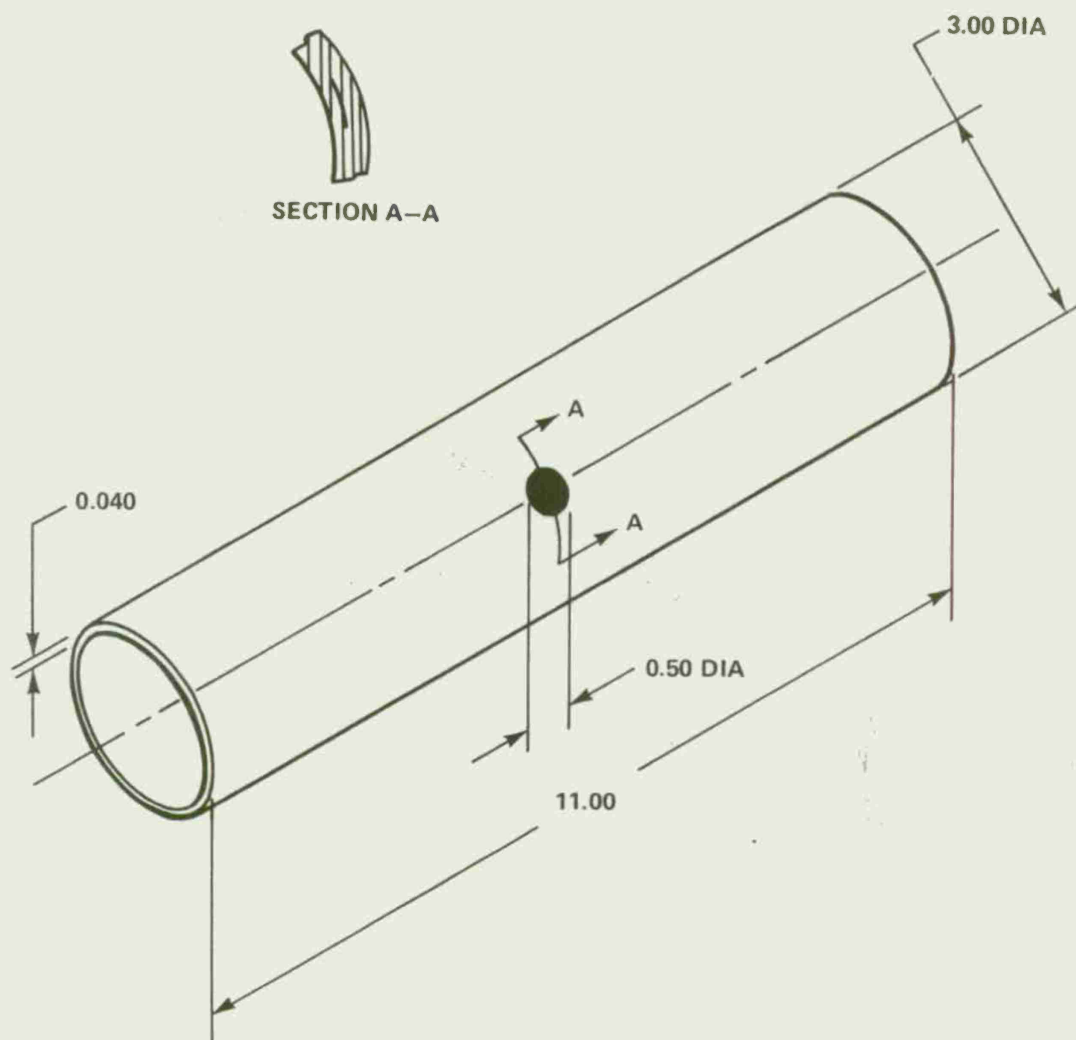


Figure 3. Composite cylinder with simulated spot flaw.

An approach was taken in this study which is typical of current efforts made to model the flaw; the appropriate material properties of the flaw or Teflon inserts were reduced in shear relative to the material properties of the surrounding material. This has the disadvantage that elements with high aspect ratios must be utilized in the finite element model and these tend to produce severe inaccuracies in the computation process. Also, alteration of the material properties may produce a set of ill-conditioned stiffness equations due to the large differences in element stiffnesses. This can also lead to significant numerical computation difficulties.

III. DISCUSSION

By examining the results, it is apparent that the deflection patterns in the vicinity of the simulated flaws are complicated. Rather than a single indentation there are multiple depressions. This behavior has been detected in other structures [3]. These depressions would produce several adjacent concentric fringe patterns near each flaw instead of one concentric pattern.

A judicious choice of finite-element mesh spacing and material property values is required to obtain the results. This was necessary to eliminate numerical inaccuracies and to properly model the slipping effect of the Teflon. As a result of attempts here to model the flaw, it was determined that a more appropriate element stiffness relation in the finite-element computer codes is required to model flaws, cracks, and bonded joints as well. Effort is currently underway to develop a special element to predict displacement around a crack tip. This could greatly improve the ability to analyze continuum structures with such features present. A suggested element stiffness is presented in Section IV of this Chapter.

It is recommended that this element stiffness be incorporated into a finite-element computer program of the type utilized in this study and a study made of its applicability in bonded, cracked, and flawed structures.

Although the study described here was designed to aid in the detection and assessment of flaw sizes in composite structures, the influence of the flaws on rocket motor and launch tube structural integrity during operation can best be made by combined analytical and experimental methods.

An assessment of flaw size and shape influence on structural integrity is being initiated in connection with an automated system for the inspection of rocket motor cases and launch tubes.

IV. A FINITE ELEMENT FOR BONDS, CRACKS AND FLAWS

A. General

It has been recognized in the analysis of composite structures of materials with dissimilar stiffness characteristics that bonded joints and cracks play a decisive roll in the prediction of structural behavior under load. The importance of these characteristics arises from the tendency of the structural components on one side of the joint or crack to slide or pull away from those on the other side. The joints or cracks have a low stiffness in shear or tension but a high stiffness in compression.

In past efforts, the analytical approach adapted to model the joints or cracks involved reducing the appropriate elastic moduli for material in the vicinity of the discontinuity. This approach has the important disadvantage that the complete structure must still be treated as a continuum. Thus, there is no geometrical dimension of the structure which can be correlated with a stability phenomenon; stability of the motion is independent of size.

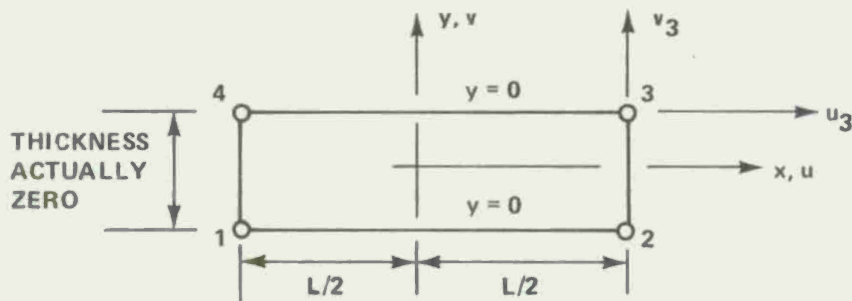
For a more realistic model of this phenomenon, a model of the discontinuity is needed which behaves in a different manner from the structural material on either side of the joint or crack. The discontinuity model should have special properties which permit large deformations in tension and shear stress states and yet be highly stiff in compression.

The finite-element method with simplex elements has been used successfully to model the behavior of continuum structures. However, the continuum element cannot be used to model the discontinuity behavior. The continuum element requires a finite thickness, which although small, leads to an element with a high aspect ratio and hence to inaccuracies in the stress and displacement determinations. A special finite element is needed to model joints and cracks; that is, a line element with special properties: one which can be combined with common continuum finite elements used to model the material surrounding the discontinuities.

B. Joint Element Stiffness

Ideas similar to those presented here have been suggested for use in modeling civil engineering structures such as reinforced concrete and rock formations with joints and cracks.

Consider the four-node element with zero thickness shown in the following diagram.



The element is shown relative to a local coordinate system with axes x and y . Although the element is illustrated with a finite thickness, the thickness is actually zero initially and nodes 1 and 4 and 2 and 3 initially coincide. Assuming that the displacements in the x and y directions vary linearly between nodes on the upper and lower surfaces of the element, the displacement vector on the upper surface can be expressed as

$$\tilde{w}_u = \begin{Bmatrix} u \\ v \end{Bmatrix}_{\text{upper}} = 1/2 \begin{bmatrix} (1 - \frac{2x}{L}) & 0 & (1 + \frac{2x}{L}) & 0 \\ 0 & (1 - \frac{2x}{L}) & 0 & (1 + \frac{2x}{L}) \end{bmatrix} \begin{Bmatrix} u_1 \\ v_1 \\ u_2 \\ v_2 \end{Bmatrix} \quad (1)$$

and that on the lower surface

$$\tilde{w}_l = \begin{Bmatrix} u \\ v \end{Bmatrix}_{\text{lower}} = 1/2 \begin{bmatrix} (1 + \frac{2x}{L}) & 0 & (1 - \frac{2x}{L}) & 0 \\ 0 & (1 + \frac{2x}{L}) & 0 & (1 - \frac{2x}{L}) \end{bmatrix} \begin{Bmatrix} u_3 \\ v_3 \\ u_4 \\ v_4 \end{Bmatrix} \quad (2)$$

Define a relative displacement vector as

$$\tilde{w} = \tilde{w}_u = \tilde{w}_l = \tilde{D} \tilde{u} \quad (3)$$

where \tilde{u} is the matrix of nodal point displacements and where \tilde{D} is composed of the terms in Equations (1) and (2). The joint element stiffness can then be expressed in terms of the relative displacement vector as

$$\begin{bmatrix} k_x & 0 \\ 0 & k_y \end{bmatrix} \begin{Bmatrix} u \\ v \end{Bmatrix} = \begin{Bmatrix} P_x \\ P_y \end{Bmatrix} \quad (4)$$

where k_x and k_y are the joint stiffnesses in the x- and y- directions, respectively, and P_x and P_y are corresponding forces.

Based upon the theorem of stationary potential energy, it can be shown that the stored energy in the element is expressible as

$$E = 1/2 \mathbf{L} \mathbf{u}^T \mathbf{K} \mathbf{u} \quad (5)$$

in which \mathbf{K} is the complete element stiffness matrix expressed as

$$\mathbf{K} \approx \begin{bmatrix} 2k_x & 0 & k_x & 0 & -k_x & 0 & -2k_x & 0 \\ 0 & 2k_y & 0 & k_y & 0 & -k_y & 0 & -2k_y \\ k_x & 0 & 2k_x & 0 & -2k_x & 0 & -k_x & 0 \\ 0 & k_y & 0 & 2k_y & 0 & -2k_y & 0 & -k_y \\ -k_x & 0 & -2k_x & 0 & 2k_x & 0 & k_x & 0 \\ 0 & -k_y & 0 & -2k_y & 0 & 2k_y & 0 & k_y \\ -2k_x & 0 & -k_x & 0 & k_x & 0 & 2k_x & 0 \\ 0 & -2k_y & 0 & -k_y & 0 & k_y & 0 & 2k_y \end{bmatrix} \quad (6)$$

The previous joint element stiffness matrix is constructed for each joint element in a finite element model and then assembled along with continuum elements into the structure stiffness matrix. After solving for the displacements from the stiffness relations, the element stresses can then be calculated. If the joint element stress is positive (tension) normal to the element, then both k_x and k_y should be set equal to zero

for that element and the solution repeated. This cyclic process should be repeated until a consistent set of displacements results.

The element formulation above should permit a more accurate modeling of the joints and cracks in composite structures. This element should eliminate the need for large numbers of high aspect ratio elements in the regions of discontinuities which currently give rise to inaccuracies in the computation process.

An investigation is needed to determine the effect of this element on the computation process. Improvements, if any, in the modeling process should be studied along with appropriate techniques for determining the appropriate stiffness properties k_x and k_y . Provision should also be made to allow a possible coupling between the shear and normal modes of deformation. Finally, the possibility of including a finite shear strength element should be investigated.

Chapter 3. OPTICAL HOLOGRAPHIC ANALYSIS

I. GENERAL

Holographic interferometry has been used as a non-destructive testing method for several years. The various techniques that have been developed essentially use a double-exposure technique to produce interference fringes from a deformed body. If the anomaly in a body is of sufficient size to be critical to structural integrity, irregularities in the fringe pattern can be observed. These irregularities in the fringe pattern are an indication of the variation in the surface deformation due to the subsurface void. Therefore, if the fringes can be interpreted to measure the surface deformation in terms of displacements, some measure of the structural integrity can be made for the body.

Non-destructive testing of thin-wall cylinders seems to be a useful application of holographic interferometry because the void must lie close to the surface. However; for filament wound composite cylinders, the interpretation of the fringe pattern is sometimes complicated by irregularities produced by the filament geometry. In order to determine if holography could be applied to the testing of filament-wound cylinders, three test cylinders with three different geometries were tested. Also, the displacement of the surface was determined to measure the surface variation in the area of the flaw. Several photographs show the different views of each cylinder and illustrate the effect of flaw geometry and filament wrap angle on the fringe pattern.

II. APPLICATION OF HOLOGRAPHIC INTERFEROMETRY TO THE SURFACE DEFORMATION MEASUREMENTS OF CYLINDRICAL SHELLS

A. Basic Theory of Fringe Formation

A common method of forming double-exposure holograms utilizes an off-axis reference beam which was first developed by Leith and Upatnieks [4]. Other methods have been developed; however, only the off-axis reference beam will be considered. When a double exposed hologram is reconstructed, interference fringes are formed on the body due to any displacement of the body between exposures. If the displacement results from deformation as shown in Figure 4 then the fringes are a measure of this deformation. This result is obtained due to the phase change of the light due to deformation of the body between exposures. The basic equation which predicts the interference fringes is the intensity of the virtual image. The intensity of the virtual image in a doubly exposed hologram is given in the following equation [5, 6, 7, 8]

$$I_{\text{VIRTUAL}} = C [1 + \cos \Delta\theta] \quad (7)$$

where C is a constant and $\Delta\theta$ is the phase change of the light due to the deformation of the body.

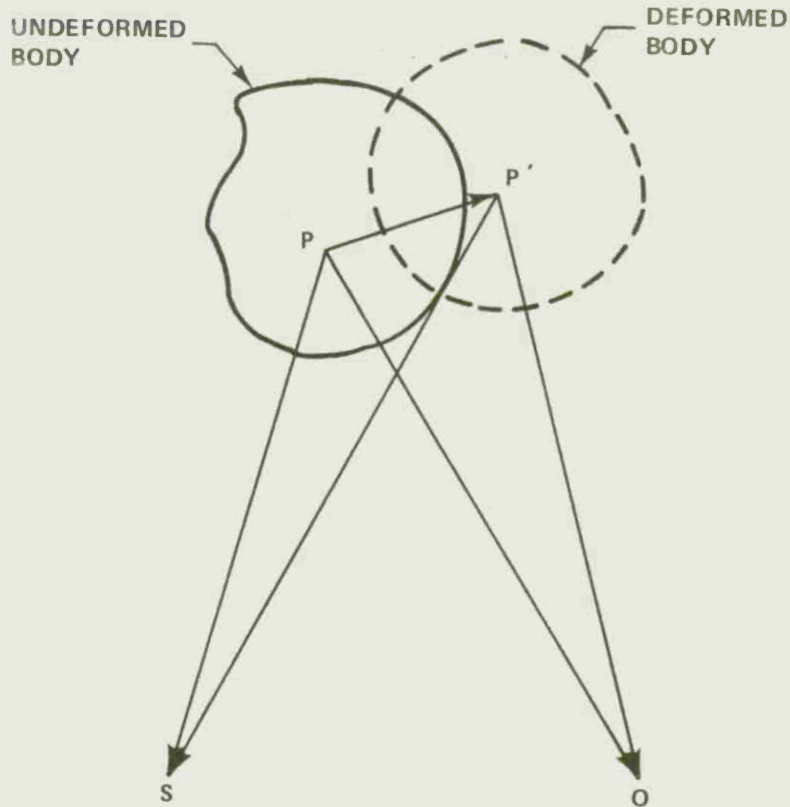


Figure 4. Geometrical relationships for phase change for a deformed body.

A fringe will be defined with $I_{\text{VIRTUAL}} = 0$. From equation (7) the following condition results from the definition of a fringe

$$\Delta\theta = (2n-1)\pi \quad n = 1, 2, 3, \dots \quad (8)$$

The counting number, n , is called the fringe order. Equation (8) is the basic equation which relates the fringe information to the deformation of the body.

The phase change $\Delta\theta$ in equation (8) is determined from the optical path length change of the light between exposures of the hologram. In the reference condition (undeformed state) the optical path length is denoted by L_1 and is the distance (Figure 4).

$$L_1 = |\vec{PS}| + |\vec{PO}| \quad (9)$$

where S is the light source

P is a point on the surface of the body

O is a point in the hologram plane.

The distance, $|\vec{PS}|$, between two points (P,S) is the length of the vector which connects them. Therefore, the distance $|\vec{PS}|$ can be written in terms of the inner product of the point difference. The vector PS connecting the points P and S is defined as the point difference. Equation (9) can now be written in the following form:

$$L_1 = \left[\vec{PS} \cdot \vec{PS} \right]^{1/2} + \left[\vec{PO} \cdot \vec{PO} \right]^{1/2} . \quad (10)$$

The point P on the surface of the body is deformed into the point P'. With the body in the deformed configuration the optical path length of the light, denoted as L_2 is the distance

$$L_2 = |\vec{P'S}| + |\vec{P'O}| . \quad (11)$$

Using the inner product of the point difference, this equation can be written as

$$L_2 = \left[\vec{P'S} \cdot \vec{P'S} \right]^{1/2} + \left[\vec{P'O} \cdot \vec{P'O} \right]^{1/2} . \quad (12)$$

In order to determine the phase change of the light, equations (11) and (12) are used to determine the change in optical path length Δ , where

$$\Delta = L_1 - L_2 . \quad (13)$$

Substitution of equations (11) and (12) into equation (13) yields for the optical path length change

$$\Delta = \left[\vec{PS} \cdot \vec{PS} \right]^{1/2} + \left[\vec{PO} \cdot \vec{PO} \right]^{1/2} - \left[\vec{P'S} \cdot \vec{P'S} \right]^{1/2} - \left[\vec{P'O} \cdot \vec{P'O} \right]^{1/2} . \quad (14)$$

The phase change $\Delta\theta$ is related to Δ by $2\pi/\lambda$, therefore the phase change is written as

$$\Delta\theta = \frac{2\pi}{\lambda} \left\{ \left[\vec{PS} \cdot \vec{PS} \right]^{1/2} + \left[\vec{PO} \cdot \vec{PO} \right]^{1/2} - \left[\vec{P'S} \cdot \vec{P'S} \right]^{1/2} - \left[\vec{P'O} \cdot \vec{P'O} \right]^{1/2} \right\} . \quad (15)$$

This equation, while completely general, is not in a form convenient for numerical use. Let the point difference of the body before and after deformation be PP' , then

$$\vec{PS} = \vec{P'S} + \vec{PP'}$$

$$\vec{PO} = \vec{P'O} + \vec{PP'} \quad . \quad (16)$$

Therefore, equation (15) can be written in the following form using equation (16), which yields

$$\begin{aligned} \Delta A = \frac{2\pi}{\lambda} & \left\{ \left[\vec{PS} + \vec{PS} \right]^{1/2} + \left[\vec{PO} \cdot \vec{PO} \right]^{1/2} \right. \\ & - \left[(\vec{PS} \cdot \vec{PS}) - 2(\vec{PS} \cdot \vec{PP'}) + (\vec{PP'} \cdot \vec{PP'}) \right]^{1/2} \\ & \left. - \left[(\vec{PO} \cdot \vec{PO}) - 2(\vec{PO} \cdot \vec{PP'}) + (\vec{PP'} \cdot \vec{PP'}) \right]^{1/2} \right\} . \quad (17) \end{aligned}$$

In holographic interferometry, the displacements of points between exposures are small; therefore, it will be assumed here that $|\vec{PP'}|^2 \ll |\vec{PP'}|$. Using this information the last two terms in equation (17) can be written in the following form for small deformations between exposures:

$$(\vec{PS} \cdot \vec{PS}) - 2(\vec{PS} \cdot \vec{PP'}) \stackrel{1/2}{\approx} \vec{PS} \cdot \vec{PS} - \frac{\vec{PS} \cdot \vec{PP'}}{|\vec{PO} \cdot \vec{PO}|^{1/2}} + \quad (18)$$

and

$$\left[(\vec{PO} \cdot \vec{PO}) - 2(\vec{PO} \cdot \vec{PP'}) \right]^{1/2} \approx \vec{PO} \cdot \vec{PO} - \frac{\vec{PO} \cdot \vec{PP'}}{[\vec{PO} \cdot \vec{PO}]^{1/2}} + \quad (19)$$

Using the results in (18) and (19), the phase change can now be written as

$$\Delta A = \frac{2\pi}{\lambda} \left[\frac{\vec{PS}}{[\vec{PS} \cdot \vec{PS}]^{1/2}} + \frac{\vec{PO}}{[\vec{PO} \cdot \vec{PO}]^{1/2}} \right] \cdot \vec{PP'} \quad . \quad (20)$$

The terms in brackets in equation (20) are unit vectors in the direction PS and PO; therefore, the following change in notation is employed:

$$\begin{aligned}\vec{p_s} &= \frac{\vec{PS}}{[\vec{PS} \cdot \vec{PS}]^{1/2}} \\ \vec{p_o} &= \frac{\vec{PO}}{[\vec{PO} \cdot \vec{PO}]^{1/2}}\end{aligned}\quad (21)$$

Equation (8) can now be written in the following form:

$$[\vec{p_s} + \vec{p_o}] \cdot \vec{PP'} = \frac{(2n-1)\lambda}{2} \quad (22)$$

These results are still in a general form and special cases will be considered in regard to the deformation of cylindrical shells.

B. Deformation of Cylindrical Shells

The displacement vector $\vec{PP'}$ of a point on the surface of the shell is resolved into three components, a radial component U_r , a circumferential component U_ϕ , and longitudinal component U_z . The experimental geometry and coordinate system of the cylinder are shown in Figure 5. The point P on the surface can be represented in either cartesian or cylindrical coordinates. In the cartesian system let $\vec{PP'}$ have the following representation:

$$\vec{PP'} = U_{X_1} \vec{e}_1 + U_{X_2} \vec{e}_2 + U_{X_3} \vec{e}_3 \quad (23)$$

and the following representation in the cylindrical system

$$\vec{PP'} = U_r \vec{e}_r + U_\phi \vec{e}_\phi + U_z \vec{e}_z \quad (24)$$

The relation between the unit base vectors are as follows:

$$\begin{aligned}\vec{e}_z &= \vec{e}_2 \\ \vec{e}_r &= \vec{e}_1 \sin \phi + \vec{e}_3 \cos \phi \\ \vec{e}_\phi &= \vec{e}_1 \cos \phi - \vec{e}_3 \sin \phi\end{aligned}\quad (25)$$

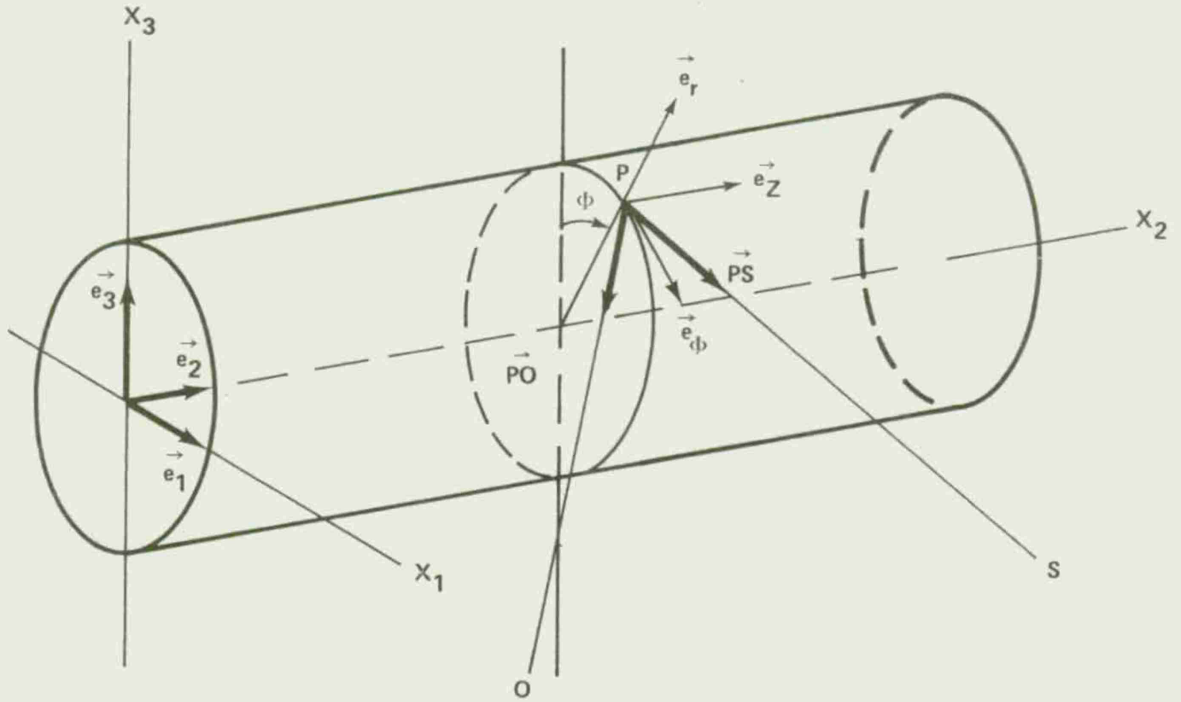


Figure 5. Geometry used to measure the surface deformation of cylindrical shells.

Let the vectors \vec{ps} and \vec{po} have the representations shown in Figure 6.

Then,

$$\vec{ps} = \ell_1 \vec{e}_1 + \ell_2 \vec{e}_2 + \ell_3 \vec{e}_3$$

$$\vec{po} = m_1 \vec{e}_1 + m_2 \vec{e}_2 + m_3 \vec{e}_3 \quad (26)$$

where ℓ_1, ℓ_2, ℓ_3 and m_1, m_2, m_3 are the set of direction cosines of the vectors \vec{ps} and \vec{po} , respectively.

Using the notation for the cylindrical shell, equation (22) can be written in the following form:

$$\begin{aligned} &(\ell_1 + m_1) (U_r \sin \phi + U_\phi \cos \phi) + (\ell_2 + m_2) U_z \\ &+ (\ell_3 + m_3) (U_r \cos \phi - U_\phi \sin \phi) = \frac{(2n-1)}{2} \end{aligned} \quad (27)$$

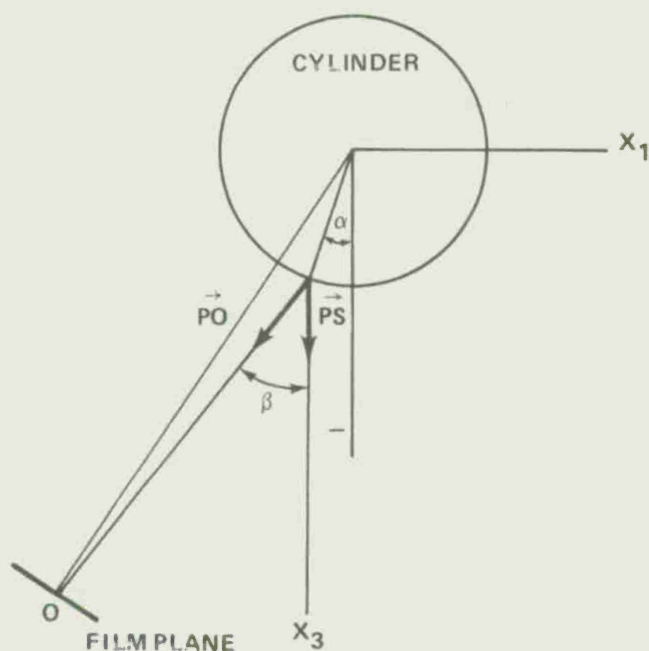


Figure 6. Geometrical relationships for the directions \vec{PS} and \vec{PO} .

Equation (27) illustrates that the fringe information in a single hologram contains information for all three displacement components that cannot be determined uniquely from a single hologram. In order to determine the components uniquely three holograms must be recorded simultaneously. Each hologram will have an equation relating fringe order to displacements as given in equation (27). In each case, the direction cosines to the unit vectors \vec{ps} and \vec{po} will be different for each hologram. This general procedure will require considerable data reduction in order to determine U_r , U_ϕ , and U_z . However, some simplifications can be made in many problems; and with careful selection of the experimental geometry the amount of data reduction can be reduced. Two examples will be considered to illustrate the application of equation (27) to the measurement of surface deformation of cylindrical shells.

(1) Example 1: Symmetrical Deformation of Cylindrical Shells. The cylinder will be assumed to be deformed symmetrically about the longitudinal axis. For this case, the component $U_\phi = 0$ and U_r , U_z are assumed to be nonzero. Direction cosines for this geometry are shown schematically in Figure 6. The direction cosines for the PS direction are

$$l_1 = 0$$

$$l_2 = 0$$

$$l_3 = 1 \quad .$$

Values for the PO direction are

$$m_1 = -\sin \beta$$

$$m_2 = 0$$

$$m_3 = \cos \beta \quad .$$

This particular geometry assumes that the surface of the cylinder is illuminated with collimated light parallel to the X_3 direction. The direction of \vec{ps} is the same at every point on the surface of the cylinder. Also, the direction cosine m_2 is assumed to be zero. This direction cosine is the angle between the observation direction and the X_2 axis. If the hologram is located at a long distance from the cylinder and the cylinder axis X_2 is parallel to the hologram plate, then m_2 will be negligible compared to the other values. Therefore, it can be assumed to be zero. The only non-zero displacement component to be measured is U_r as shown schematically in Figure 7.

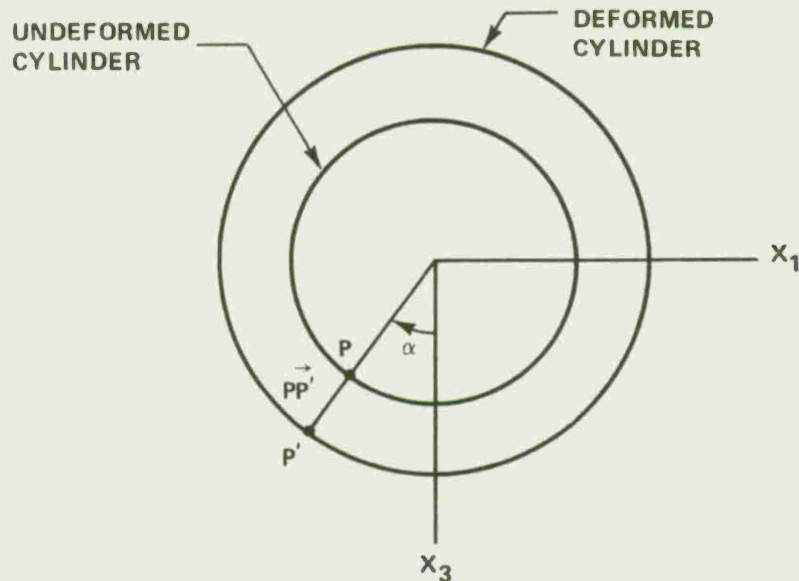


Figure 7. Symmetrical deformation displacement component $\vec{PP'}$ for a circular cylinder.

For this example, equation (27) reduces to .

$$-\sin \beta U_r + (1 + \cos \beta) U_r \cos \Phi = \frac{(2n-1)\lambda}{2} \quad (28)$$

This equation can be solved for U_r , which yields

$$U_r = \frac{(2n-1)\lambda}{2[(1 + \cos \beta) \cos \Phi - \sin \beta]} \quad (29)$$

Example 1 illustrates that for the case of symmetrical deformation, and with proper selection of the experimental geometry, U_r can be determined from a single hologram.

(2) Example 2: Radial Deformation Measurements of Cylindrical Shells with Non-Symmetrical Deformation. The second example will consider the general case of the deformation of cylindrical shells. Only in this example the radial deformation of cylindrical is to be measured with non-zero values of U_θ and U_z . Figure 8 is a schematic diagram of the experimental configuration to measure the radial deformation.

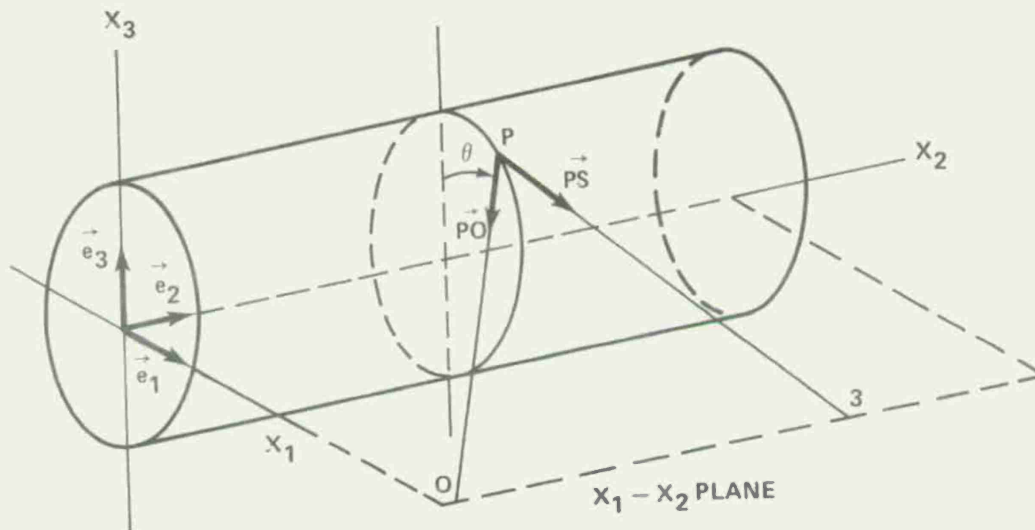


Figure 8. Geometry used to measure the radial displacement component for cylindrical shells with non-symmetrical deformation.

For this example the direction cosines are chosen to be (Figure 9)

$$\ell_1 = \cos \theta$$

$$\ell_2 = \sin \theta$$

$$\ell_3 = 0$$

and

$$m_1 = \cos \theta$$

$$m_2 = \sin \theta$$

$$m_3 = 0$$

In this example all light rays are assumed to be collimated with illuminating and observation directions in symmetric directions with respect to the X axis.

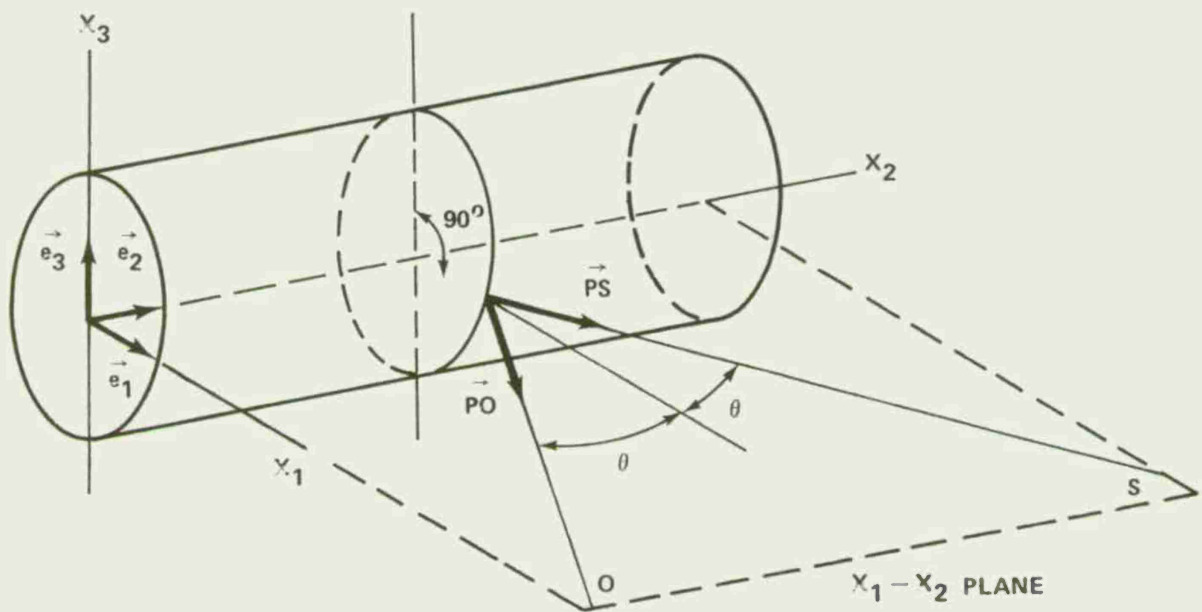


Figure 9. Geometrical relationships for the \vec{PS} and \vec{PO} directions in the $X_1 - X_2$ plane.

Equation (27) for this example reduces to

$$2 \cos \theta (U_r \sin \phi + U_\phi \cos \phi) = \frac{(2n-1)\lambda}{2} \quad (30)$$

If observations are made in the X_1 X_2 plane, then $\sin \phi = 1$, $\cos \phi = 0$, and equation (35) reduces to

$$U_r = \frac{(2n-1)\lambda}{4 \cos \theta} \quad (31)$$

As in Example 1, if proper choice is made with the experimental geometry then the general form of equation (27) can be reduced to a form that is amenable to use in numerical computations. These two examples are used to illustrate how the basic equation in holographic interferometry can be used to measure uniquely the radial component of surface displacement of cylindrical shells.

A numerical example was chosen in order to illustrate the application of the equations in Example 2. This example assumes the cylinder to be aluminum with the following geometrical and material properties:

- a) Thickness = 0.020 inches
- b) Modulus of elasticity = 10.2×10^6 psi
- c) Mean radius = 3 inches
- d) Poisson's ratio = 0.332
- e) Internal pressure = 10 psig
- f) λ = 24.9×10^{-6}
- g) θ = 10°

With these properties, the fringe order can be determined as a function of the angular coordinate. Figure 10 is a graph of the fringe order versus angular coordinate. The corresponding fringe pattern is shown in Chapter 3, Section IV.

III. SURFACE DEFORMATION MEASUREMENTS OF COMPOSITE CYLINDERS WITH INTERNAL FLAWS

In order to measure the surface deformation of composite cylinders with internal flaws, the three test models shown in Figures 1, 2, and 3 were made with simulated flaws in specified locations. Each cylinder was pressurized and the radial surface deformation was measured using an experimental configuration as shown in Figure 11. This holographic configuration will produce an interference fringe pattern which is a measure of the radial displacement of the outer surface. The following data were used for each test:

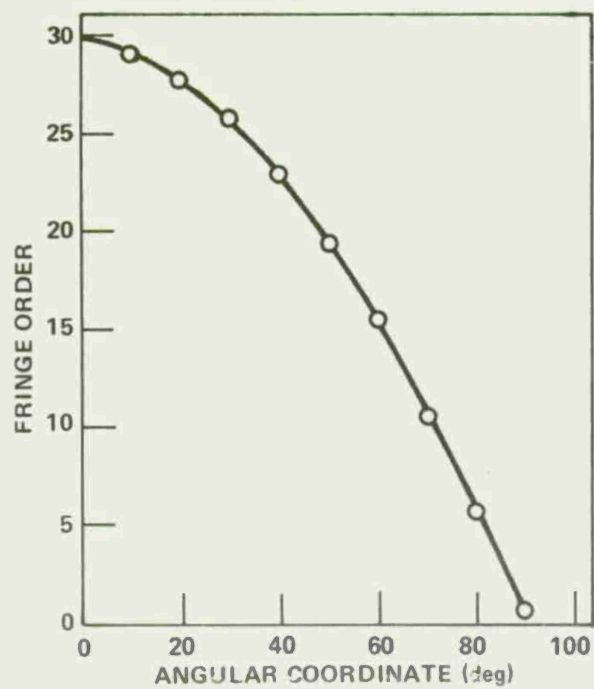


Figure 10. Fringe order for symmetrical deformation of an aluminum cylinder.

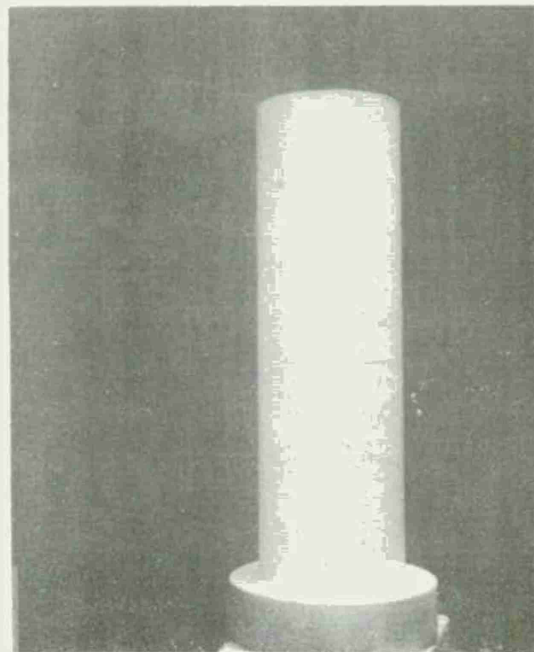


Figure 11. Typical composite cylinder.

a) $\theta = 8.5^\circ$.

b) $\lambda = 632.8 \times 10^{-9}$ meters .

The measurements are made independent of material properties. Only the geometry and wavelength of light is needed in order to measure the surface deformation.

The fringe pattern produced by a spot flaw is shown in Figure 12. This type of flaw is easily recognized from the photograph. The circular fringes in the center are approximately the same diameter as the flaw.

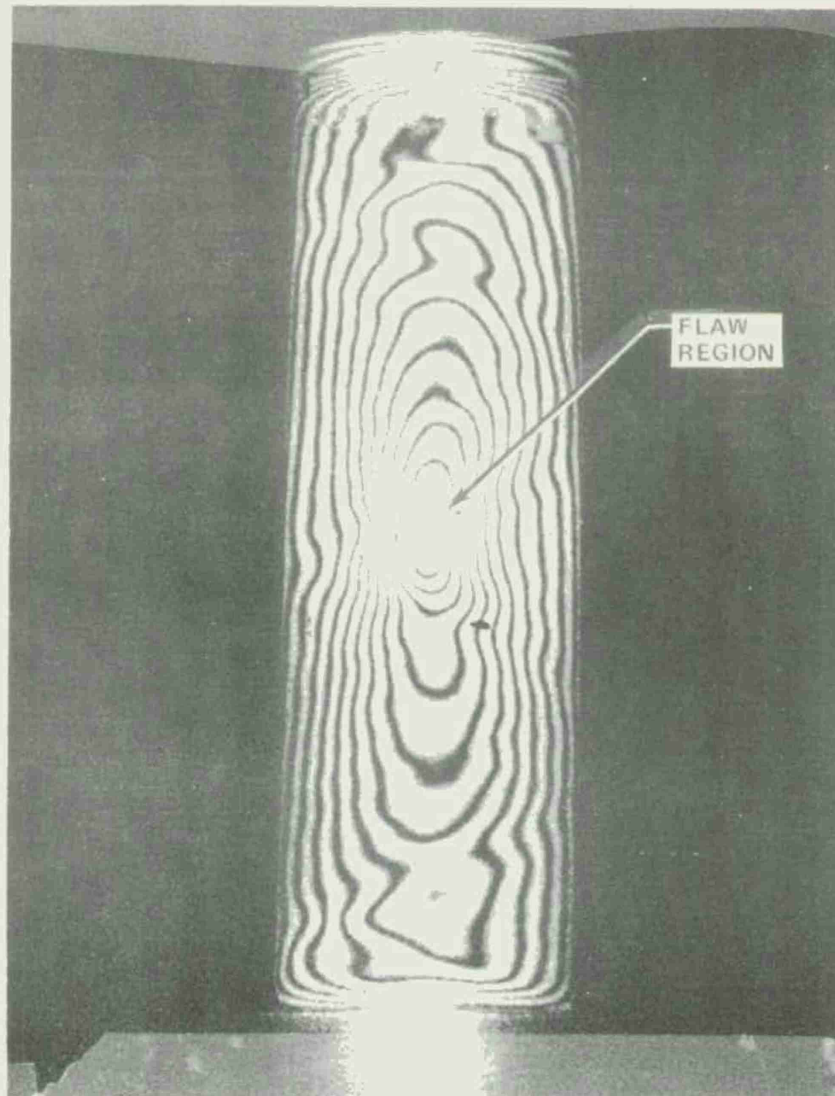


Figure 12. Fringe pattern for the cylinder with a spot flaw.

In the regions away from the flaw the fringes are parallel to the longitudinal axis. This type of fringe pattern is characteristic of symmetrical deformation. Therefore, if the cylinder were free of internal voids, the fringes would be a series of parallel lines away from any end effects. For this case the radial deformation was calculated along a line in the center of the cylinder. The displacements are shown in graphical form in Figure 13. As can be seen from this figure the radial displacement changes by a large amount in the region near the flaw.

Figure 14 shows the fringe pattern produced by the circumferential flaw. As can be seen from the photograph this fringe pattern is more complex than the spot flaw. The internal pressure for this cylinder was 20 psig. At the higher pressures the deformation from the wrap angle geometry becomes significant. The areas of the cylinder where the layers overlap act as a stiffener effect to the shell. Therefore, the fringe pattern is not one that is characteristic of a symmetrical deformation of an isotropic cylinder. However, the presence of the circumferential flaw can be seen in the photograph. Figure 15 shows the radial deformation of the cylinder with an internal circumferential flaw. This type of flaw is not as easily seen in the photograph. However, it is believed that the spot flaw is a more realistic type of flaw that will occur in a production situation.

Figure 16 shows a composite cylinder with a longitudinal flaw. The fringe pattern for this flaw geometry is significantly changed by the presence of the flaw. This type of flaw geometry produces a complex fringe pattern similar to the circumferential flaw. However, this flaw is not expected to be representative of a production-type flaw. Radial deformation for this flaw geometry is not as easy to determine as in the previous examples. As can be seen from the photograph, the radial deformation is essentially constant along the longitudinal axis of the flaw. Therefore, the radial deformation was plotted as a function of the angular coordinate relative to the cylinder centerline. Figure 17 shows the fringe order data as it appears on the photograph. The distance measured on the photograph relative to the cylinder centerline is then used to determine the angular coordinate. After the angular coordinate is known then the radial deformation can be calculated. Figure 18 shows the radial deformation for the longitudinal flaw geometry.

IV. FLAW DETECTION IN FIBER GLASS EPOXY THIN WALLED PRESSURE VESSELS

A. General

Weapon sophistication points out the need for a higher strength-to-weight ratio and especially for small structures that are used once and then discarded. This higher strength-to-weight ratio has necessitated structures made from composite materials such as glass and epoxy. However, along with these more efficient structures, undetermined stress distributions exist. The stress distribution solutions for

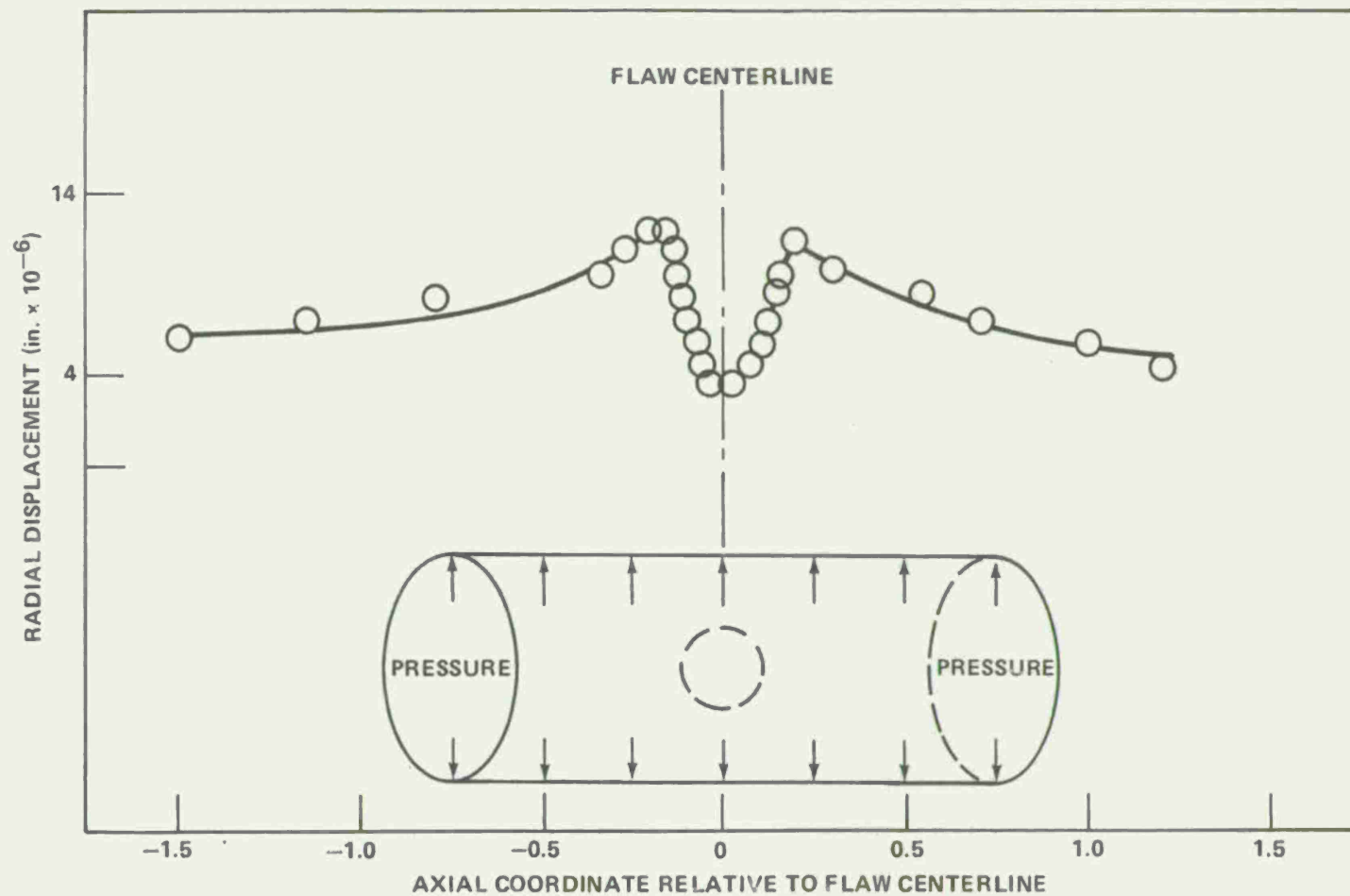


Figure 13. Surface deformation of composite cylinder with a spot flaw, internal pressure 10 psig.

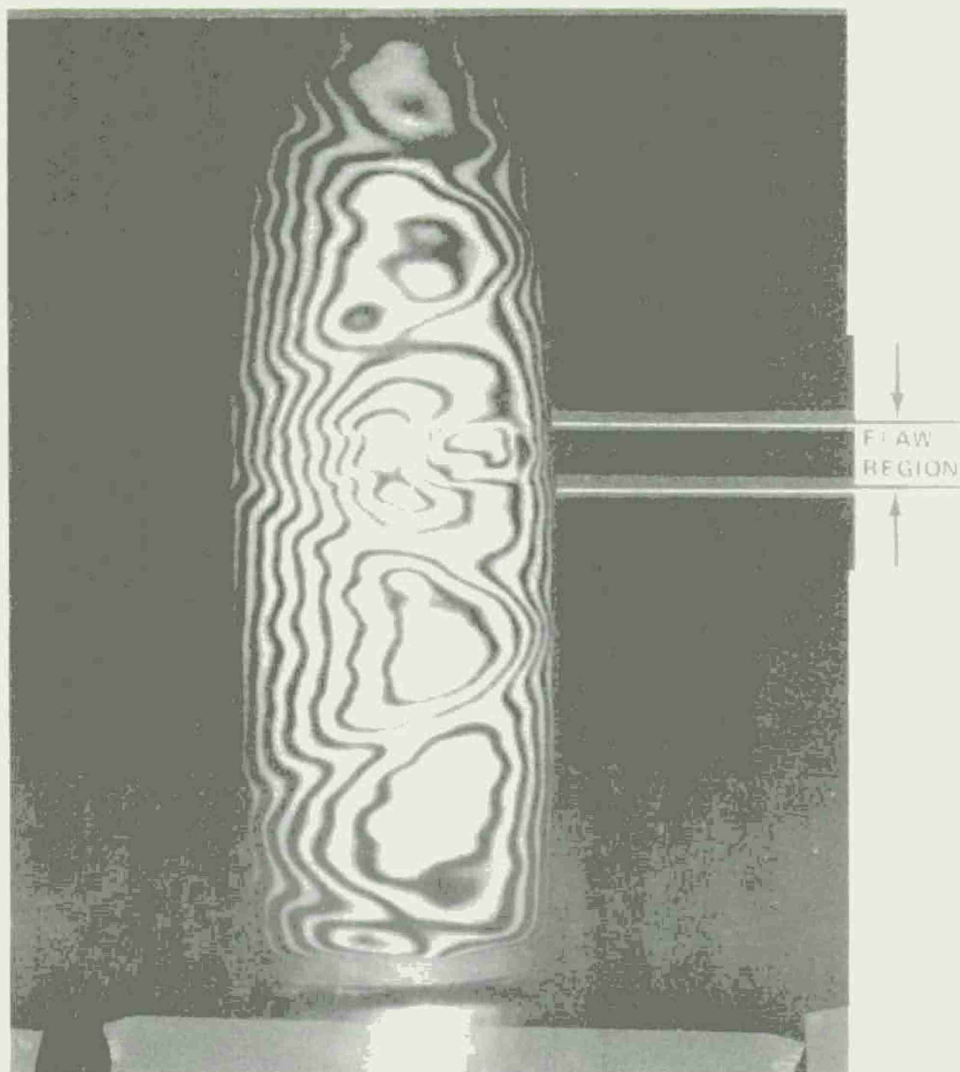


Figure 14. Fringe pattern for the cylinder with a circumferential flaw.

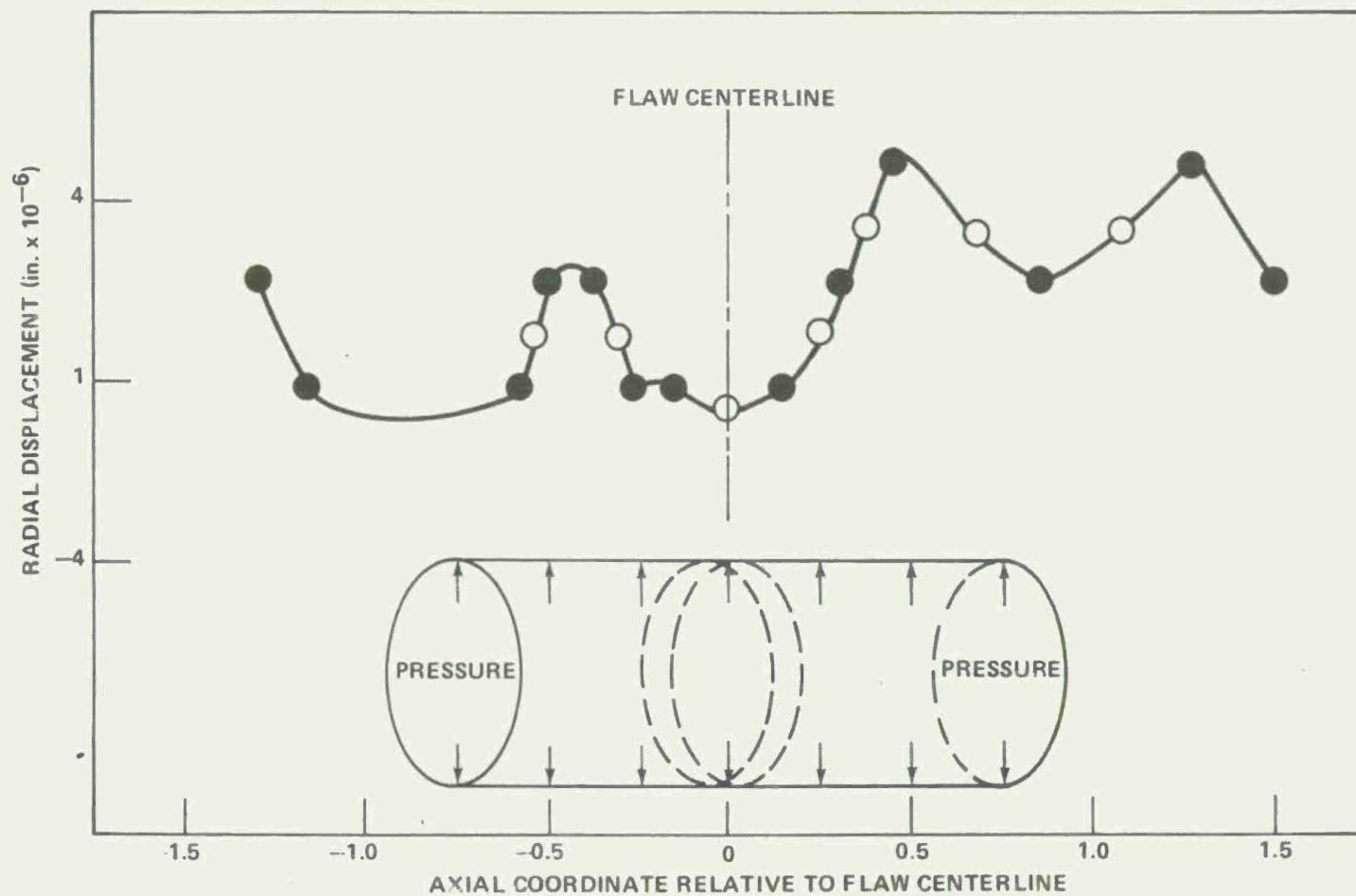


Figure 15. Surface deformation of composite cylinder with a circumferential flaw, internal pressure 20 psig.

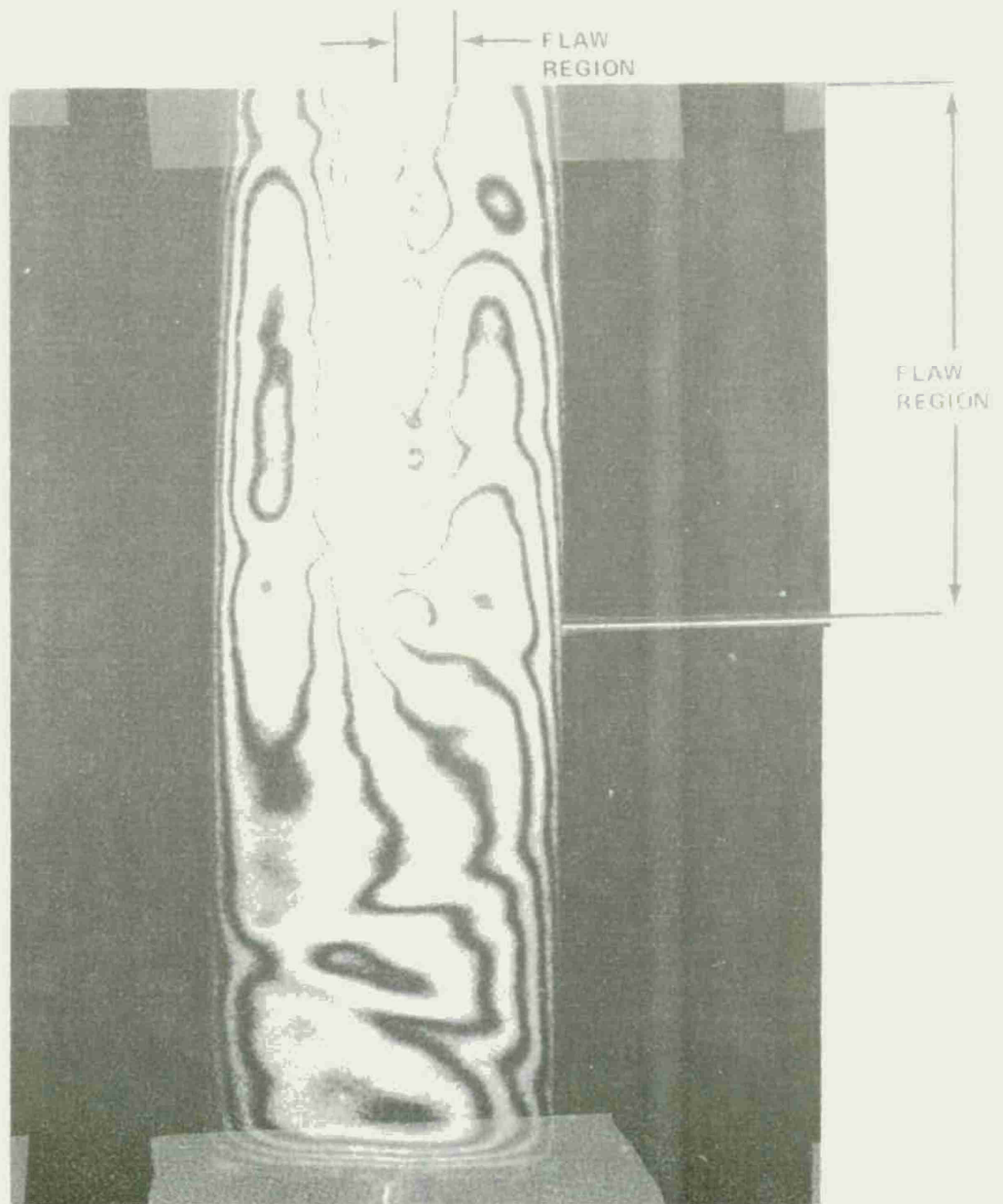


Figure 16. Fringe pattern for the cylinder with a longitudinal flaw.

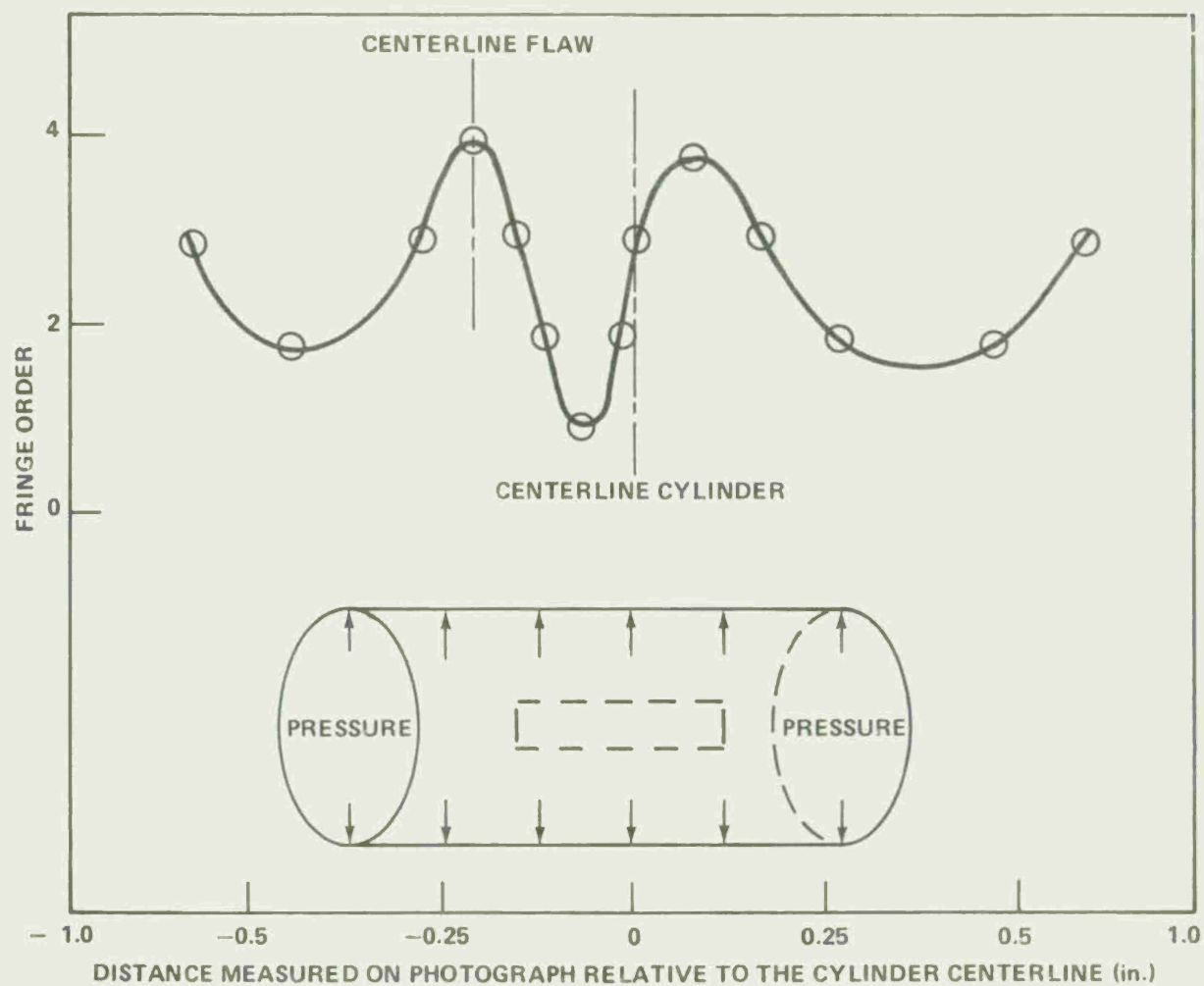


Figure 17. Fringe orders of a composite cylinder with a longitudinal flaw, internal pressure 10 psig.

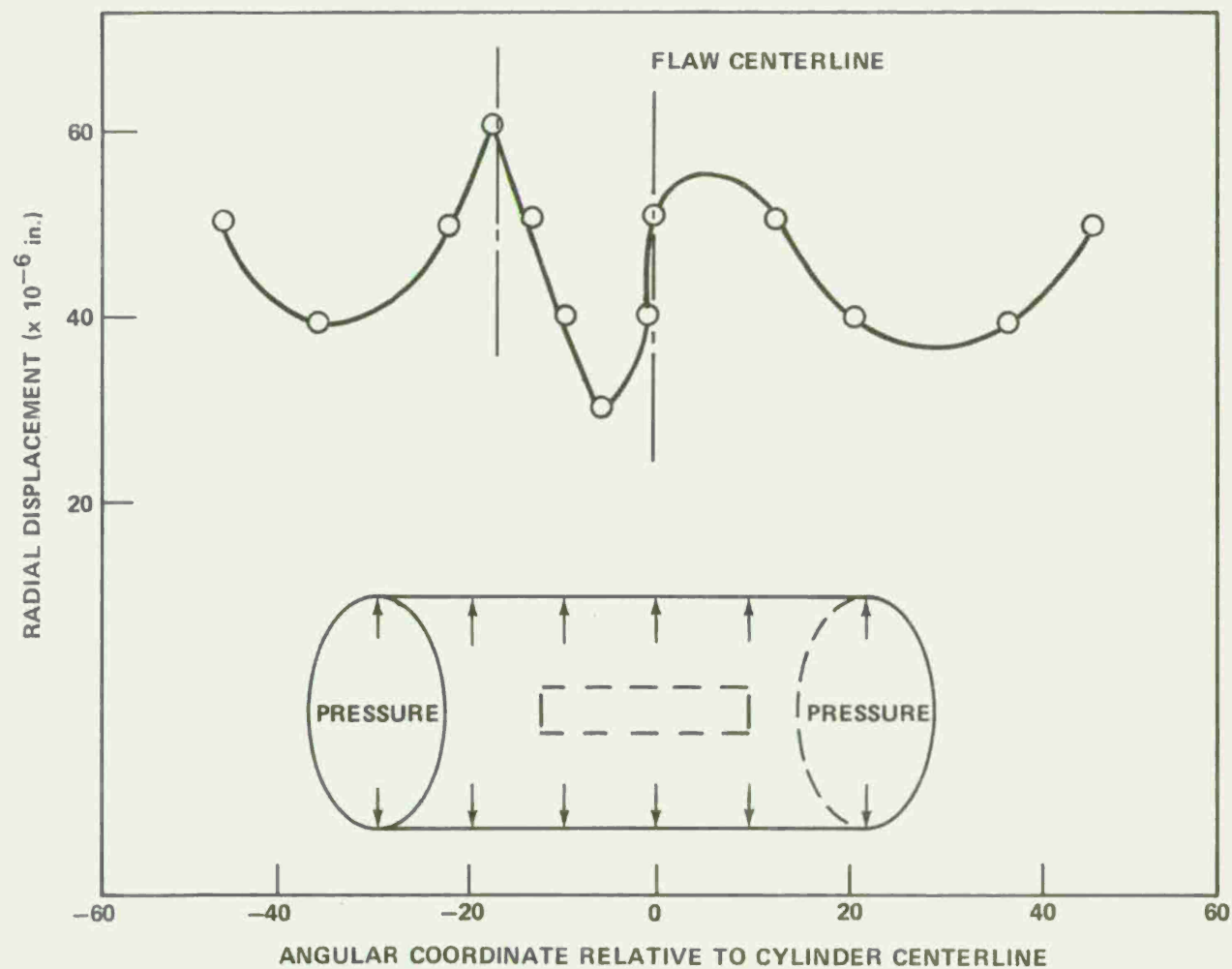


Figure 18. Surface deformation of composite cylinder with a longitudinal flaw, internal pressure 10 psig.

homogeneous structures are not valid. Until adequate analytical techniques can be developed, more testing is needed to evaluate structural integrity of composite-material structures.

For thin-walled pressure vessels made from composite materials and utilized as hand-held rocket tubes, safety considerations demand reliability. Flaws such as broken fibers or delamination between the glass and epoxy affect the structural integrity of the structure and a need exists to detect these flaws that can occur in manufacturing.

The optical technique of holography is recommended. The technique is nondestructive, and can be arranged for reasonably fast evaluation on a real-time basis. Further, the technique is sensitive enough to detect flaws in thin-walled structures without requiring pressure high enough to degrade the structure.

B. Holographic Technique

In reference to this problem, it was first necessary to show that flaws could be detected using double-exposure holography.

A thin-walled composite material cylinder was capped and pressurized. A flaw was "manufactured" in the vessel during winding by inserting a thin teflon disk (0.5 inch in diameter) between the glass layers. Figure 19 illustrates a doubly exposed hologram of the test vessel. The known flaw was on the opposite side shown; thus, represents a normal vessel without flaws. The hologram is a doubly exposed hologram with one exposure taken at no load and one exposure with 30-psi load. Figure 20 illustrates the presence of a flaw (under A and about the center of the vessel).

The evidence of the fiber wrap angles between layers is noted. When this typical fringe pattern is compared with that of a typical homogeneous vessel (Figure 21) the difference is evident. While this difference is marked by careful restrictions, some comparisons can be made.

Observing Figure 20, where the flaw is evident approximately half way between the end caps, the size of the flaw (disbond) is estimated at 0.45-inch across. This compares favorably with the 0.5-inch flaw manufactured into the vessel (the diameter of vessel is 3.25 inches). The size of the flaw was estimated from the photograph as the area contained by fringes in the vicinity of the flaw. This technique seemed consistent on other photographs of similar flaws and seems sufficient to estimate the size of flaw.

While the technique of double-exposure holography can be used to detect flaws, complicating factors exist and must be resolved.

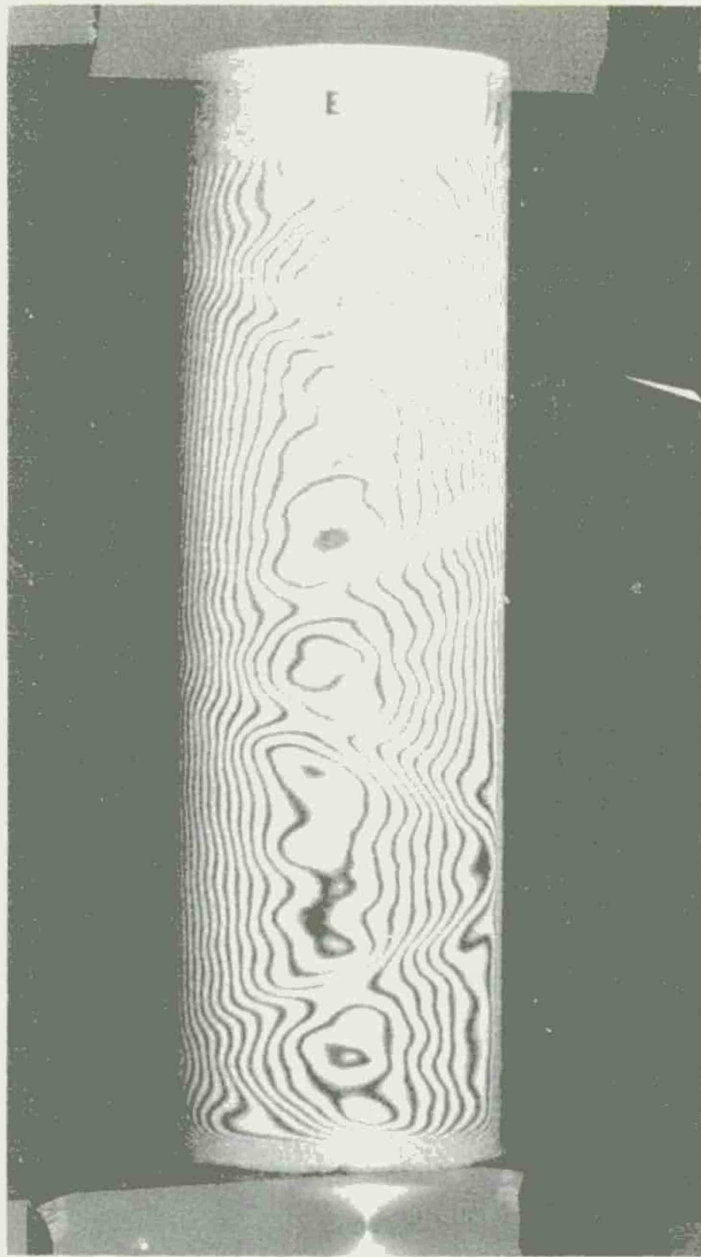


Figure 19. Doubly exposed hologram
of the test vessel.

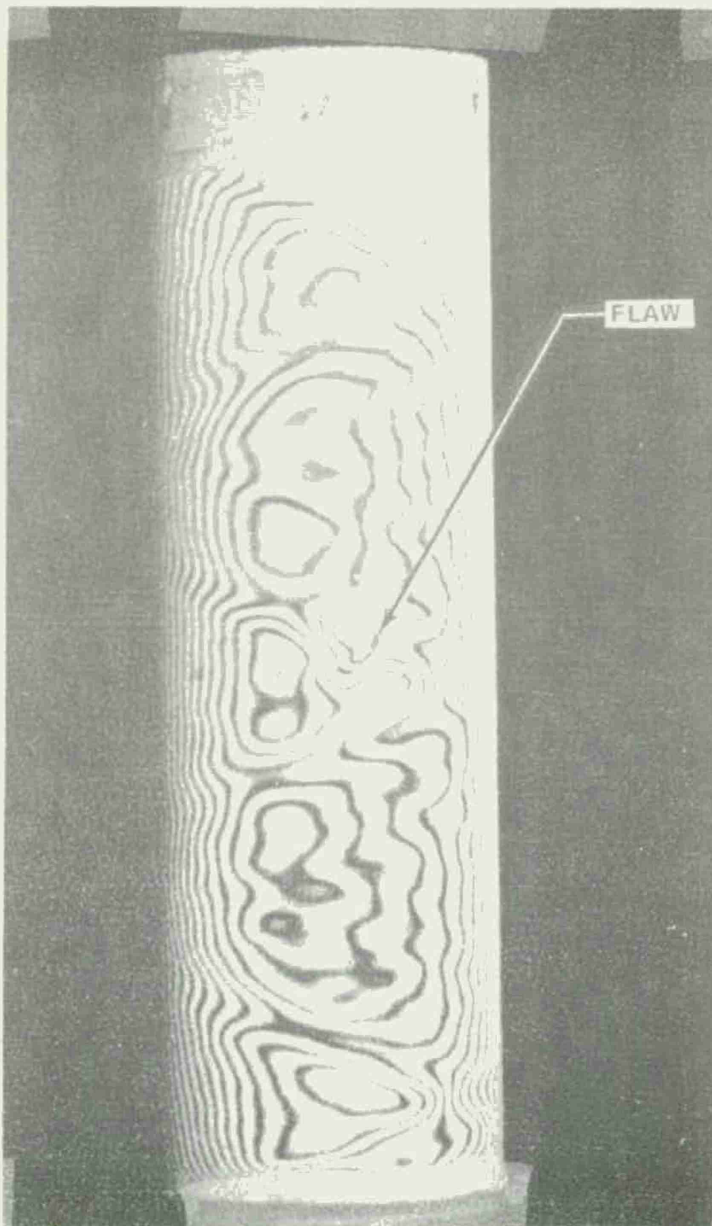


Figure 20. Flaw location under Section A
at the center of the vessel.

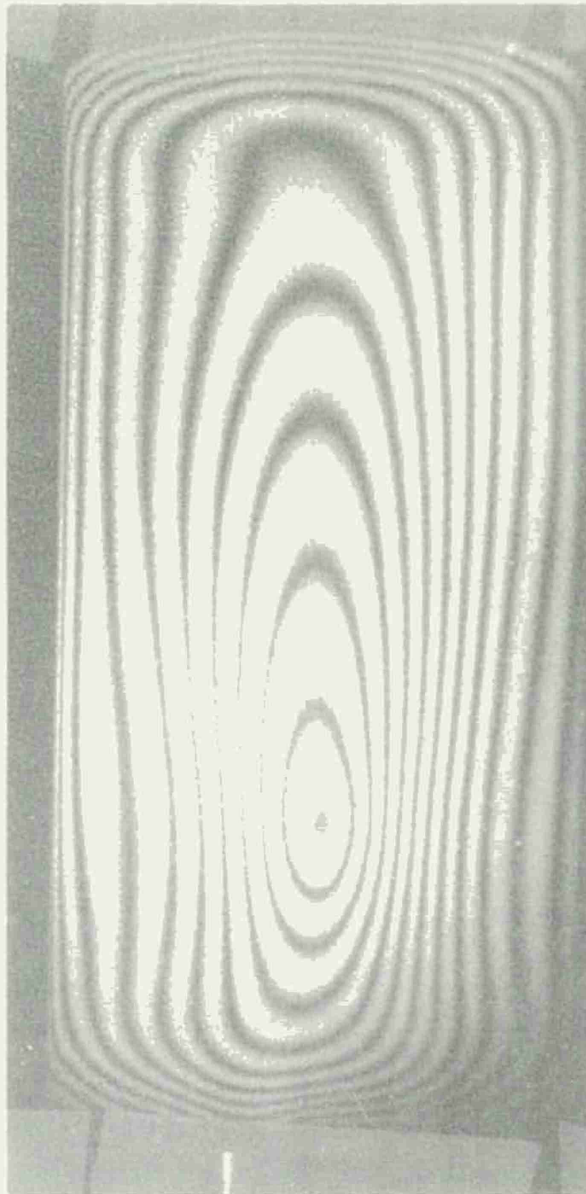


Figure 21. Typical hologram of homogeneous aluminum pressure vessel without flaws.

One complication is the need to develop the holographic film, which requires time and thus is not ideal as an inspection technique for mass production of these pressure vessels. This complication can be eased by using a photopolymer instead of film which allows an investigator to observe the fringe pattern as it occurs (real time). One video tape was made of the event to demonstrate capability and the possibility of later evaluation. The preparation and use of the photopolymer material is described later in Section V of this chapter with photographs of the resulting fringe patterns.

Another complication is the need to automatically read the fringe patterns and detect a flaw. After considering several approaches, one reasonable way is to scan the fringe pattern with a photometer at small increments along the axis of the cylinder and note "shifts" from a normal "s" curve. Such a plot is illustrated in Figure 22. Line zero goes through the center of a flaw and is located under "A" of the figure. The fringe number is plotted as a light meter would detect a fringe scanning across the photograph. In a normal plot (with a flaw) such as along line 6 the fringe spacing is close at the beginning, followed by large fringe spacing and finally close fringe spacing as noted on the plot. Evidence of a flaw can be detected on line 3 where the fringe plot deviates from the "s" curve and a "hump" on the curve is noted. This type of effect is noted on lines -3, -2, -1, 0, 1, 2, 3, 4 and established the size of the flaw which scales out to be 0.59 inch which compares favorably since it is expected that the disbond is slightly larger than the known 0.5 inch diameter teflon in the vessel. Thus, by taking a photometer scan and digitizing, the fringe spacings (curve tangents) can be stored and note made of the deviation from the normal "s" curve indicating a flaw. In this example the area enclosed by A_1 represents the flaw. Attention is called to a second "trouble spot"¹ which is just below A_1 and labeled A_2 . This appears to be caused by layers of glass interacting at a bias angle and suggests a possible "flaw" that can be in vessels due to the lay of the windings. Figure 23 also shows where the type of "flaw" is not near another flaw.

To enhance the flaw detection and reduce the time required to test each cylinder, computer software was developed to scan, digitize, and analyze the holographic fringe patterns in regions where flaws were located using a Fringe Pattern Analyzer. The approximate size of the flaws was determined. "U" curves were utilized in the computer plots in an effort to capitalize on the symmetric properties of the fringe patterns and make flaws more easily detected.

The Fringe Pattern Analyzer is a computerized system for scanning, digitalizing, processing, and displaying line information recorded on film ranging in size from 16mm movie film to 4 x 5-inch cut film. The scanning unit is a stepping spot scanner in which a spot is stepped

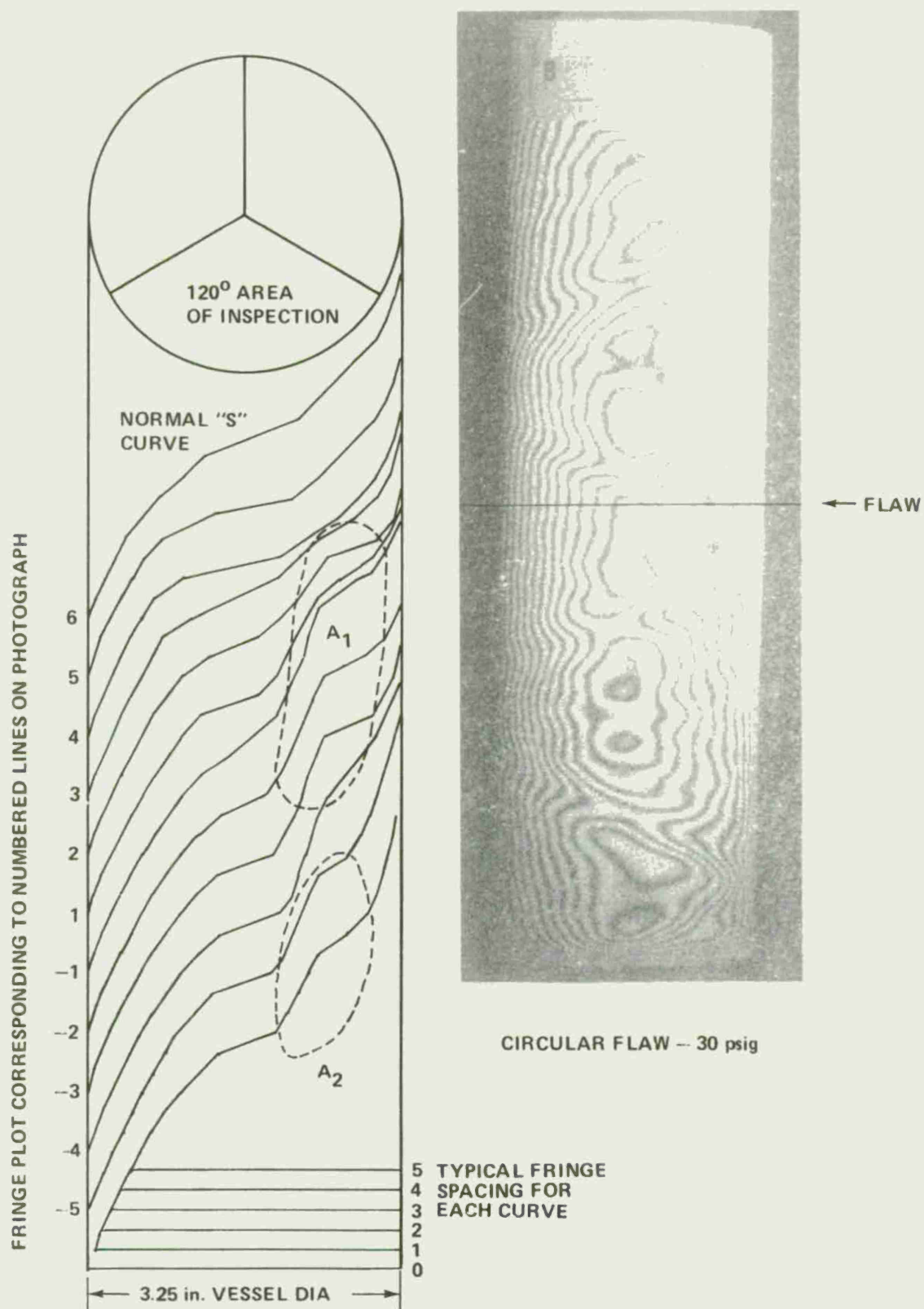


Figure 22. Flaw detection.

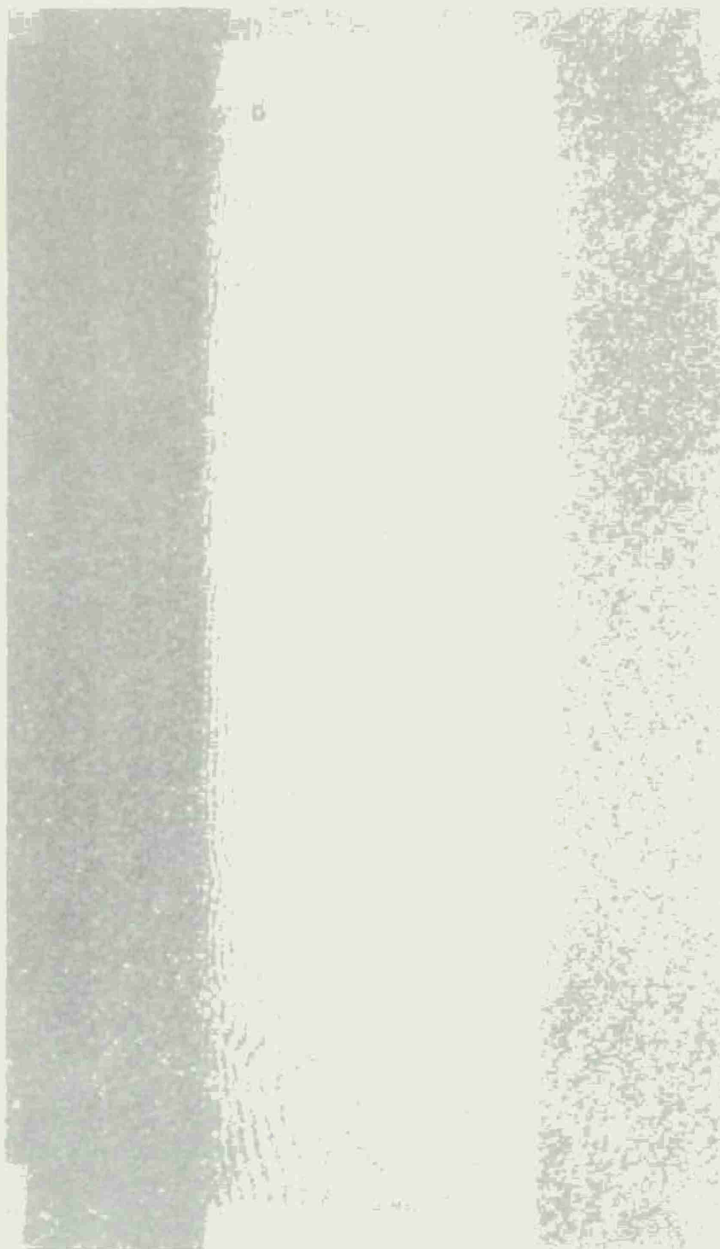


Figure 23. Cylinder with internal flaw at location A.

over the screen of a Tektronix 604 display scope by means of digital-to-analog converter under computer program control. The digital-to-analog converters have 10 bits of resolution and drive the X and Y axis of the display scope. The spot diameter of the scope is approximately 0.015 inch which permits approximately 300 resolvable spots to be laid down across the 5-inch dimension of the scope screen. The image of the screen is then focused on the film area to be scanned and, consequently, the scanning resolution on the film is approximately 1/300 of the long dimension of the scope image on the film. The light which is transmitted by the film is collected by a large condensing lens system and brought to focus on a 2-inch photomultiplier.

The components of the scanning unit are mounted on a heavy 2-meter optical bench so that they may be accurately and reproductively positioned on the optical bench with sufficient accuracy so that no additional focusing is necessary. The 4 × 5-inch film carrier attachment is loaded by placing the film to be scanned between the two glass plates. Accurate vertical and rotational positioning of the film may be maintained if the lower edge of the film is permitted to contact both of the positioning pins.

The data-collection cycle is controlled by the system software. The data cycle commences upon issuing an "intensify" command. This command causes the scope interface to issue an "intensify" pulse about 25 μ sec in duration. The light reaching the photocathode of the photomultiplier is converted to an electrical signal and amplified internally within the tube.

The output of the photomultiplier is amplified in an amplifier mounted in the base of the photomultiplier carriage. This signal is then sent to the computer cabinet in a coaxial cable for an additional stage of amplification.

After the last amplification, the signal is fed to a sample-and-hold circuit which is actuated by a "hold" signal generated about 20 μ sec after the "intensify" pulse. The output of the sample and hold is digitized by an 8 bit analog-to-digital converter (ADC). The conversion takes 4 μ sec. When the digitizing is complete, the ADC sends a "done" signal to the computer and the data are transferred to the computer under program control.

The Fringe Pattern Analyzer is equipped with a Tektronix 4601 hard-copy unit which prints out a graphical representation of the digitized fringe pattern. Comparison of the digitized fringe pattern with the original assures that the correct fringe pattern is being analyzed by the computer.

A film transparency of the fringe pattern in Figure 23 was digitized using the Fringe Pattern Analyzer. A computer graphical representation of the fringe pattern in the region of the flaws is shown in Figure 24. The scanning interval was 0.2 inch around the circumference of the cylinder. The fringe-density plots of the "U" curves corresponding to the "s" curves plotted by hand are shown in Figure 25. The flaws are both

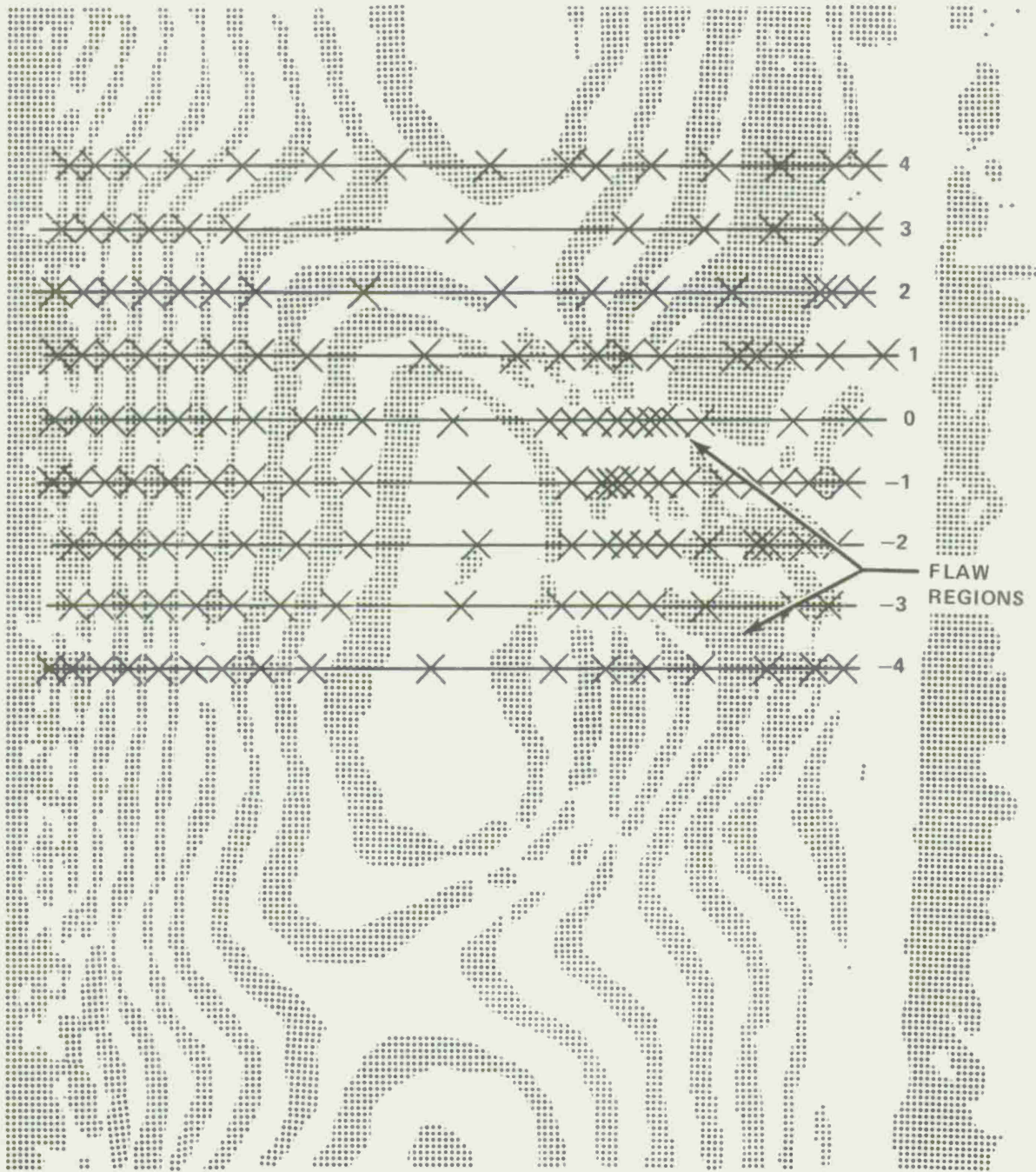


Figure 24. A computer graphics representation of the holographic fringe pattern from a composite cylinder.

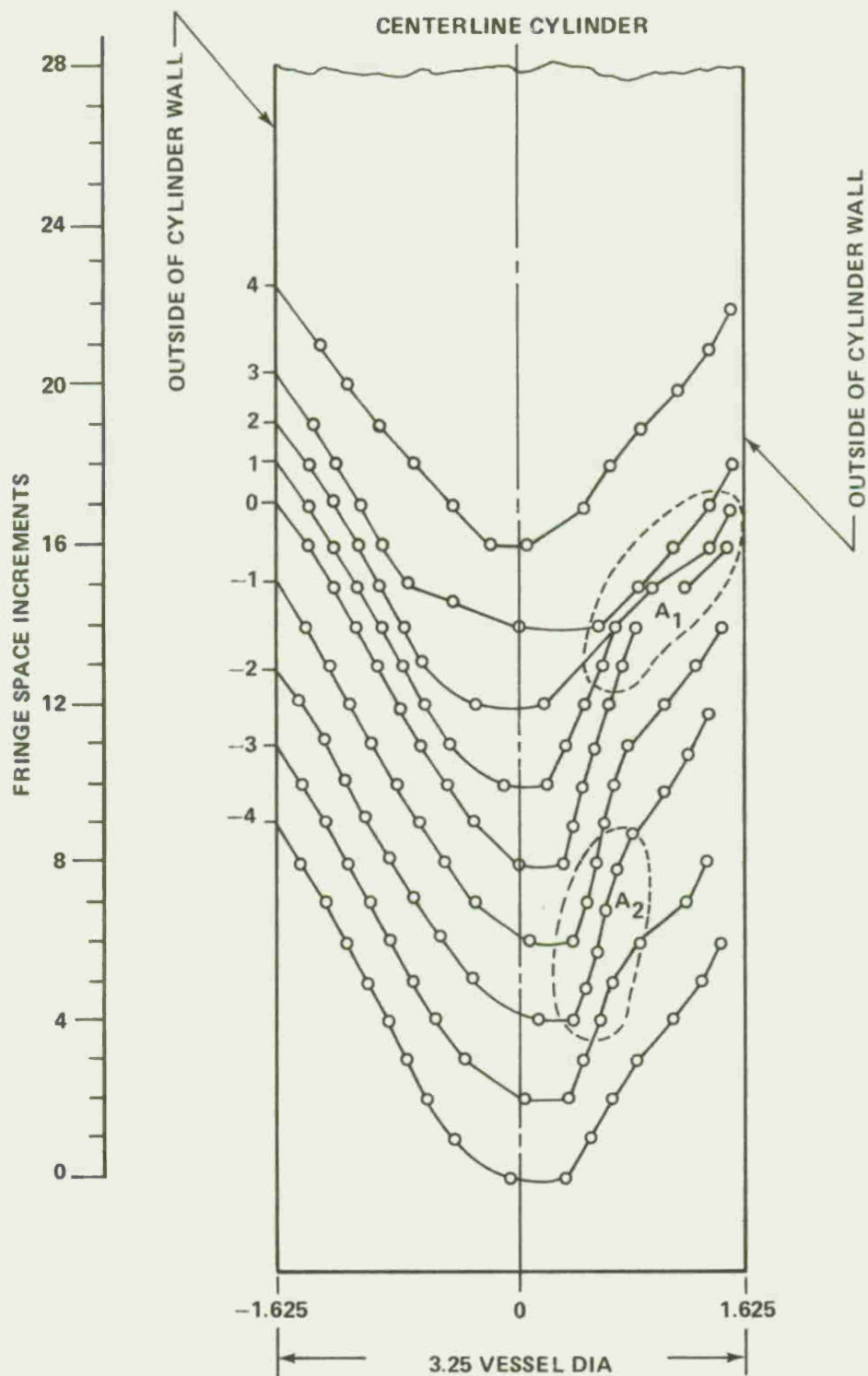


Figure 25. Fringe density plots by computer of the fringe patterns in Figures 23 and 24.

easily detected on the fringe-density plots. With the known scan interval and horizontal scale on the cylinder diameter the size of flaw can be determined. Flaw A_1 should be circular and slightly larger than the 0.5-inch-diameter teflon insert and A_2 is of unknown origin and size.

However, it is nearly 0.5 inch and is almost circular. The distortion in the shape of the nearly circular flaws is due to the curvature of the cylinder and the unequal scales in the horizontal and vertical directions. It should be noted that the scan intervals for the "S" and "U" curves are not the same.

Computerization of the data-reduction process has been demonstrated and this effort can be extended to cover the analysis by extending the computer software.

Other disbonds were manufactured into different pressure vessels and tested. For a disbond that occurred for several inches along the length, a typical example is shown in Figure 26. The disbond is above A in the picture. The technique as described previously for locating a small circular disbond will work also in this example.

Another disbond, that of going completely around the pressure vessel, was not easily detected. The point where the teflon tape (under A and about the center of the vessel, Figures 27 and 28) was easily noted and detected where the disbond was continuous; this was not detectable with the proposed technique. However, it is noted that such symmetrical flaws are not to be expected and that the beginning and end of such flaws are discernable.

In an effort to speed up the testing of such vessels other loading techniques are being examined to avoid the need of special removable plugs for pressurizing the vessels. Heating the vessel was examined as one alternative, where the disbond would cause different heat-transfer characteristics. To date this has not been effective. Vibrating the vessel is another type of load that is being examined. Results are in progress but not complete at this time.

Finally the next phase of this work is the need to establish what size flaw will weaken the vessels sufficiently to make them unsafe. This will have to come from testing vessels to failure that contain various-size flaws.

In summary, the technique of holography can be used for detecting flaws. The technique requires three views of each vessel to include 120° in each view. The results from the doubly exposed hologram can be recorded in real time and stored on video tape. The tapes can be digitized and flaws detected.

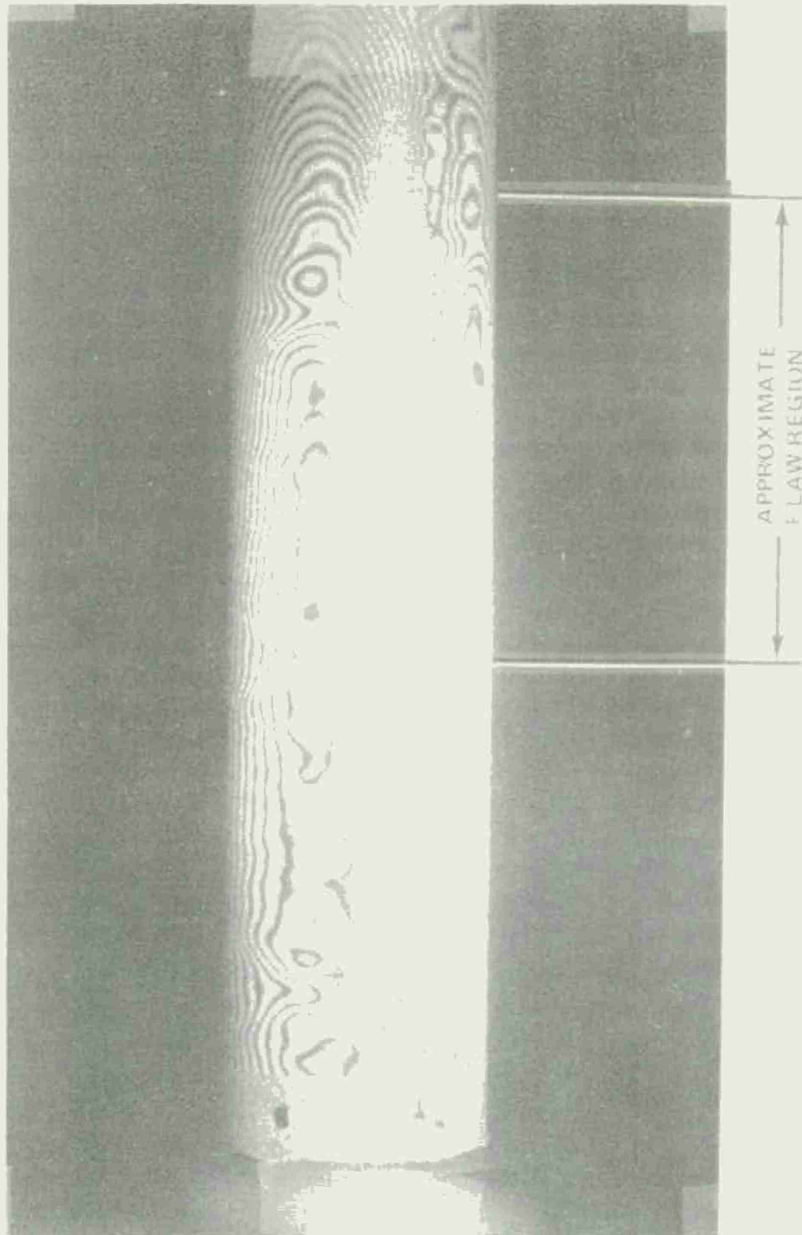


Figure 26. Longitudinal disbond in a composite cylinder.

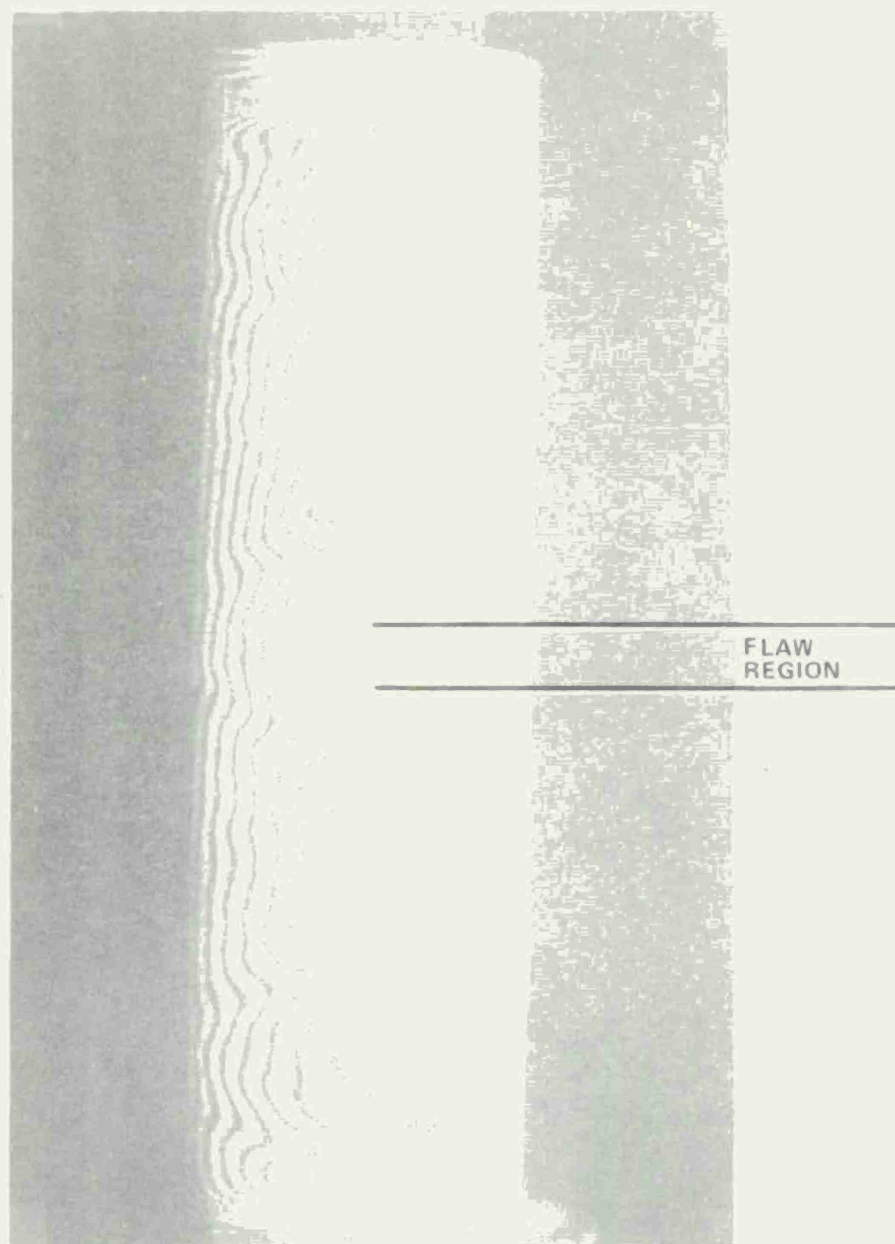


Figure 27. Circumferential disbond in a composite cylinder.

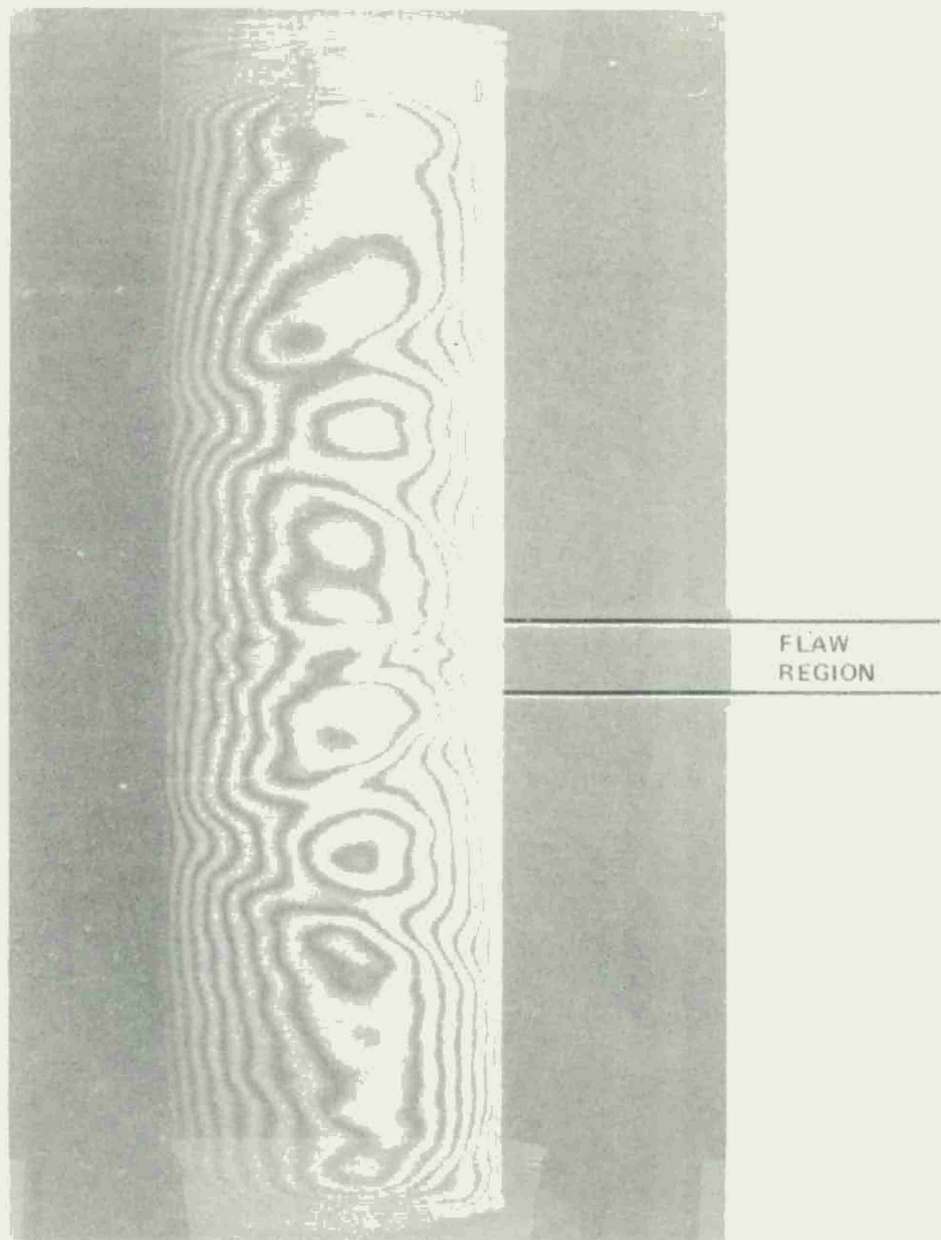


Figure 28. Circumferential disbond in a composite cylinder.

V. THE PREPARATION AND USE OF A PHOTOPOLYMER SYSTEM FOR REAL-TIME HOLOGRAPHIC APPLICATIONS

A. The Photopolymer System

A material capable of high-resolution image recording that needs no development is desirable for holography and in particular real-time recording. Of the numbers of unconventional photographic processes that have been used, including recording on thermoplastics and photore-sists, only photopolymers exhibit holographic-quality resolution and are self-developing. Initial research on such a system was conducted by Hughes Research Laboratories [9, 10, 11, 12, 13] under Air Force Office of Scientific Research sponsorship. The system presented is a modification of the imaging method described by the Hughes researchers.

Photopolymerization is defined as a process by which polymer molecules of high molecular weight are formed from fundamental building blocks, monomers, by the action of radiation in the presence of suitable catalysis or reaction initiators. Specifically, the mechanism of the image-forming reaction is a photoinitiated polymerization of a monomer solution. This aqueous monomer solution, comprised of barium acrylate, lead acrylate, and acrylamide, is stable and insensitive to light. It is sensitized by the addition of a second solution containing sodium benzene sulfinate and methylene blue. During irradiation of the mixed solutions, the ground-state methylene blue molecule being excited to a singlet state undergoes a transition to an excited triplet state by intersystem crossing. The excited triplet molecule of the methylene blue, a stronger oxidant than the ground-state molecule, oxidizes the sulfinate ions producing sulfinate-free radicals which subsequently catalyze the polymerization of the monomers present. The resulting polymer is an ionic cross-linked Ba-Ph acrylate and, due to its heavy metal ions, it has a high refractive index and low solubility. Thus, when plates containing the photosensitive solution are exposed in a hologram configuration, exposure leads to a higher refractive index in the exposed areas of the hologram than in the unexposed areas. After the exposure some monomer will diffuse from the unexposed areas to the polymer present in the exposed areas. If the spatial frequency of the hologram is high, this diffusion is completed within a very short period. The desensitization (fixing) of the system can be achieved by a second, overall exposure which polymerizes the remaining monomers. Since the local refractive indices depend on the rate of polymerization and monomer concentrations, the exposed regions will contain "more polymer" than the unexposed regions. Thus, the distribution of the polymer is modulated according to the spatial frequency of the hologram in terms of refractive index. The system is particularly useful for holographic applications due to this refractive index recording capability since the information is stored mostly as an efficient phase hologram rather than as a transparency hologram, i.e., when silver halide microcrystal emulsions are used for recording [14].

B. Preparation of Plates for Hologram Recording

The preparation of the plates initially consists of combining the required chemicals for the photopolymer system. The preparation of the monomer and sensitizing solutions giving the best performance is described in Section V.E. In order to sensitize the monomer solution for hologram recording, 10 parts of the monomer solution is mixed with 1 part sensitizing solution in the absence of red light - in this experiment the two components are mixed in the darkroom using a yellow darkroom lamp. The proper solution quantities are conveniently measured, mixed and dispensed using a 1 cc syringe. Although the two solutions (individually) have a long shelf-life, the photosensitive mixture has to be used within a few hours (in this experiment the mixture retained its high sensitivity for as long as 3 hours); otherwise, the mixture loses sensitivity by thermal reaction. The amount usually prepared is about 0.8 cc of solution, sufficient for four holograms. After mixing the two solutions, 0.2 cc of the mixture is placed in the middle of a 4 × 5-inch clear-glass plate. Then a second plate is placed over the "puddle" of mixture so that the liquid is evenly spread between the two glass plates by applying slight pressures with fingers (use cotton gloves to avoid finger prints on the plates) until the liquid film between the plates is free of air bubbles. The plates are then inserted into a plate holder specially designed for this experiment. To ensure the plates remain exactly in their initial position (within 1/10 of a wavelength), the design uses two adjustable tightening screws. After the plates are in position, they permanently remain there during the exposure, desensitization and real-time interferometry.

C. Recording Holograms

The optic setup for testing the photopolymer system performance is shown in Figure 29. A composite material cylinder, painted white for good reflectivity, was used as the object. The test cylinder used had a known disbond wrapped into it; this was done by inserting a teflon strip between layers of wrapping. A 50 mw He-Ne laser light source was used.

The best holograms were recorded with an object to reference beam ratio of 1/7 to 1/10. This was accomplished using a Gossen Lunasix lightmeter to maintain permanent optic data of:

- 1) Reference Beam Intensity 1/4
- 2) Reflected Object Beam Intensity . . . 10

The required exposure was found to be 20 seconds of He-Ne- laser radiation. About one-half of the total exposure is an induction period during which most of the sensitizing reactions (formation of free radicals) is quenched by inhibitors (mostly oxygen) present as impurities. Thus, a

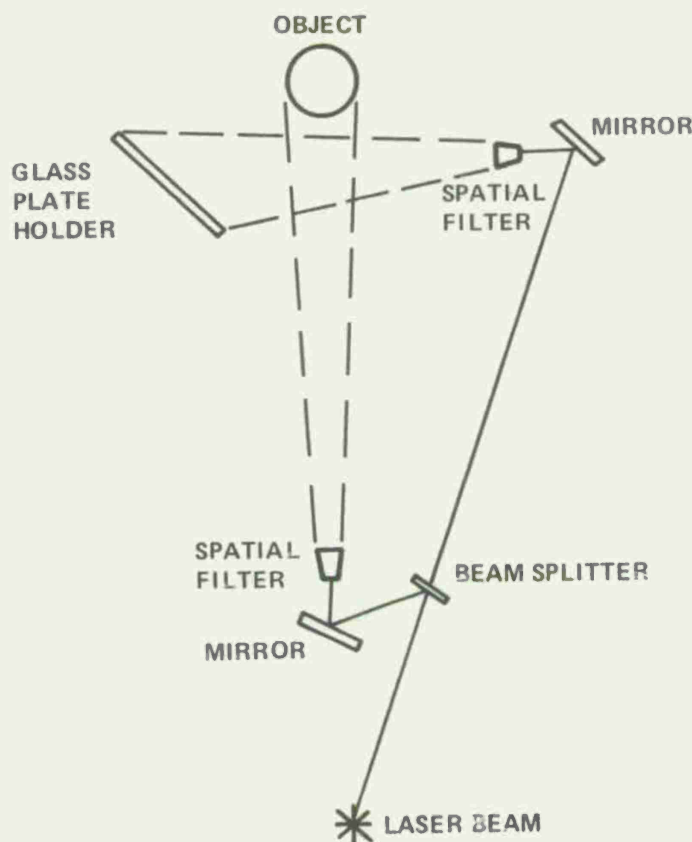


Figure 29. Optical arrangement for real-time interferometry.

pre-illumination of the plates can result in increase of the apparent sensitivity [15]. The adequate range of the exposure can be followed visually; following the induction period the plates exhibit the forming of a grayish "fog" or light scattering. This signals that the useful holographic exposure is attained and further exposure may result in loss of diffraction efficiency. After the holographic exposure, the plate must be fixed to continue with the single exposure real-time interferometry.

The fixing process is necessary to prevent image degradation from exposure to a playback beam or room light. The literature survey revealed a number of techniques that were applicable to this process. The first alternate technique was to flash the photopolymer holograms with either a xenon flashlamp [12], or a 15-to 30-second exposure to a 200-W mercury-arc lamp, with water and glass filter, or filter, or a "strobotac" strobe light also equipped with a red filter.

Both methods used in this experiment seemed to work rather well. The procedure for the flashbulb technique consisted of merely illuminating the holographic plates at a distance of several inches. The

procedure for the strobotac consisted of holding the unit at only a distance of about 1/2 inch from the plates and allowing the unit to flash continuously at lowest frequency for a period of roughly 2 minutes.

It has been determined that the index of refraction of the polymer is dependent on the irradiance of the exposing light [16], so that rapidly polymerizing the background increases the average index of refraction but does not wash out the spatial variations of the index of refraction resulting from the holographic exposure.

In all of the cases studied, the flash-fixing technique permitted exposing the hologram to a playback beam or to room light for 30-60 min. with little loss of diffraction efficiency. However, several hours exposure to room light reduced the diffraction efficiency to a few percent. The advantage of this technique is that it requires only a fraction of a second to fix the hologram so that it is compatible with holographic applications that require rapid access. Specifically, this technique should be applicable where self-developing and rapid access are necessary and where the hologram need be viewed for only an hour, at most. If a permanent record is desired, the reconstructed image can be photographed, or a more permanent fixing technique can be used after viewing the reconstruction.

The second fixing technique, called thermal fixing, is essentially permanent and may be used before or after viewing the reconstructed image, but it does not permit immediate access to the image. This technique involves keeping the hologram in the dark until the catalyst is completely deactivated. The deactivation of the catalyst is the result of chemical reaction between the monomer and catalyst. Satisfactory fixing was obtained by keeping holograms in the dark for one to two days. No attempt was made to measure the minimum time required but it is known that the desensitization reaction rate is dependent on the pH and the temperature of the photopolymer solution. However, lowering the pH to achieve fast thermal fixing will reduce the sensitivity of the photopolymer and reduce the sensitivity of the photopolymer and reduce the shelf-life of the mixed solutions [16].

After either of the fixing techniques the hologram is ready for real-time interferometry.

Also during the process of this experiment a double-exposure hologram was formed. The procedure included exposing the holographic plates to the initial 20 seconds of laser radiation and then, following the loading of the model to a prescribed pressure, exposing the plates to a second 20 seconds of laser radiation. After the second exposure the plates were fixed, using the No. 5 flashbulb. The result was a very high-quality double-exposure hologram with sharp, distinct fringe patterns.

D. Hologram Evaluation

Figures 30 through 50 display some typical real-time hologram interferograms prepared by the system described. The holograms from which these pictures were taken were clear in appearance, slightly scattering the light; have diffraction efficiencies up to 20% (in comparison with 1-4% for silver halide emulsion holograms) and resolution of about 2000 lines/millimeter [14]. Optical microscopy has revealed that the hologram is recorded both on the surface and in the volume of the material and that the surface modulation provides the dominant contribution to the diffraction efficiency [17].

Figures 30 and 31 were made from a hologram that had been flash-fixed after the initial 20-second exposure to the laser light. At the time of the flash, the cylinder was under zero pressure. The subsequent pictures were taken, viewing through the original glass plates, at the indicated pressure settings. The formation of the fringe patterns could be easily followed (visually) as the pressure inside the cylinder was increased. Also, the diminishing of the fringe patterns could be observed as the pressure decreased. Similar results were obtained by allowing the exposed hologram to set in the dark for 2 days thermal fixing.

In evaluation of the two fixing techniques, it is noted that the flash fixing is temporary. However, flash fixing provides faster access to the reconstructed image; it does not require chemical additives in the photopolymer solution, and it is more convenient to use. Thermal fixing does not permit rapid access, but it can be employed after a hologram has been temporarily fixed, so that the hologram can be played back immediately and then thermally fixed if the reconstruction is satisfactory. Thermally fixed holograms appear to be completely permanent.

E. Preparation of the Monomer and Sensitizing Solutions

(1) Preparation of the Monomer Solution. The preparation of the monomer solution is as follows:

- 1) 233 g acrylic acid is placed in a 1500 cc beaker equipped with a stirring motor and stirrer.
- 2) With continuous stirring, 169 g barium hydroxide crystals are added in small portions.
- 3) After complete dissolution, 65 g yellow lead oxide is added slowly in small portions.
- 4) After dissolving the lead oxide, a slurry of 300 cc distilled water and 294 g barium hydroxide crystals is added with continuous stirring. At this step some precipitation may occur.

5) After about 30 minutes stirring the pH of the solution is adjusted to 8-8.2 by adding acrylic acid or barium hydroxide crystals as needed. After the pH is adjusted, 50 g activated charcoal is added and the mixture is left to stand for 3 days. (This step is necessary to remove the polymerization inhibitor resulting from the acrylic acid).

6) The mixture is then filtered through coarse filter paper. The resulting solution is clear and has a specific density of 1.423 @ 25°C; yield is about 450-500 cc.

7) 30 g acrylamide is added for each 100 cc filtered solution with further stirring. After dissolving the acrylamide the specific density of the solution is about 1.344.

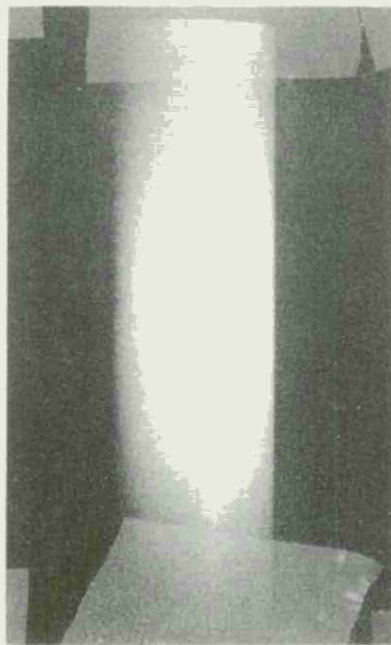
8) The solution is placed in a vacuum oven or desiccator equipped with a trap and water is removed at 35° to 40°C until the specific density of the remaining solution reaches 1.45 to 1.460.

The monomer solution prepared in this manner is a clear, stable viscous solution. Analysis indicates that it contains between 1.4-1.8M barium acrylate and 0.3-0.4M lead acrylate; pH should be about 8-8.2.

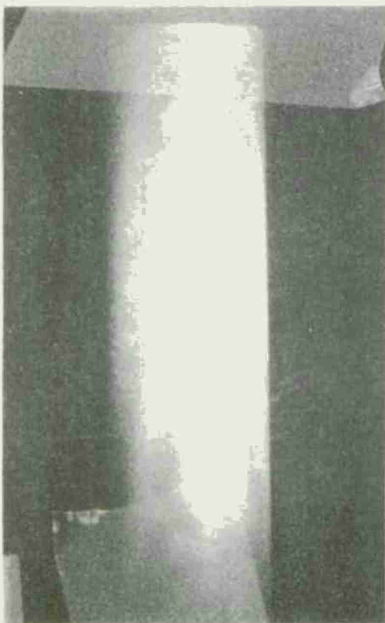
(2) Preparation of the Sensitizing Solution. The preparation of the sensitizing solution is as follows:

1) 25 g benzene sulfinic acid sodium salt is dissolved in 250 cc boiled (air-free) distilled water and 10 g charcoal mixed into the solution. After a few minutes the solution is filtered through filter paper.

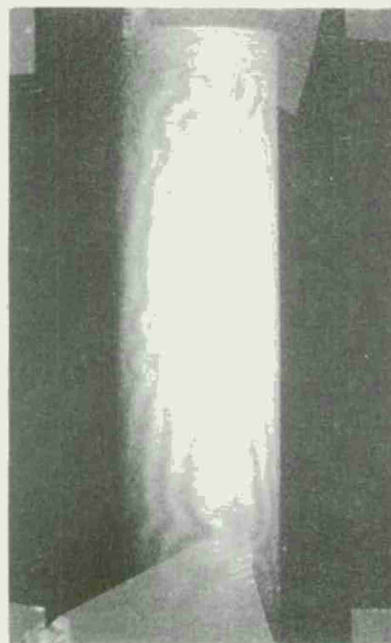
2) After filtering, 0.44 g methylene blue is added to each 100 cc solution. The solution must be kept in dark and stored in dark.



0 psig



5 psig



10 psig

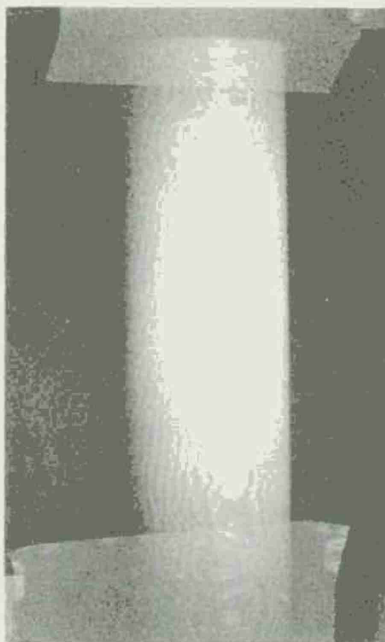
Figure 30. Composite cylinder with circumferential flaw at indicated loadings.



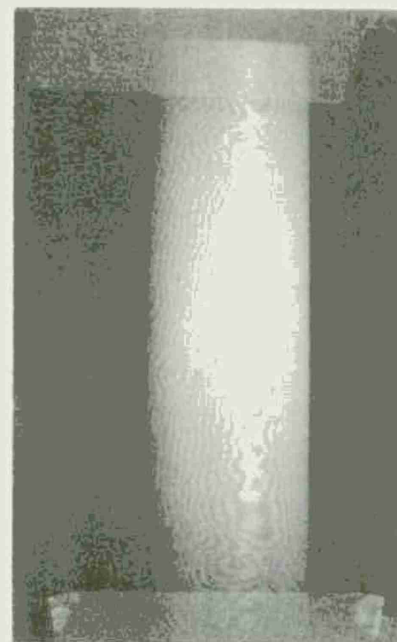
15 psig



20 psig



25 psig



30 psig

Figure 31. Composite cylinder with circumferential
flaw at indicated loadings.

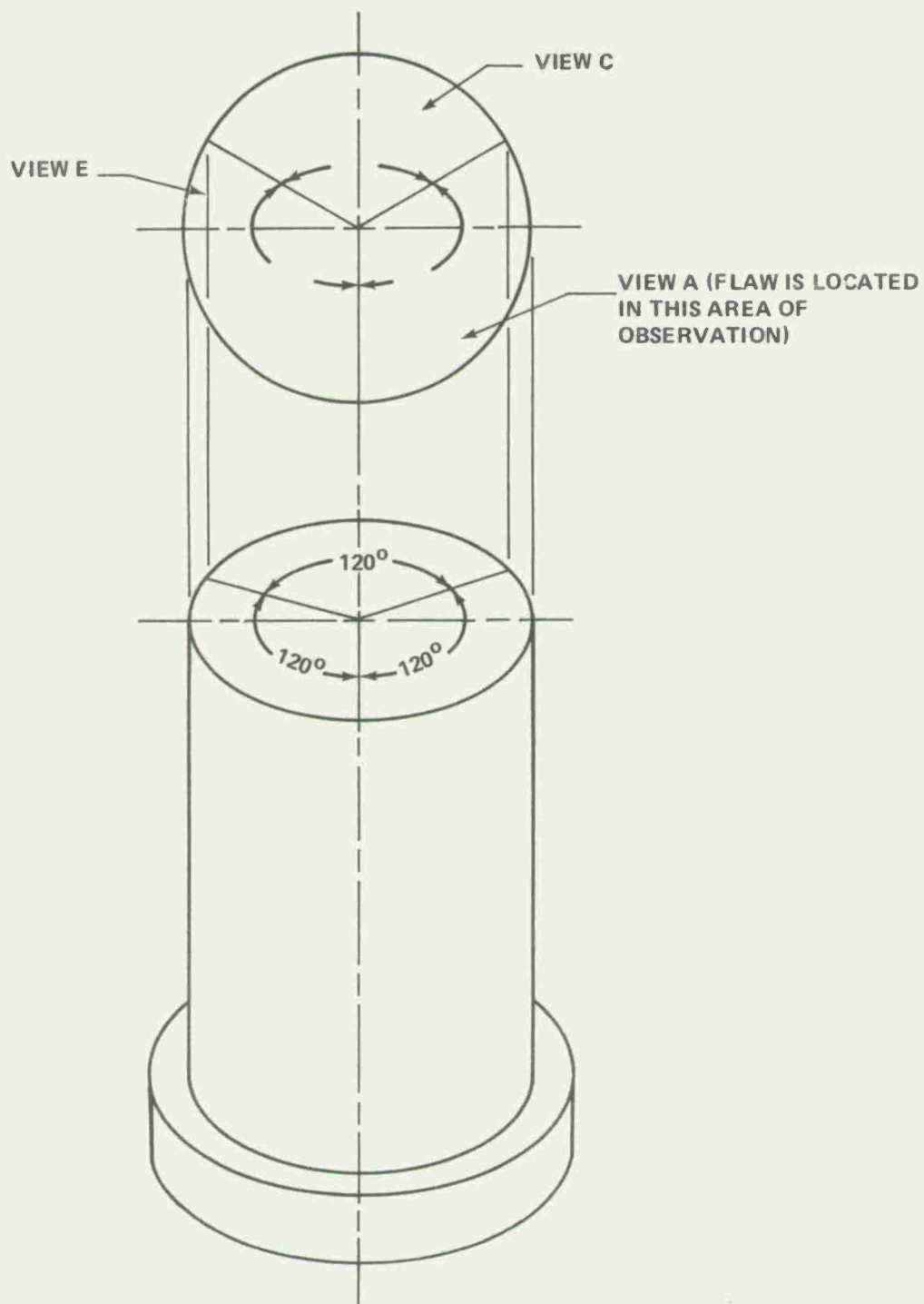


Figure 32. Schematic diagram illustrating the different positions of the cylinder with respect to the flaw location.

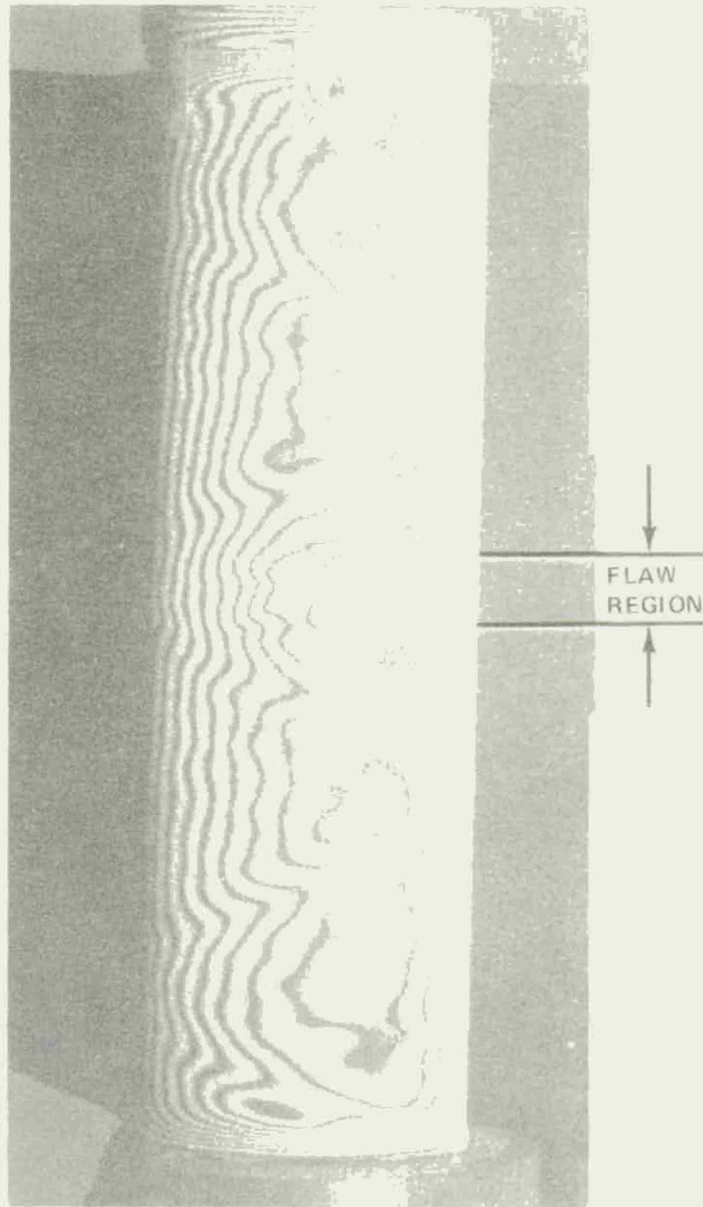


Figure 33. Circumferential flaw, view A 0-20 psig.

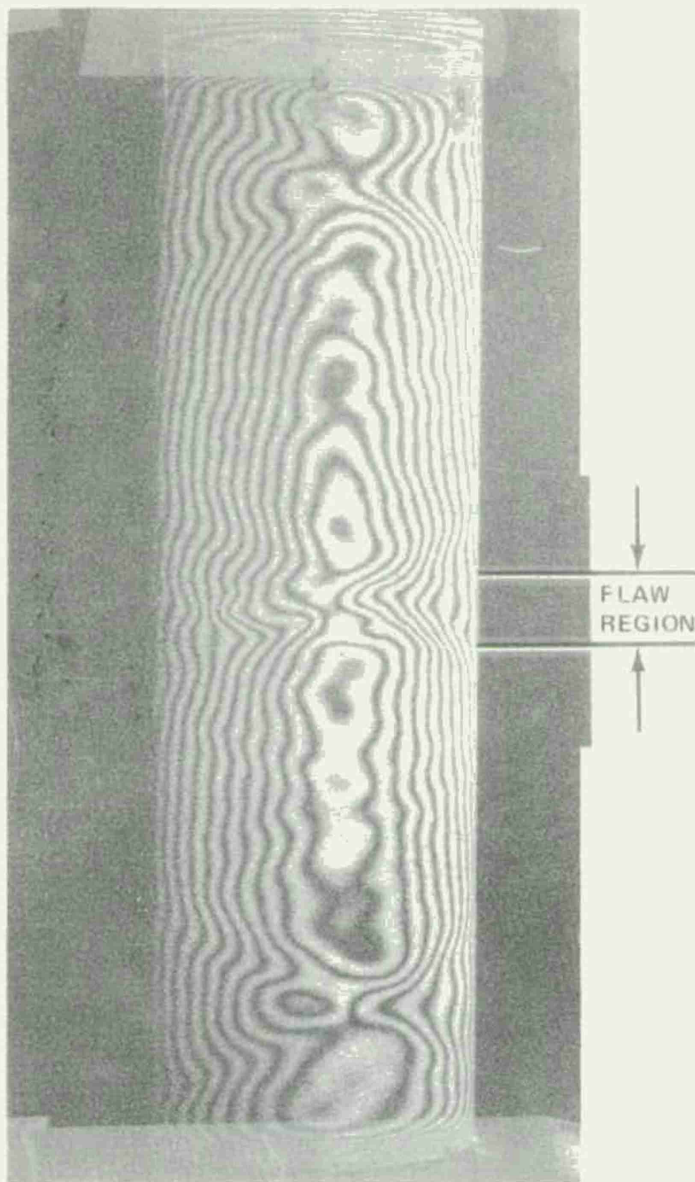


Figure 34. Circumferential flaw, view C 0-20 psig.

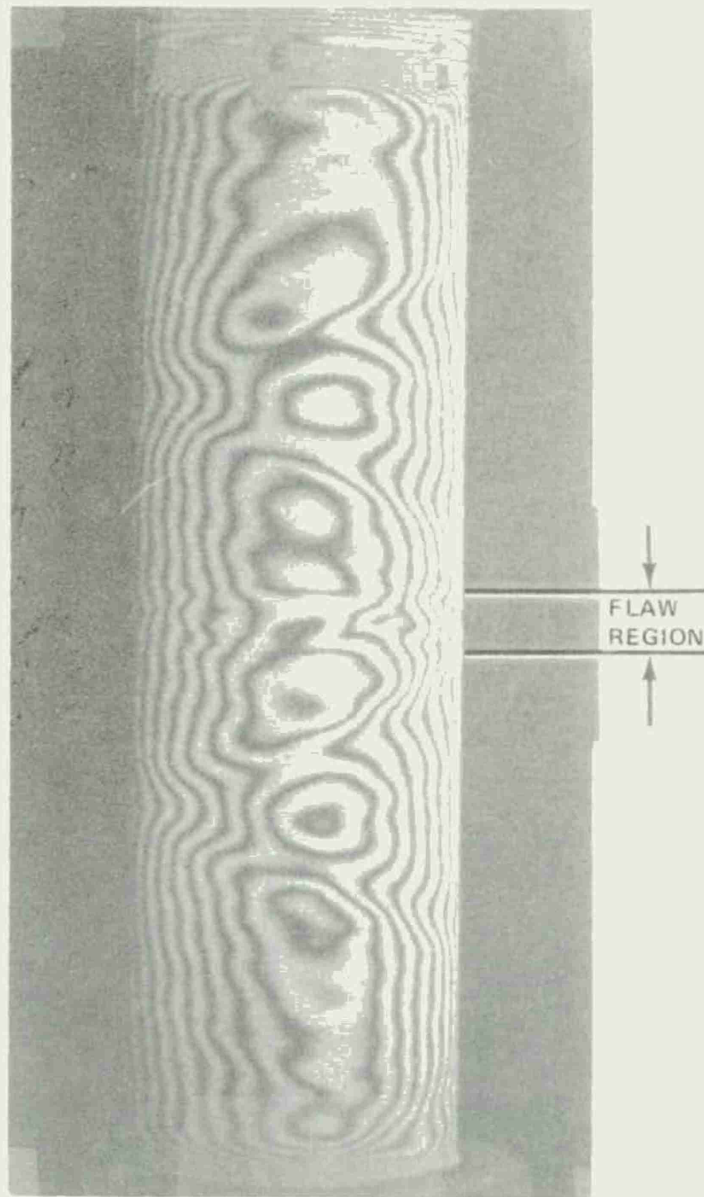


Figure 35. Circumferential flaw, view E 0-30 psig.

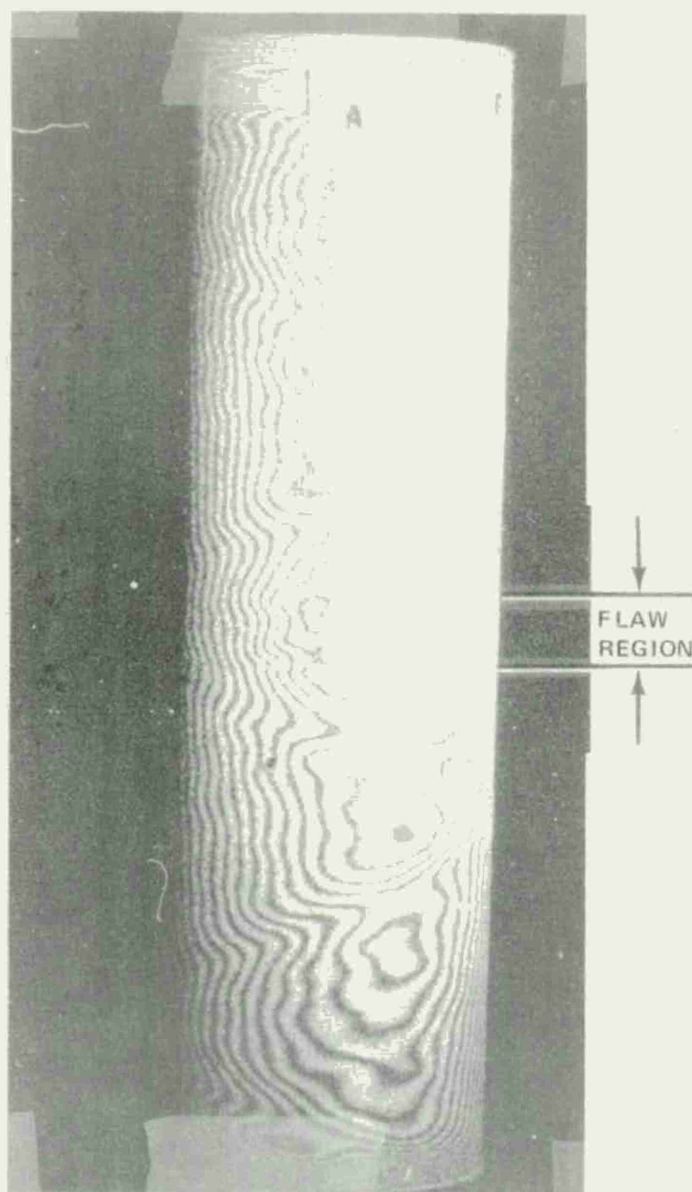


Figure 36. Circumferential flaw, view A 0-30 psig.

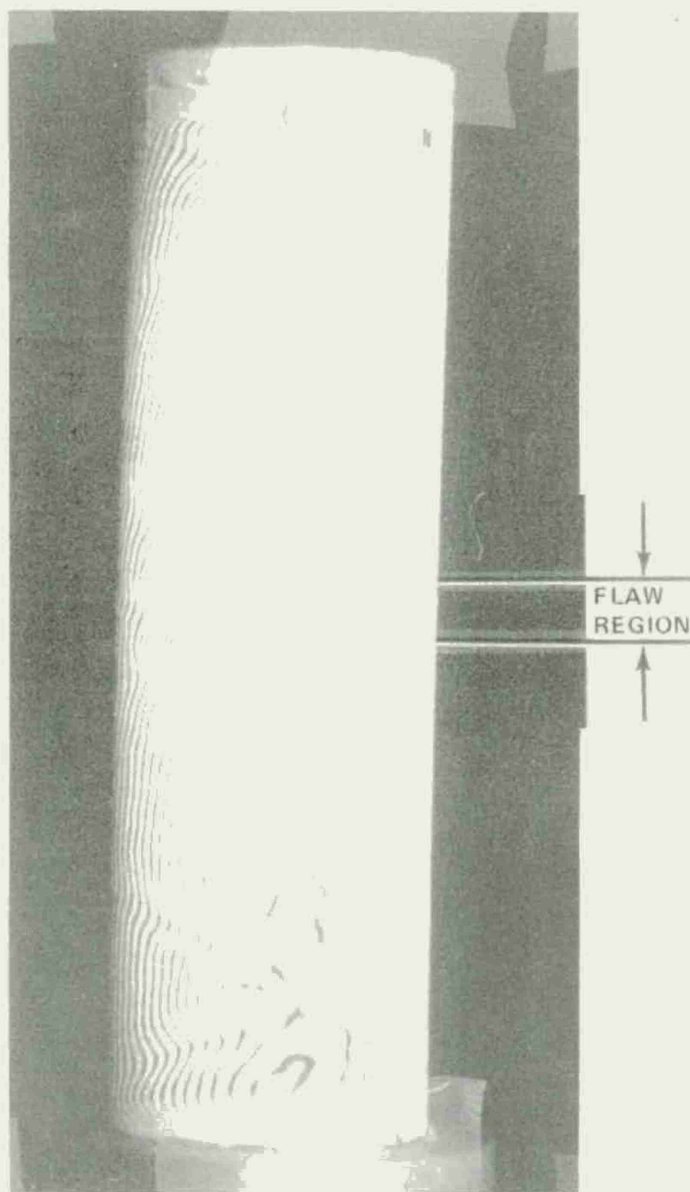


Figure 37. Circumferential flaw, view C 0-30 psig.

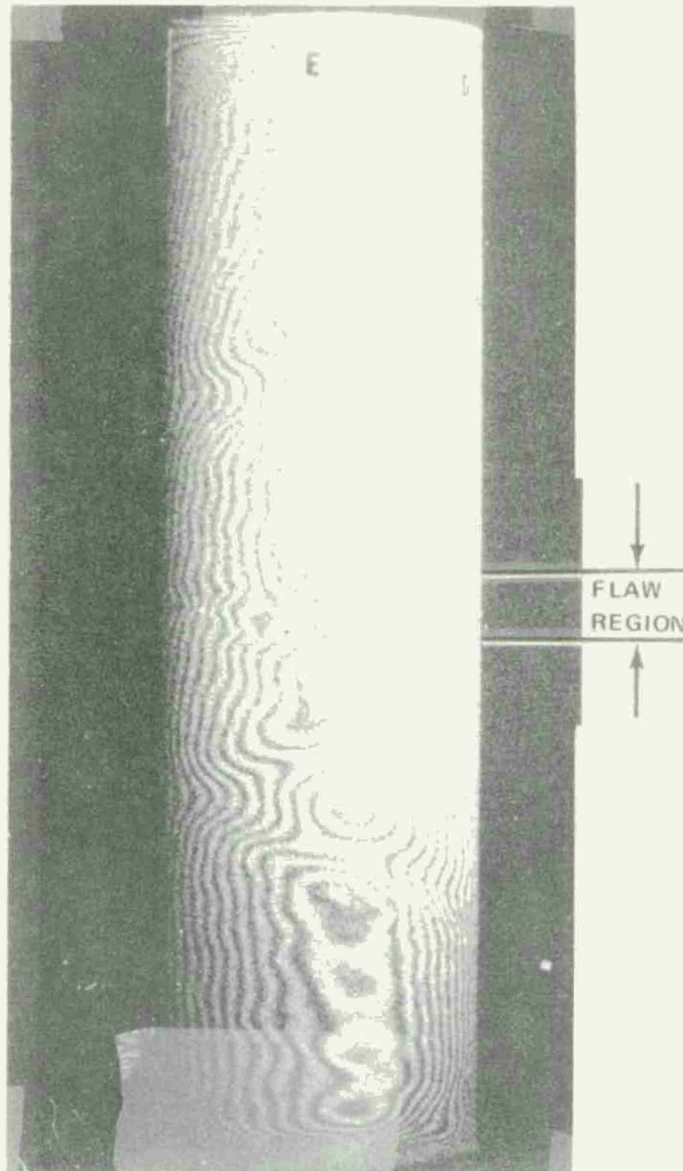


Figure 38. Circumferential flaw, view G 0-30 psig.

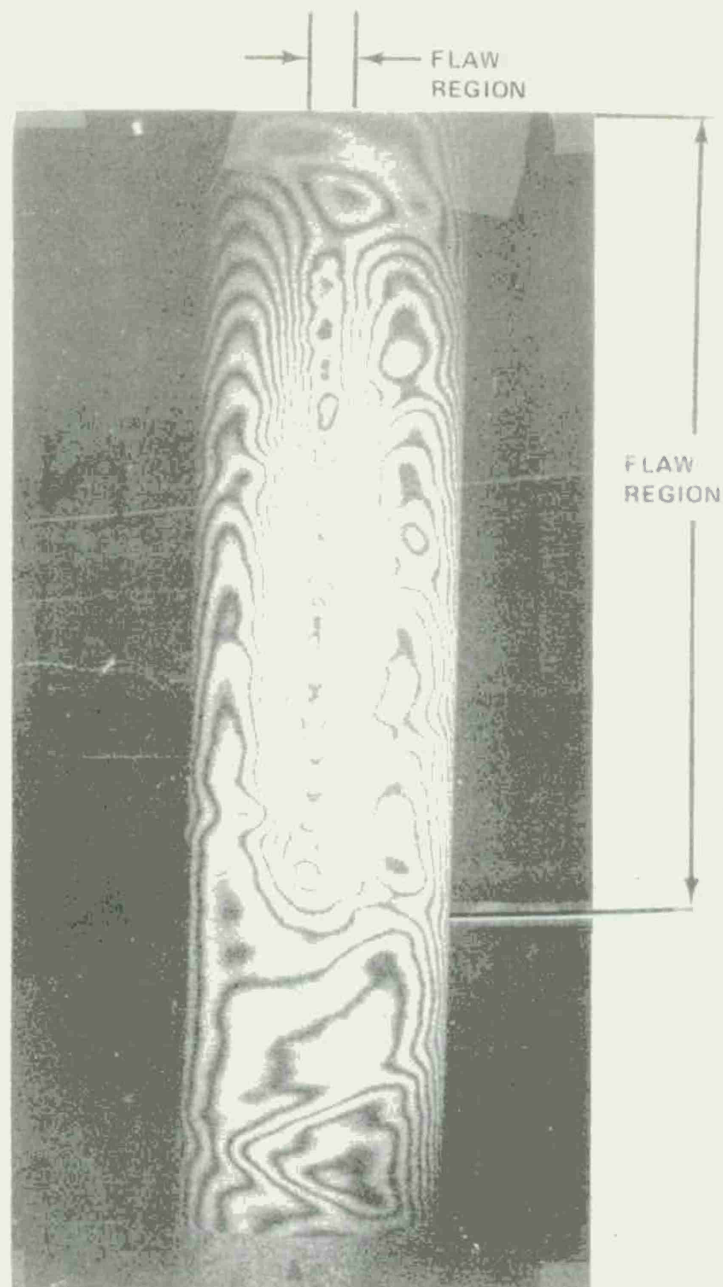


Figure 39. Longitudinal flaw, view A 0-20 psig.

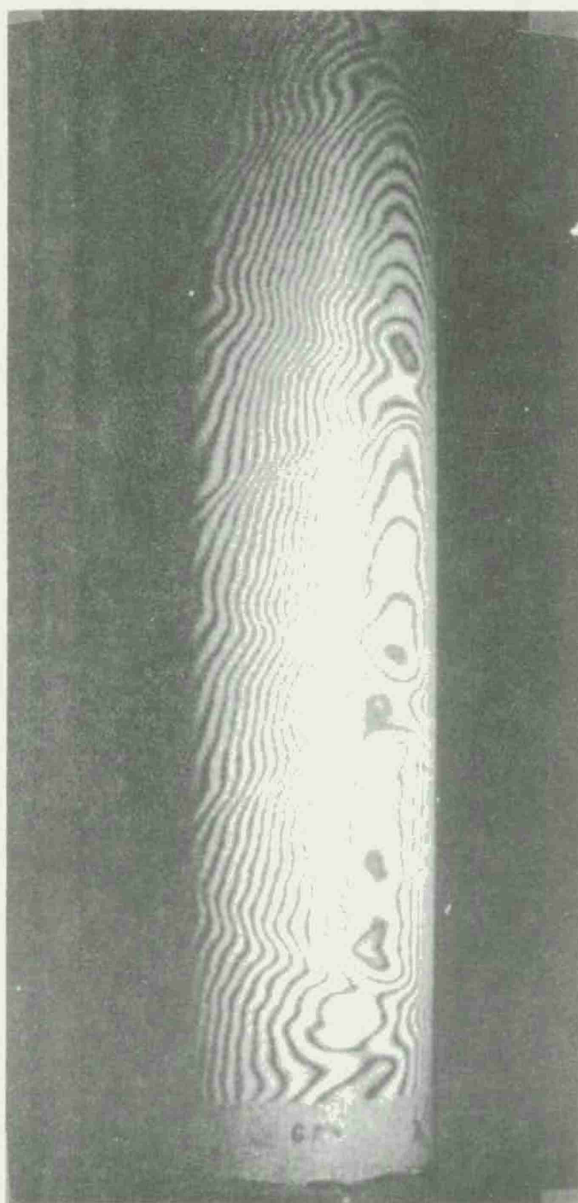


Figure 40. Longitudinal flaw, view C 0-20 psig.

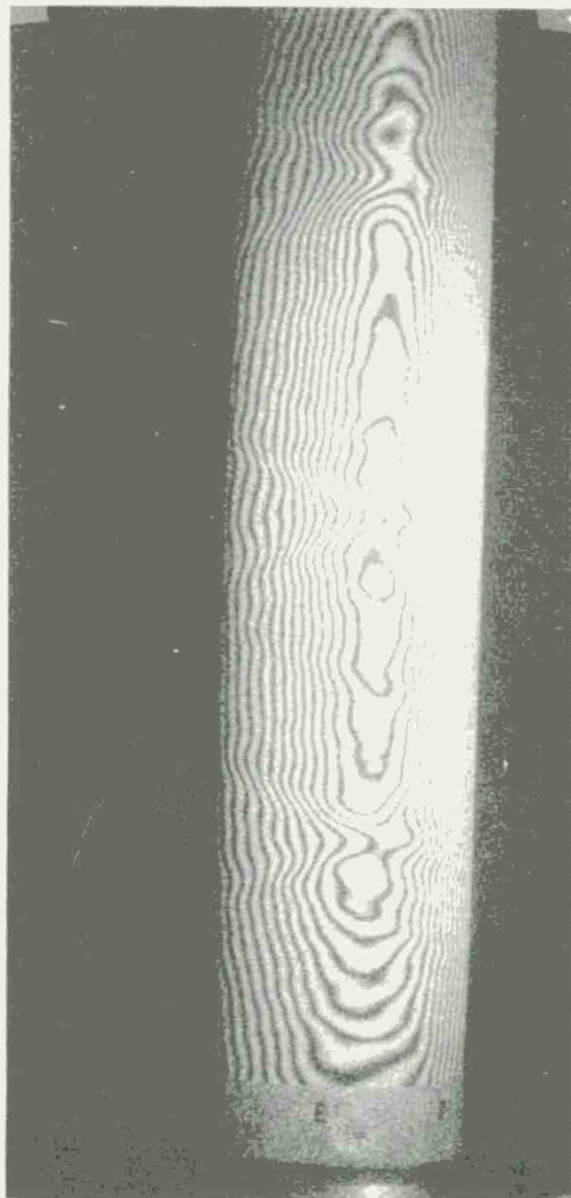


Figure 41. Longitudinal flaw, view E 0-20 psig.

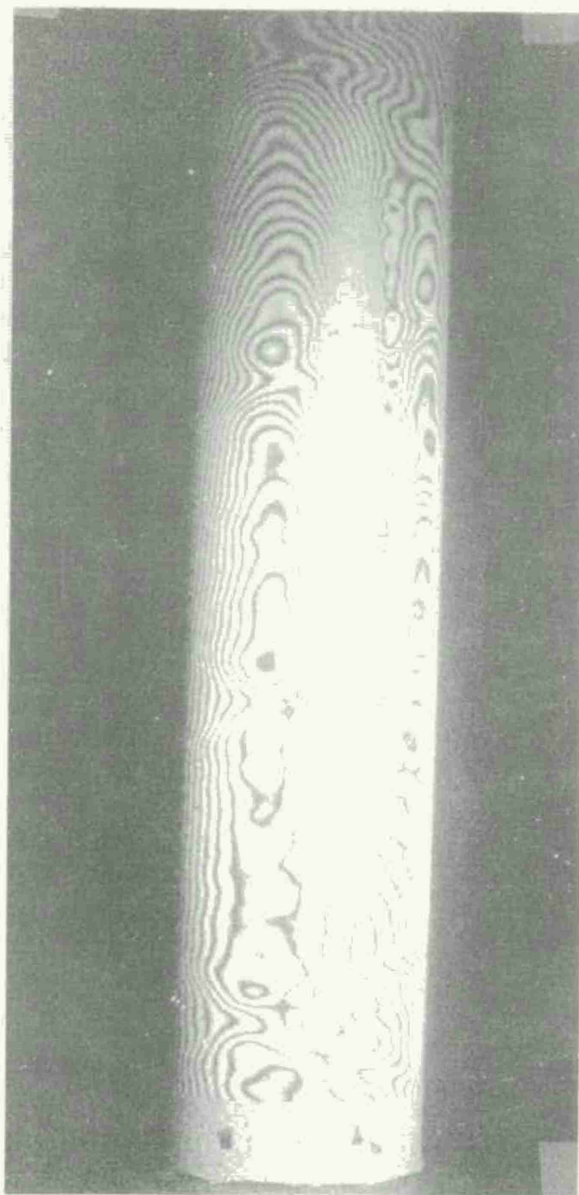


Figure 42. Longitudinal flaw, view E 0-30 psig.

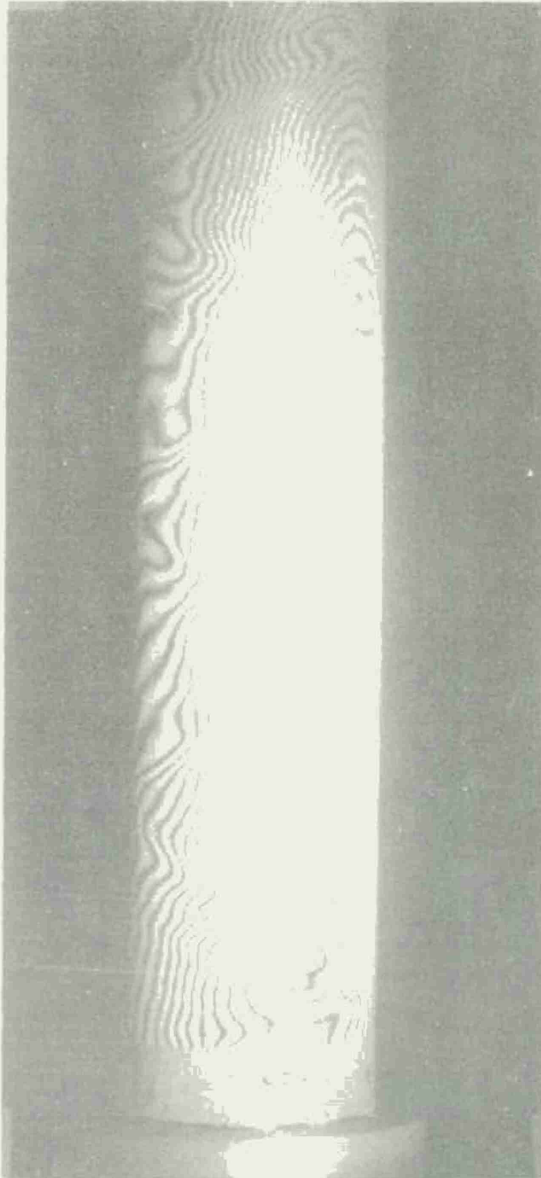


Figure 43. Longitudinal flaw, view C 0-30 psig.

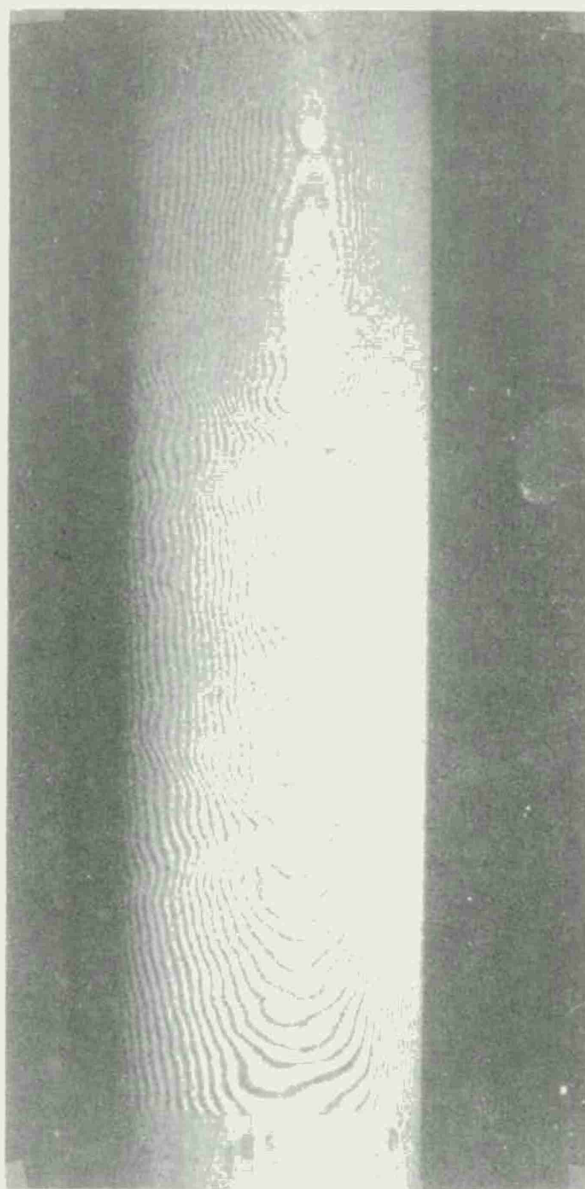


Figure 44. Longitudinal flaw, view E 0-30 psig.

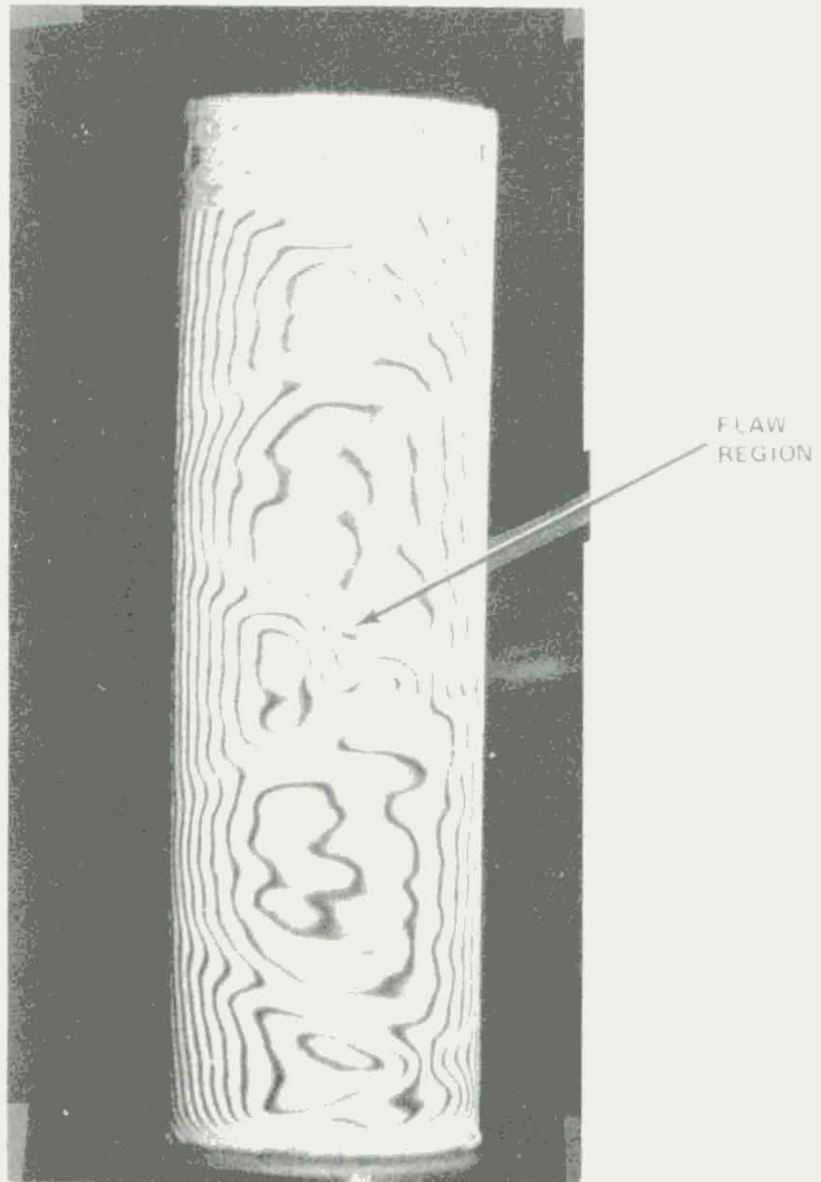


Figure 45. Circular flaw, view A 0-20 psig.

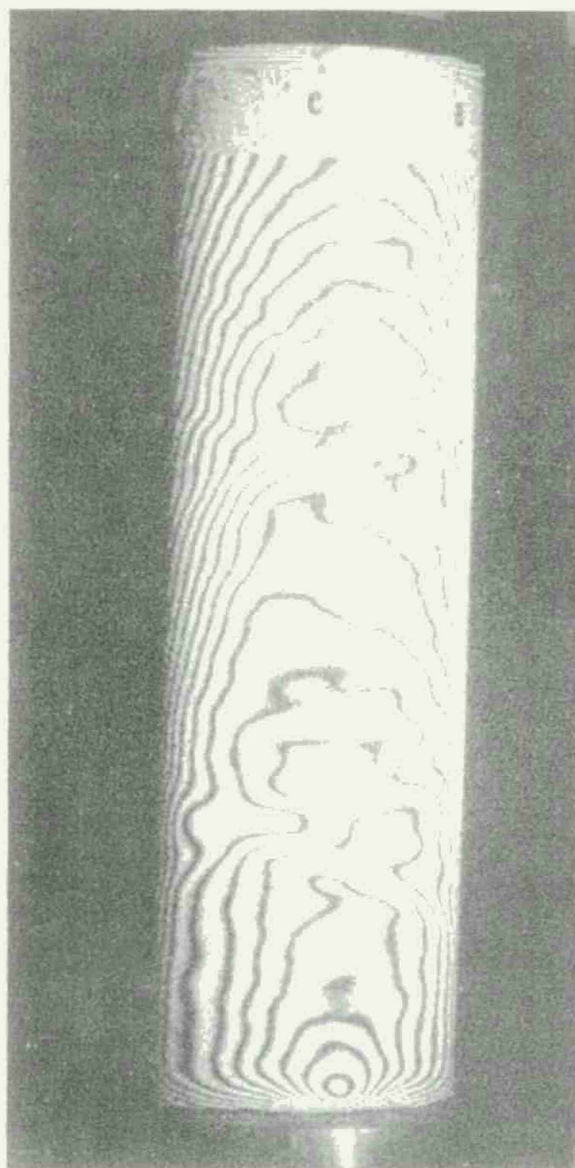


Figure 46. Circular flow, view C 0-20 psig.

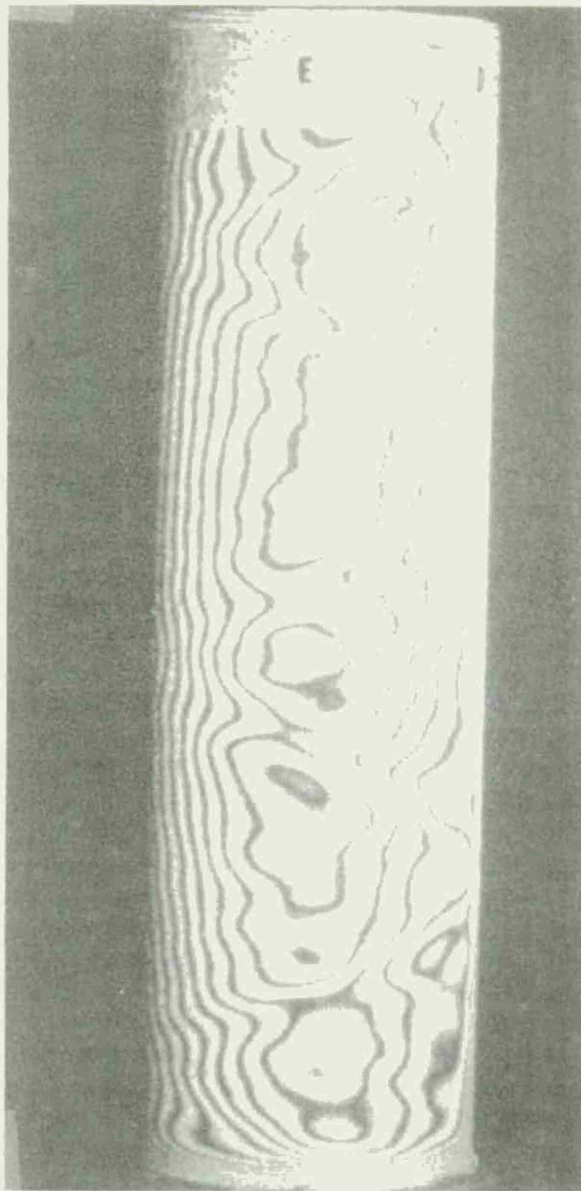


Figure 47. Circular flaw, view E 0-20 psig.



Figure 48. Circular flaw, view A 0-30 psig.

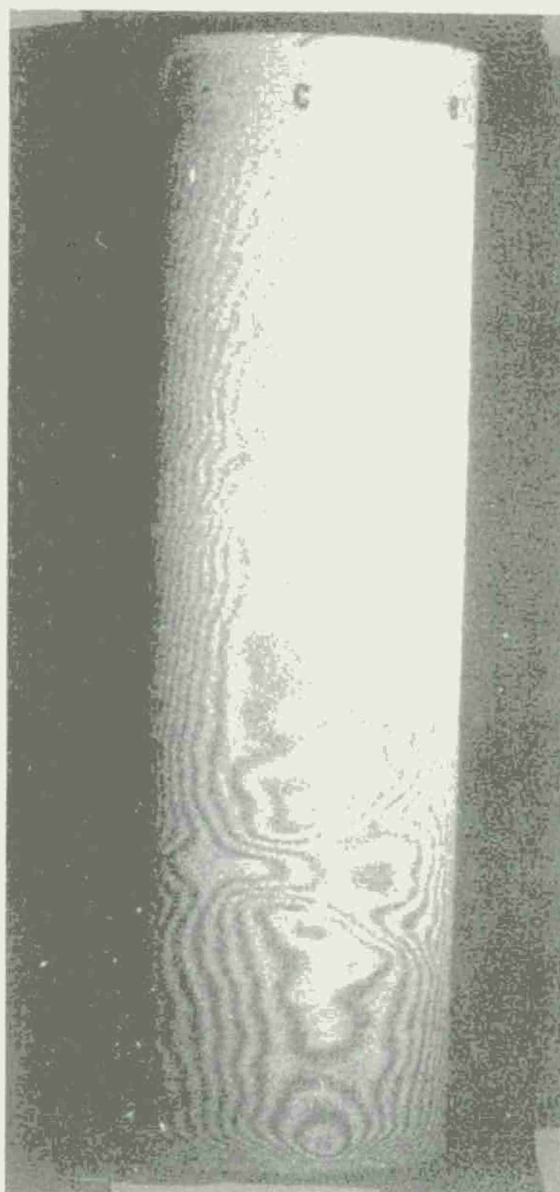


Figure 49. Circular flaw, view C 0-30 psig.

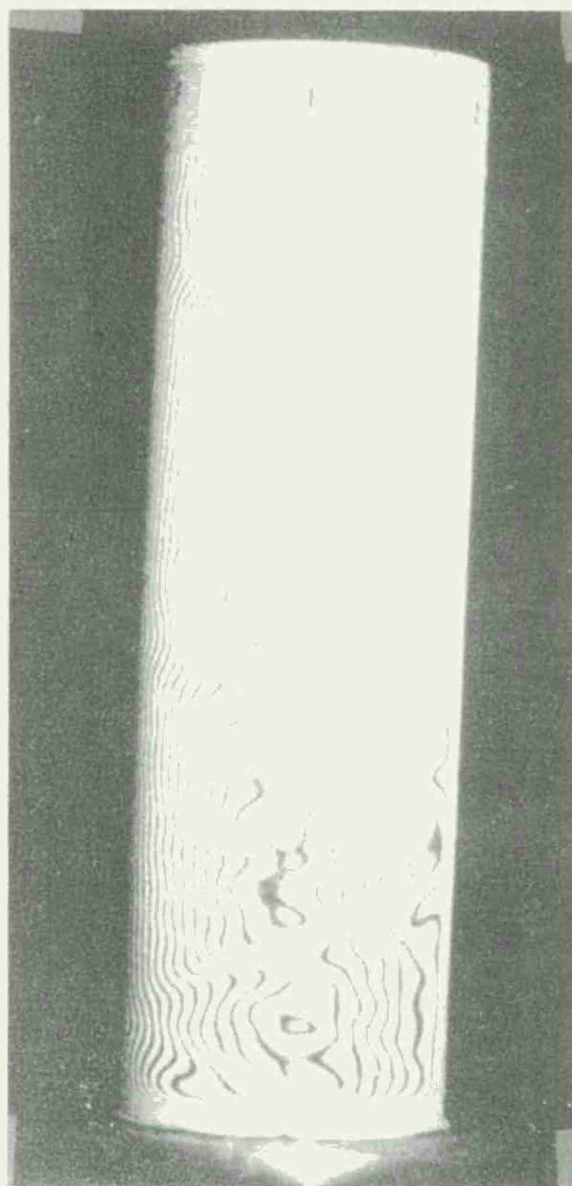


Figure 50. Circular flaw, view E 0-30 psig.

Chapter 4. SPECKLE INTERFEROMETRIC ANALYSIS USING YOUNG'S FRINGES

I. GENERAL

Several investigators have observed interference fringes from laser produced speckle displacements when a test piece is loaded [18, 19, 20, 21, 22]. Figure 51 illustrates the arrangement for recording the necessary double exposed film. One exposure with the model unloaded and one with the model loaded. Figure 52 illustrates how one can observe the data.

If each speckle point is thought of as an aperture emitting light, then several things take place. First, the aperture (speckle) produces interference patterns (Fraunhofer diffraction) due to its size; secondly, any nearby aperture will produce interference patterns with each other (Young's fringes). Finally, because the speckles (apertures) are numerous and randomly oriented the patterns mentioned previously are obscured by each other. Now, if a film record is made of the speckles of a test model and then the model loaded and the previous film record double exposed (Figure 51), fringes can be seen when coherent light is passed through a small region of the film and the diffraction pattern observed (Figure 52). This occurs because the film records the aperture (speckle) in the undeformed model state, then the apertures (speckles) are displaced in the loaded model and again recorded on the film. In a small region of the film the second recorded apertures are uniformly spaced relative to the first set and when a small coherent light beam is passed through this small region of film a diffraction pattern is observed identical to those observed when a small coherent light illuminates a small region in a diffraction grating. The pattern resulting comes from interference of the light as it passes through a small aperture (Fraunhofer diffraction) and interference from multiple apertures (diffraction grating) uniformly spaced in a small region.

The fringes, caused when light passes through a small rectangular slit (Fraunhofer diffraction), will initially be mathematically described. Then, the pattern resulting from two apertures will be described (Young's fringes) followed by a mathematical description of the fringe patterns of multiple apertures (diffraction grating) uniformly spaced.

II. FRAUNHOFER DIFFRACTION BY A RECTANGULAR APERTURE

Consider the arrangement shown in Figure 53. The lens serves to project onto a screen parallel rays that would otherwise diverge from the center line. A unit vector to the parallel light rays along OH is represented as

$$\bar{a}_1 = \ell \bar{i} + m \bar{j} + n \bar{k} \quad . \quad (32)$$

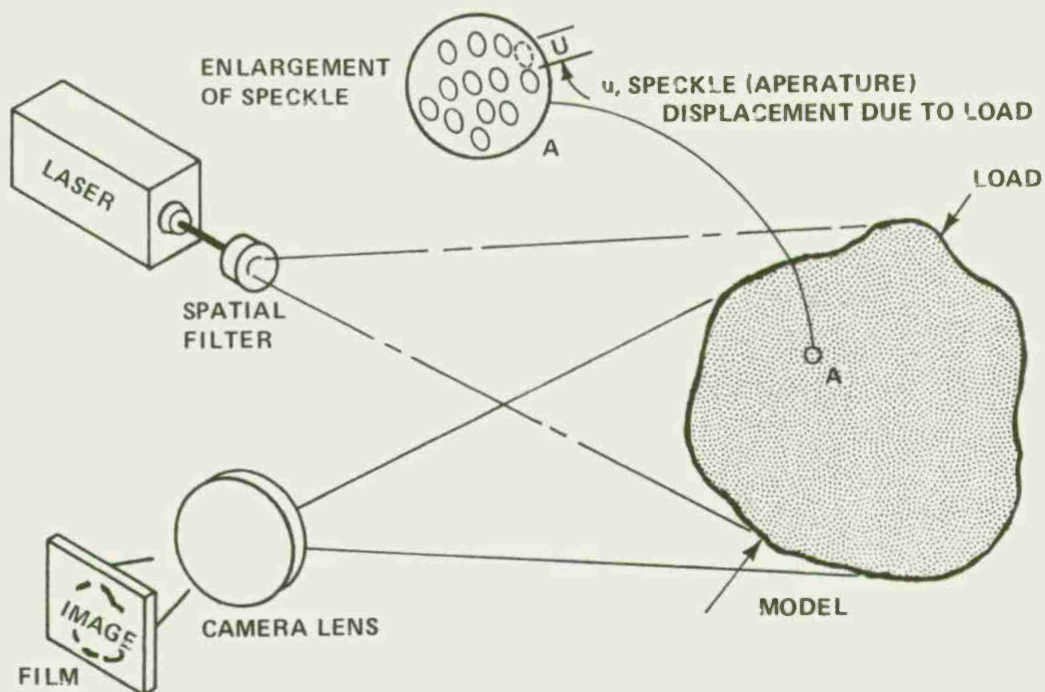


Figure 51. Collection of speckle interferometric data.

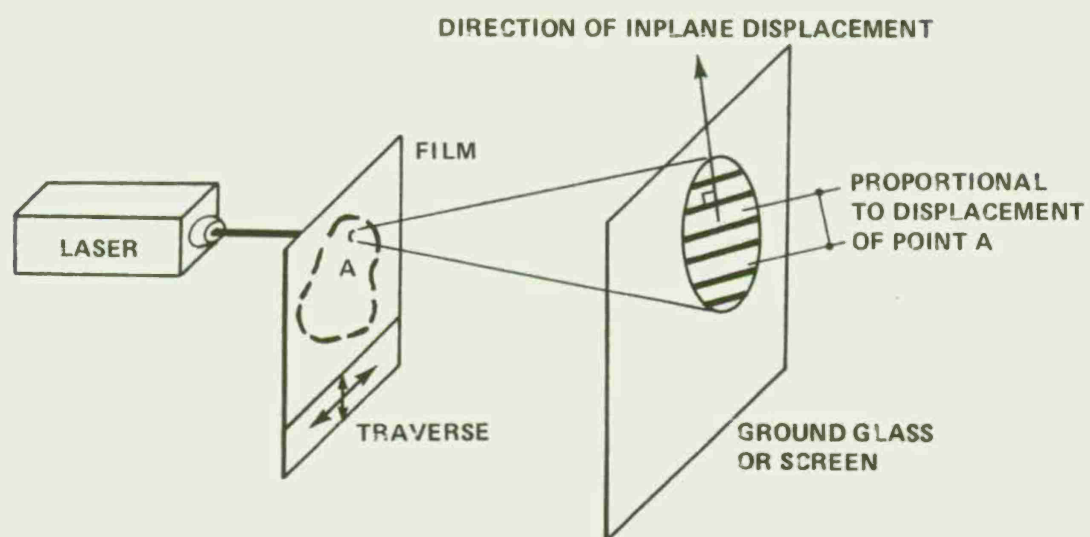


Figure 52. Data analysis

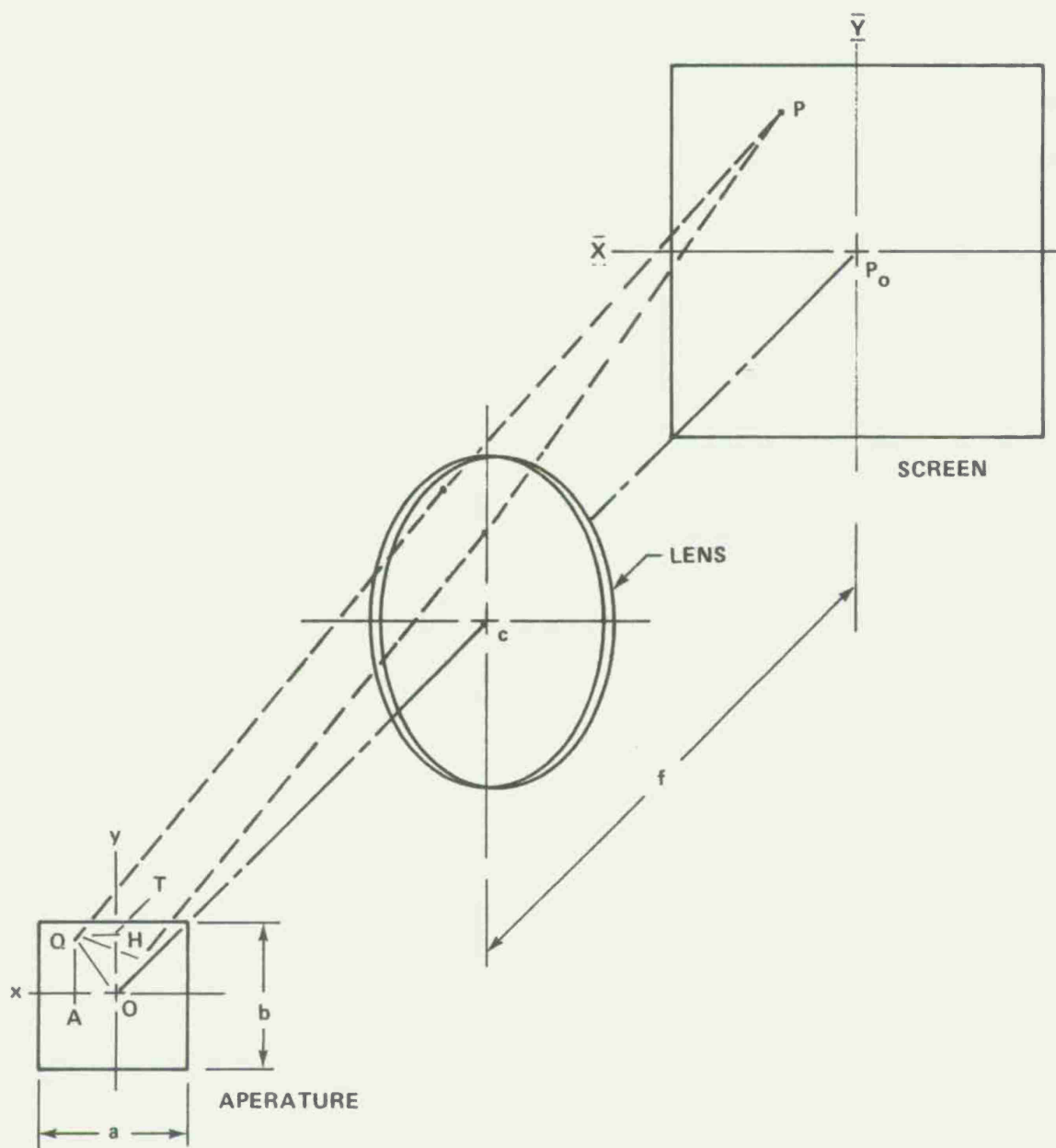


Figure 53. Rectangular aperture arrangement.

Note that \overline{OH} is on a ray passing through the center of the aperture. Point Q is a representative point in the plane of the aperture and located as

$$\overline{OQ} = x\overline{i} + y\overline{j} \quad . \quad (33)$$

The projection of \overline{OQ} on to the ray passing through the center is

$$\overline{OH} = \overline{OQ} \cdot \overline{a}_1 = x\ell + ym \quad . \quad (34)$$

Recall from lens theory that the optical path length QP and HP are equal. From this, rays OP and QP are out of phase by \overline{OH} .

Let the real part of

$$\overline{A} \text{Exp} [i (wt - \Phi)] dy dx$$

represent the optical disturbance at P due to secondary waves originating from the element of area $dy dx$ around the point O. Then, the optical disturbance at P due to secondary waves originating at a small region around Q is

$$\overline{A} \text{Exp} [i (wt - \Phi)] \text{Exp} [2\pi i (\frac{x\ell + ym}{\lambda})] dy dx \quad . \quad (35)$$

The intensity at P_o (being proportional to the square of the amplitude) is

$$I_o = (A a b)^2 \quad , \quad (36)$$

and the intensity at P is

$$I_P = I_o \left(\frac{\sin \frac{\pi \ell a}{\lambda}}{\frac{\pi \ell a}{\lambda}} \right)^2 \left(\frac{\sin \frac{\pi m b}{\lambda}}{\frac{\pi m b}{\lambda}} \right)^2 \quad . \quad (37)$$

To examine the intensity on the observation plane $(\overline{X}, \overline{Y})$, note that rays of light passing through the center of the lens (c) are not bent, thus are parallel to the original direction such as \overline{a}_1 . The coordinate locations \overline{X} and \overline{Y} are

$$\overline{X} = |\overline{CP}| \quad \ell \approx f\ell \quad . \quad (38)$$

$$\overline{Y} = |\overline{CP}| \quad m \approx fm$$

for small angles relative to the center line and where f is the lens focal length. Equation (37) now can be expressed as

$$I_P = I_0 \left(\frac{\sin \frac{\pi \bar{X}a}{\lambda f}}{\frac{\pi \bar{X}a}{\lambda f}} \right)^2 \left(\frac{\sin \frac{\pi \bar{Y}b}{\lambda f}}{\frac{\pi \bar{Y}b}{\lambda f}} \right)^2 \quad (39)$$

Since the variables \bar{X} and \bar{Y} are separable in Equation (39), only

$$\frac{dI_P}{d\bar{X}} = 0$$

and

$$\frac{dI_P}{d\bar{Y}} = 0$$

need be examined for maxima and minima on the \bar{XY} plane. Thus, maxima and minima occur when

$$\sin \frac{\pi \bar{X}a}{\lambda f} = 0 \text{ yielding } \frac{\pi \bar{X}a}{\lambda f} = 0, \pi, 2\pi, \dots, n_1\pi \quad (40)$$

$$\text{and } \frac{\tan \frac{\pi \bar{X}a}{\lambda f}}{\frac{\pi \bar{X}a}{\lambda f}} = \frac{\pi \bar{X}a}{\lambda f} \quad (41)$$

From Equation (40) the initial value of zero will produce a maximum in Equation (39). The other values from Equation (40), $\pi, 2\pi, \dots, n_1\pi$, give minima values of zero in Equation (39). The approximate values for the solution of Equation (41) are 0 (exact), $3/2\pi, 5/2\pi, \dots$. All values correspond to maxima.

III. FRAUNHOFER DIFFRACTION BY TWO NEAR-BY APERTURES

The interference pattern produced on a screen by two equal sized apertures is considered. As illustrated in Figure 54, consider two apertures located along the X axis and projected on the screen. Let $\ell = \sin \theta$, $m = 0$, and $n = \cos \theta$; thus, the optical disturbances at P from A_1 and A_2 are

$$\bar{E}_1 = \bar{A} a b \frac{\sin \frac{\pi \ell a}{\lambda}}{\frac{\pi \ell a}{\lambda}} \text{Exp} [i (wt - \phi_1)] \quad (42)$$

and

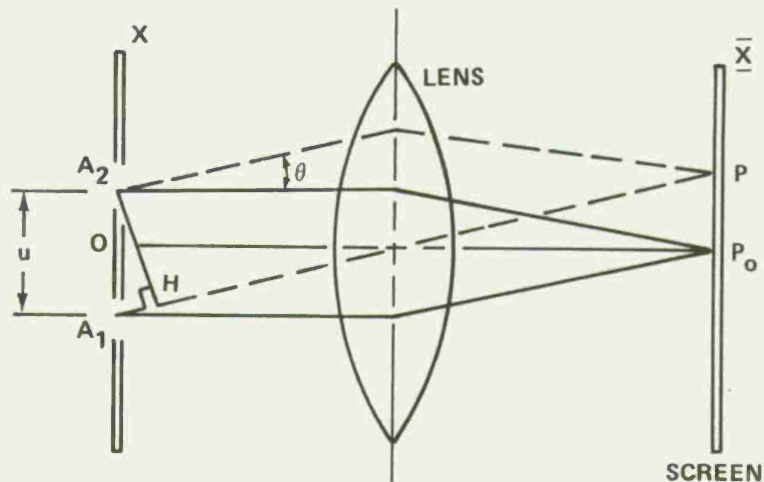


Figure 54. Fraunhofer diffraction by two apertures.

$$\bar{E}_2 = \bar{A} a b \frac{\sin \frac{\pi \ell a}{\lambda}}{\frac{\pi \ell a}{\lambda}} \text{Exp} [i (wt - \Phi_2)]$$

The phase difference at P due to the different path lengths A_1P and A_2P is

$$\frac{2\pi |\bar{A}_1\bar{H}|}{\lambda} = \frac{2\pi u \sin \theta}{\lambda} \quad (43)$$

Then

$$I_P = I_o \left(\frac{\sin \frac{\pi \ell a}{\lambda}}{\frac{\pi \ell a}{\lambda}} \right)^2 \cos^2 \left(\frac{\pi u \sin \theta}{\lambda} \right) =$$

$$I_o \left(\frac{\sin \frac{\pi a \bar{X}}{\ell \lambda}}{\frac{\pi a \bar{X}}{\ell \lambda}} \right)^2 \cos^2 \left(\frac{\pi u \sin \theta}{\lambda} \right) \quad (44)$$

where I_0 is the intensity at the center of the screen (P_0) and ℓ is approximated as \bar{X}/f and also equals $\sin \theta$.

Equation (44) contains the diffraction term as noted for a single aperture and now an interference term, $\cos^2 \left(\frac{\pi u \sin \theta}{\lambda} \right)$, due to two apertures close together. Emphasis is called to the cosine function where zero intensity occurs if

$$u = \pm \frac{\lambda}{2 \sin \theta} \cong \pm \frac{\lambda f}{2\bar{X}}$$

$$u = \left(\frac{3}{2}\right) \frac{\lambda}{\sin \theta} \cong \pm \frac{3}{2} \frac{\lambda f}{\bar{X}} \quad (45)$$

$$u \cong \pm \left(\frac{2m_1 - 1}{2}\right) \frac{\lambda f}{\bar{X}} \text{ for } m_1 = 1, 2, 3, \dots$$

Also, if u becomes less than $a/2$ then the dominating function is the sine function. The distance between apertures is the information that will give the displacement; therefore, if the total displacement at a point is less than one-half the aperture (speckle) size then this technique has limitations. A representative speckle size is 300 microinches and 150 microinches should be thought of as a minimum limitation on total displacement at a point.

IV. INTERFERENCE PATTERNS FROM MULTIPLE APERTURES

Consider the final case of multiple apertures, the same size and equally spaced about the X-axis as illustrated in Figure 55. The optical disturbance at P due to the first aperture is given by Equation

(42) and for the N^{th} aperture as

$$\bar{E}_N = \bar{E}_{n+1} = \bar{A}ab \frac{\sin \frac{\pi \ell a}{\lambda}}{\frac{\pi \ell a}{\lambda}} \text{Exp} \left[i \left(\omega t - \phi_1 + \frac{2\pi n u \sin \theta}{\lambda} \right) \right] \quad (46)$$

The total optical disturbance from N diffracted beams is

$$\bar{E}_P = \bar{E}_1 + \bar{E}_2 + \bar{E}_3 + \dots + \bar{E}_N \quad (47)$$

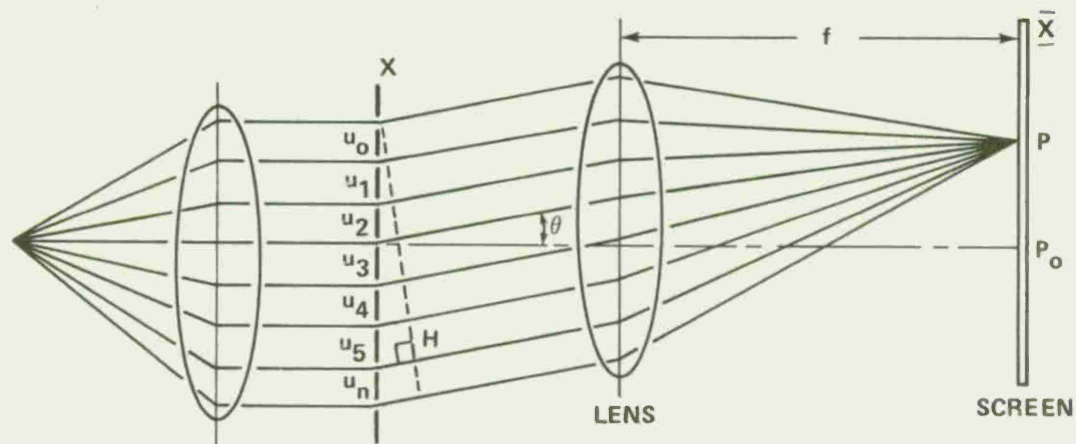


Figure 55. Multiple apertures.

$$I_p = (Aab)^2 \left[\frac{\sin \left(\frac{\pi a \sin \theta}{\lambda} \right)}{\left(\frac{\pi a \sin \theta}{\lambda} \right)} \right]^2 \left[\frac{\sin \left(\frac{N \pi u \sin \theta}{\lambda} \right)}{\sin \left(\frac{\pi u \sin \theta}{\lambda} \right)} \right]^2$$

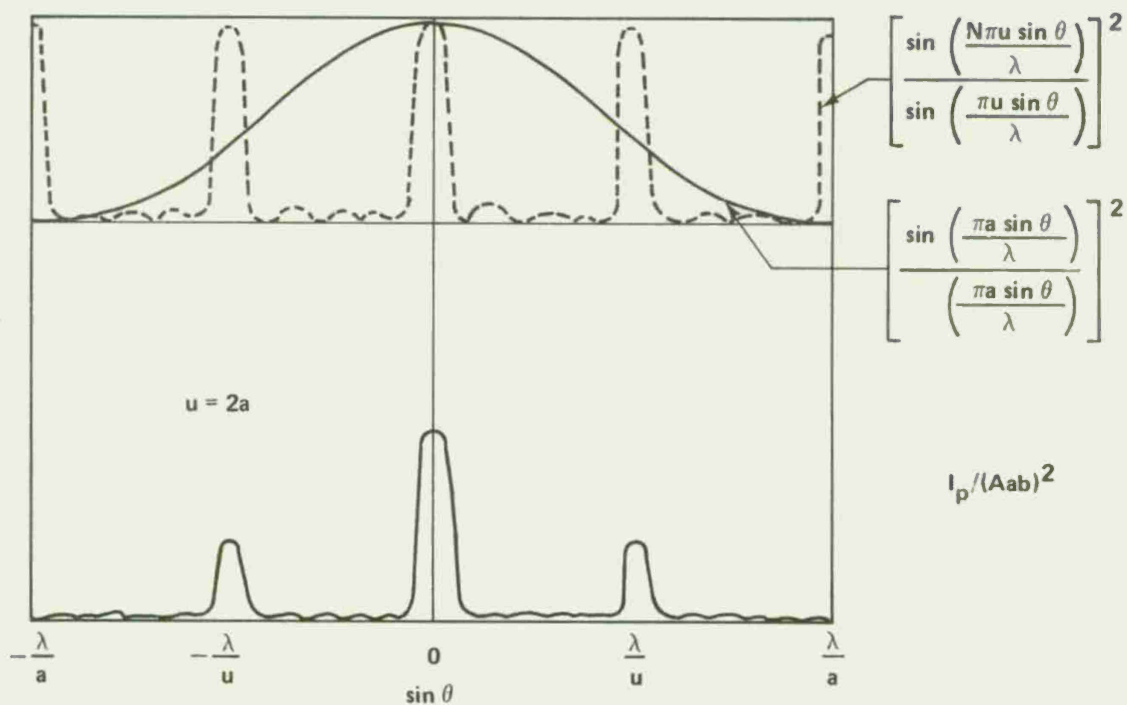


Figure 56. Intensity distribution of multiple apertures.

and the intensity at any point is

$$I_P = (Aab)^2 \left[\frac{\sin \frac{\pi a \sin \theta}{\lambda}}{\frac{\pi a \sin \theta}{\lambda}} \right]^2 \left[\frac{\sin \left(\frac{N\pi u \sin \theta}{\lambda} \right)}{\sin \left(\frac{\pi u \sin \theta}{\lambda} \right)} \right]^2 \quad (48)$$

For the case of $u = 2a$ and $N = 10$, an illustration of Equation (48) is shown in Figure 56. It should be noted that if $u = a$, no fringes will occur; and represents the minimum limiting case for engineering applications. If $u > a$ two or more fringes will be evident on the screen. Now consider the application, if an image is recorded of the speckle pattern on a model made by illumination with a coherent light source, these many speckles are recorded as apertures on the film. When the model is loaded, the speckles (apertures) shift. By double exposing the first film record, a second set of apertures is recorded.

In a small region of the film the second set of apertures is equally spaced relative to the first. The spacing equals the in-plane displacement vector. The out-of-plane displacement effects only the focus of the image and has almost no effect on the aperture spacing. When a coherent light is used to illuminate, the film record in a small region where the in-plane displacements are essentially equal to the projected diffraction pattern intensity is described by Equation (48) or as

$$I_P = C \left[\frac{\sin \frac{\pi a \bar{X}}{\lambda f}}{\frac{\pi a \bar{X}}{\lambda f}} \right]^2 \left[\frac{\sin \frac{N\pi \bar{X}}{\lambda f} u}{\sin \frac{\pi \bar{X} u}{\lambda f}} \right]^2 \quad (49)$$

where

C = a proportionality constant

a = average speckle size

f = lens focal length or distance to the screen

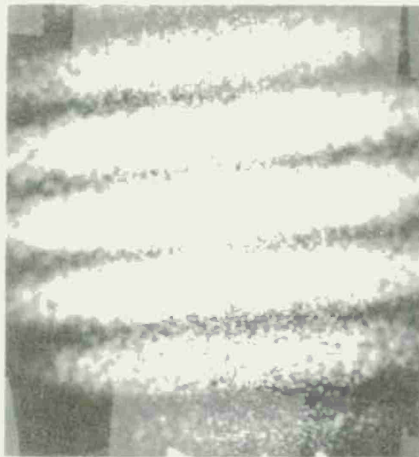
λ = wave length of the light source

\bar{X} = coordinate distance on the screen

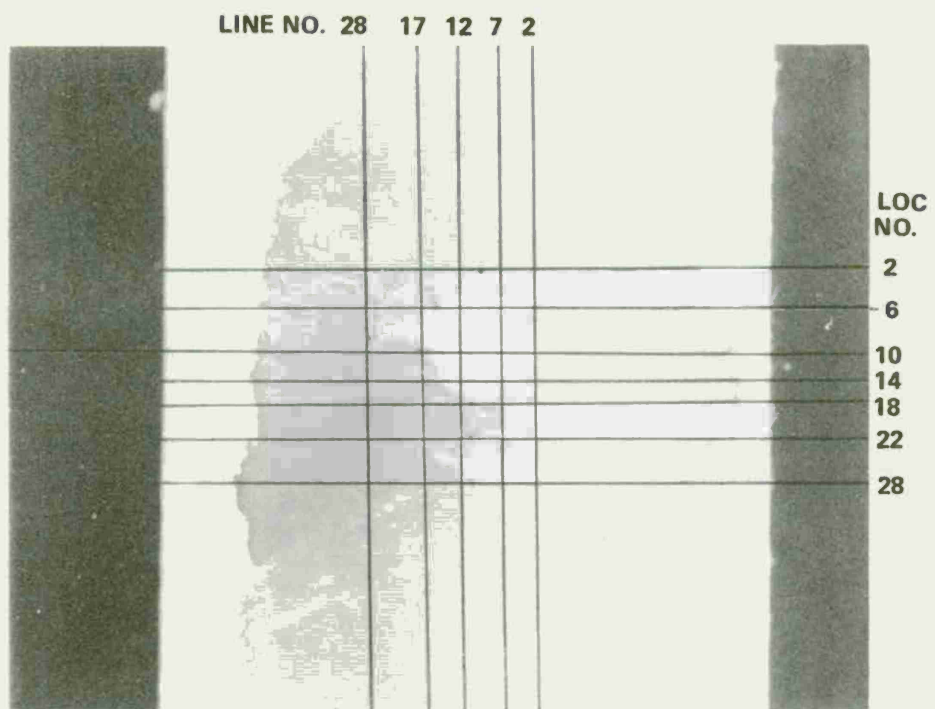
u = in-plane displacement

Maxima occur where

$$u = m_1 \frac{\lambda f}{\bar{X}} \text{ for } m_1 = 0, 1, 2, \dots \quad (50)$$



(a) TYPICAL YOUNG'S FRINGE PROJECTION



(b) GRID SYSTEM

Figure 57. Cylinder with spot flaw and Young's fringes shown with the grid system.

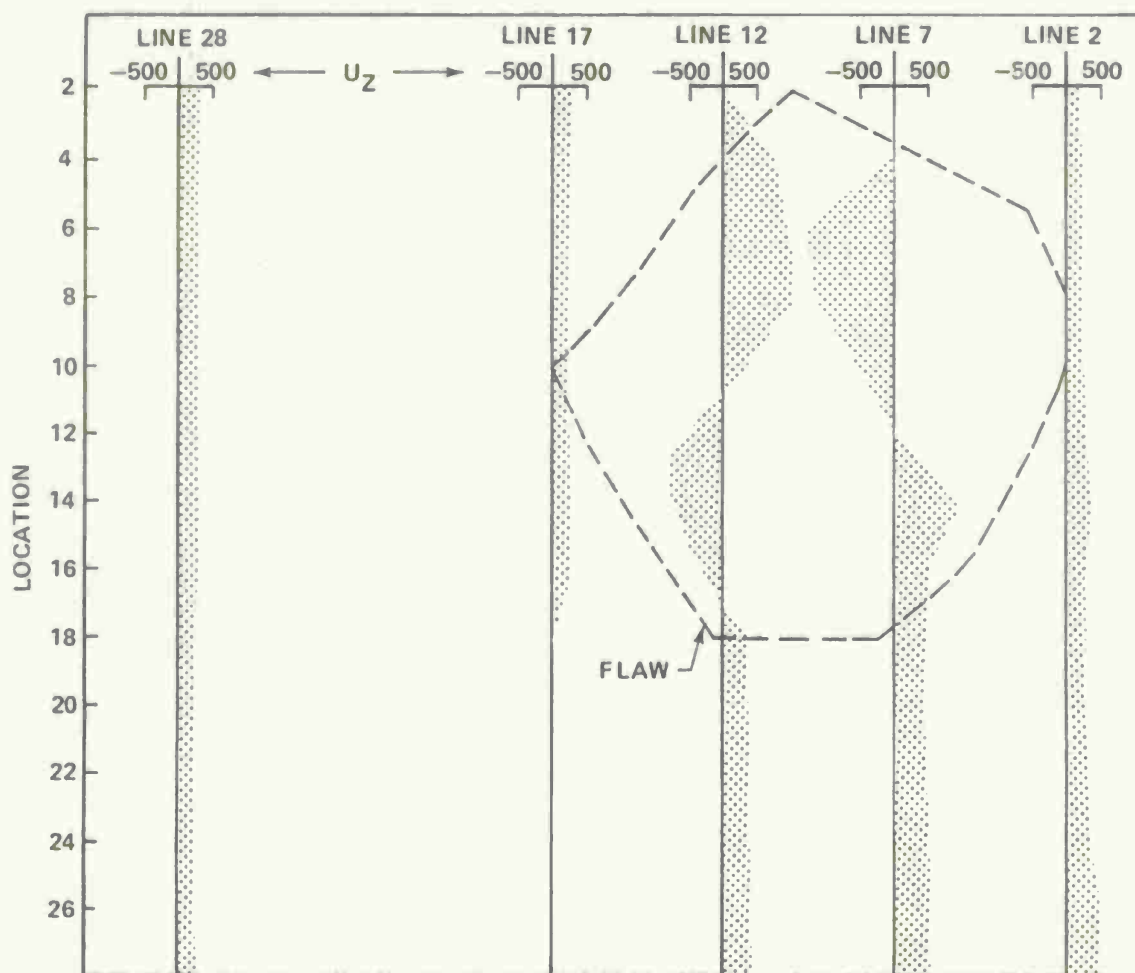


Figure 58. Grid locations versus axial displacements (microinches).

Instead of using the lens focal length to evaluate displacement, the technique works without a lens and the distance f is the distance from the film to the screen.

This speckle technique was applied to flaw detection in composite cylinders. These data are included in Figures 9 and 10. Note that the minimum spacing representing total displacement is 100 microinches. The maximum displacements depend on resolution of the fringes where 20,000

microinches is representative. Because $\sin \theta$ is approximated by $(\frac{\bar{x}}{f})$ the fringe spacing is slightly non-linear.

V. FRINGE DATA ANALYSIS

A double-exposed film record was made of the speckles on the cylinder. The deformation resulted from an internal pressure of 110 psi. The film was processed and placed in a holder in front of a laser beam. A coordinate system was chosen as shown in Figure 57b. The fringes were projected on a screen. Figure 57a shows a typical fringe pattern. The displacement was calculated by Equation (19) for each location along each line and plotted in Figure 58.

The flaw location was evident as can be seen from the plot of Figure 58. At all lines within the flaw the displacement was greater. Only two lines are shown for convenience. In taking the spacing always in the axial direction the normal strain in the axial direction can be calculated and used as an excellent criterion for critical flaws.

Chapter 5. SUMMARY AND CONCLUSIONS

Approximately eighteen fiber reinforced composite cylinders were fabricated in the in-house composite structures facility. Three types of programmed flaws were fabricated into the composite structure. The flaws consisted of delaminations between the fibers and were produced by inserting some teflon tape in a 0.04-inch-thick cylinder wall. This type of flaw corresponds to those resulting from dirt, grease, voids, or flaws being fabricated into the structure. Spot, circumferential and longitudinal flaws were used.

A computer program utilizing conventional finite elements was applied which predicts the surface displacements on the cylinders as a function of pressure loading and flaw geometry for specific composite materials. Computational data that were generated for displacements in the regions of each type flaw. It was determined that a special crack tip element was required to yield acceptable accuracy at the crack tip. A more appropriate element stiffness relation is suggested.

The basic theory for the analysis of the optical holographic fringe patterns was adapted to the specific geometries and boundary conditions for the specimen involved. Equations to reduce the fringe patterns to surface displacements were derived. Test fixtures and apparatus were designed and fabricated. Optical holographic fringe data were taken from specimens of each type with pressure loadings using both the double exposure and real-time methods. Fringe patterns were so sensitive that at certain loadings even the wrap angles of the fibers and the crossover regions were easily detected. Since locations of these points are well known, interference with the detection of flaws is not considered a major problem. The real-time approach is a rapid way of optimizing the loading parameters to best resolve the flaws. Each type flaw was detectable using double-exposure holography and real-time; however, both methods require careful digitization and analysis to quantify the flaws and determine if they are critical.

Software for a PDP-1145 digital computer interfaced with a fringe reader and analyzer was developed and utilized to digitize the film and fringe patterns, plot the fringe density, locate the flaws on the plot, determine the flaw size, and compute the surface strains. The circumferential flaw was the most difficult to detect on the fringe pattern using optical holography.

The theory was derived for the Young's Fringe method and the pattern data were taken for the different flaws. The flaw locations and approximate size were determined by plotting the surface displacements versus surface coordinates. Data taken using shearing speckle interferometry resulted in the best flaw resolution on the circumferential flaw.

In summary, fringe data were taken using both double-exposure and real-time optical holography, Young's Fringe, and shearing-speckle interferometry. The data were reduced by computer and the flaws were detected, located and the approximate flaw size determined. Strains, displacements, or stresses were determined. Very limited experiments were made using the dual-beam speckle interferometry technique. Optical holography yielded the best fringe resolution and the speckle techniques simplified the data reduction to strain.

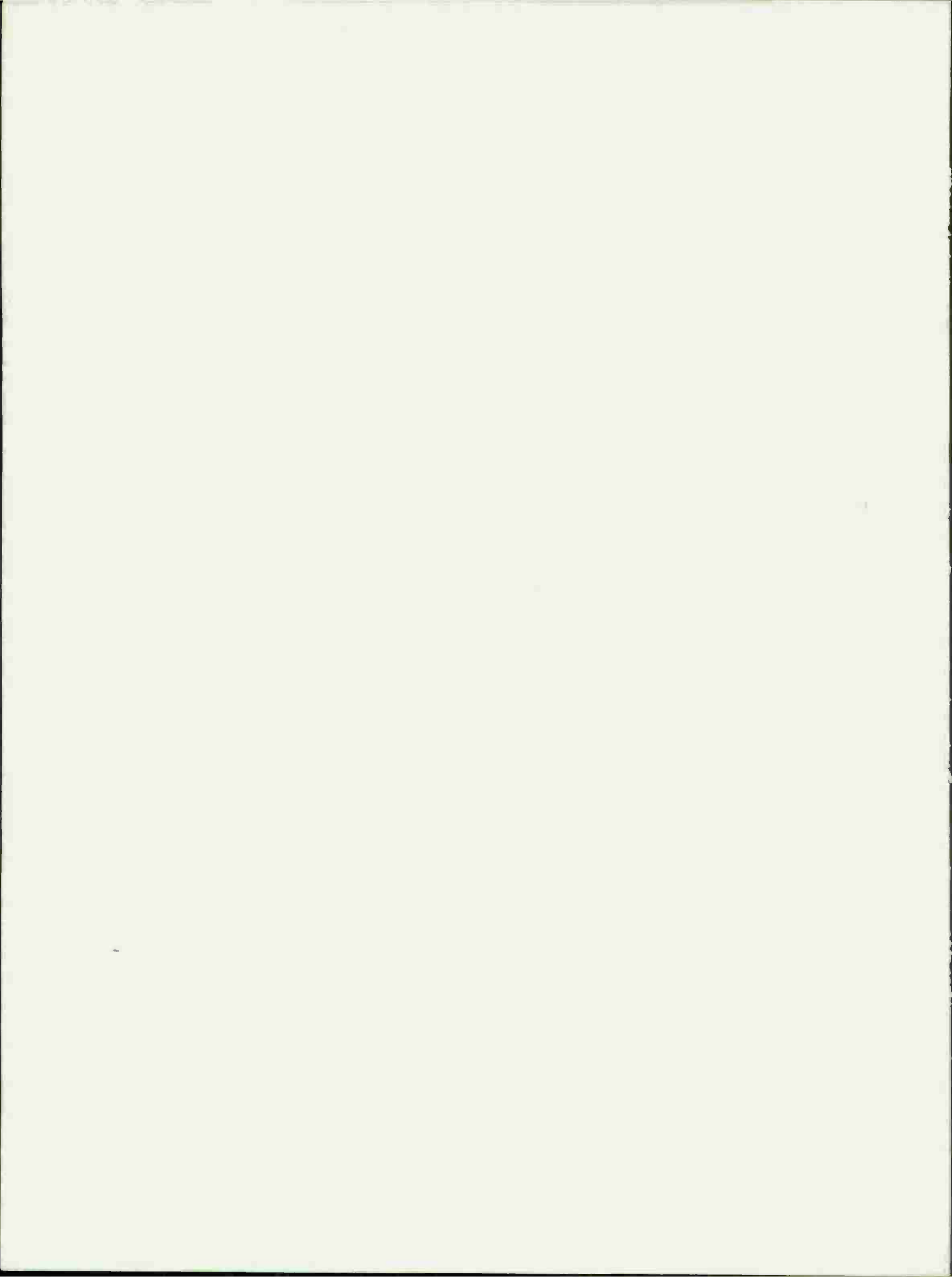
For application at the end of the production line the speckle methods are the most adaptable because they can be easily digitized using a vidicon system with a scan converter interfaced with a computer. The primary problem with the dual-beam is fringe resolution which can be greatly improved through electronic processing. In event the improvement is inadequate it may be necessary to select one of the other techniques with a small automatic film processor in the system.

Chapter 6. PLANS FOR FUTURE RESEARCH

The research presented in this report is being continued as a Manufacturing Methods and Technology program to nondestructively test fiber-reinforced composite launch tubes and motor cases for small missiles. This program is directed toward the development and fabrication of an automated system to test the end items, reduce the fringe data, determine the size and location of flaws and through interfacing with a computer, compute the surface strains and correlate with a failure criterion to accept or reject each item.

Specific tasks planned in the next two years include:

- 1) Development of a special crack-tip finite element to describe the singular behavior in the region of the crack tip.
- 2) Development of an electronic processing technique to enhance the fringe patterns from the dual-beam speckle interferometric methods.
- 3) Design and development of an electronic spatial filtering system for speckle interferometric methods.
- 4) Design and develop a vidicon camera system which consists of a vidicon camera with a control panel interfacing it with a scan convertor and television readout, or input to digital computers.
- 5) Development of techniques to automate and computerize application of the Young's Fringe Speckle Interferometric Techniques.
- 6) Exploration of methods to cover more of the surface of the specimen with each test.
- 7) Elimination of the need for film processing, if practical.
- 8) Development of computer software to reduce the fringe data and perform the strain analysis.



REFERENCES

1. Stetson, K. and Powell, R., "Hologram Interferometry", Journal of the Optical Society of America, Vol. 54, p. 1295, 1964.
2. Brisbane, J. J., Heat Conduction and Stress Analysis of Solid Propellant Rocket Motor Nozzles, Rohm and Haas Company, Redstone Research Laboratories, Huntsville, Alabama, Technical Report S-198; AD 848 594, February 1969.
3. Cost, T. L., Influence of Case-Liner Bond Flaws on Exterior Deformation of Solid Rocket Motor Cases, Athena Engineering Company, Technical Report No. AEC-TR-73-002, April 1973.
4. Leith, E. N. and Upatnieks, J., "Wavefront Reconstruction with Continuous Tone Objects", Journal of the Optical Society of America, Vol. 53, pp. 1377-1381, 1963.
5. Develis, J. B. and Reynolds G. O., Theory and Applications of Holography, Addison-Wesley, 1967.
6. Caufield, H. J. and Lu, Sun, The Applications of Holography, Wiley Interscience, 1970.
7. Collier, R. J., Burchardt, C. B. and Lin, L. H., Optical Holography, Academic Press, 1971.
8. Holloway, D. C. "Holography and its Application to Photoelasticity", M. S. Thesis (TAM REPORT 329), Department of Theoretical and Applied Mechanics, University of Illinois, Urbana, Illinois, (June 1969).
9. Rust, J. B., Miller, L. J. and Margerum, J. D., Polymer Engineering and Science, 9, 40 (1969).
10. Margerum, J. D., Miller, L. J., and Rust, J. B., Photographic Science and Engineering, 12, 177 (1968).
11. Close, D. H., Jacobson, A. D., Margerum, R. G., Brault, J. G., and McClung, F. J., Applied Physics Letters, 14, 159 (1969).
12. Jenny, J. A., Optical Society of America 60, 1155 (1970).
13. Close, D. H., and Jacobson, A. D., Optical Society of America 59, 1529 (1969).

14. Becsey, Julius G. and G. E. Maddux, "The Preparation and Use of A Photopolymer System for Real-Time Holographic Applications", Proceedings of the Air Force Systems Command Science and Engineering Symposium (1973).
15. Marshall, Samuel L., Laser Technology and Applications. New York: McGraw-Hill Book Company, 1969.
16. Jenny, J. A., Optical Society of America 61, 1116 (1971).
17. Ranson, W. F., "Use of Holographic Interferometry to Determine the Surface Displacement Components of a Deformed Body", Ph.D. Thesis (TAM Report 348), Department of Theoretical and Applied Mechanics, University of Illinois, Urbana, Illinois, (August 1971).
18. Archbold, E., Burch, J., Ennos, A., Taylor, D., "Visual Observation of Surface Vibration Nodal Patterns", Nature, 222, 263 (April 1969).
19. Leendertz, J., "Interferometric Displacement Measurement on Scattering Surfaces Utilizing Speckle Effect", Journal of Physics E, 3, 214 (1970).
20. Butters, J., "Laser Holography and Speckle Patterns In Engineering Metrology", Symposium on Advanced Experimental Technology in the Mechanics of Materials, September 1970.
21. Butters, J., Leendertz, J., "A Double Exposure Technique for Speckle Pattern Interferometry", Journal of Physics E, 4, 277 (1971).
22. Hung, Y., Der Hovanesian, J., "Full-field Surface-strain and Displacement Analysis of Three-dimensional Objects by Speckle Interferometry", Experimental Mechanics 12, (10), 454, (October 1972).
23. Cloud, G. L., "Quantitative Speckle-Moire Interferometry" paper presented at the 1973 Fall Meeting of the Society for Experimental Stress Analysis.

DISTRIBUTION

	No. of Copies		No. of Copies
Defense Metals Information Center Battelle Memorial Institute 505 King Avenue Columbus, Ohio 43201	1	Commander Watervliet Arsenal Watervliet, New York 12189	2
Defense Documentation Center Cameron Station Alexandria, Virginia 22314	12	Commander US Army Aviation Systems Command ATTN: DRSV-EE St. Louis, Missouri 63166	1
Commander US Army Foreign Science and Technology Center ATTN: DRXST-SD3 220 Seventh Street, NE Charlottesville, Virginia 22901	1	Commander US Army Aeronautical Depot Maintenance Center (Mail Stop) Corpus Christi, Texas 78403	1
Office of Chief of Research and Development Department of the Army ATTN: DARD-ARS-P Washington, D.C. 20301	1	Commander US Army Test and Evaluation Command ATTN: DRSTE-RA Aberdeen Proving Ground Maryland 21005	1
Commander US Army Electronics Command ATTN: DRSEL-PA-P DRSEL-CT-DT Fort Monmouth, New Jersey 07703	1 1	Commander US Army White Sands Missile Range ATTN: STEWS-AD-L White Sands Missile Range, New Mexico 88002	1
Commander US Army Lattek Laboratories Kansas Street ATTN: STSNLT-EQR Natick, Massachusetts 01760	1	Commander ATTN: STEAP-MT Aberdeen Proving Ground, Maryland 21005	1
Commander US Army Mobility Equipment Research and Development Center Fort Belvoir, Virginia 22060	2	Chief Bureau of Naval Weapons Department of the Navy Washington, D.C. 20390	1
Director USA Mobility Equipment Research and Development Center Coating and Chemical Laboratory ATTN: STSFB-CL Aberdeen Proving Ground, Maryland 21005	1	Chief Bureau of Ships Department of the Navy Washington, D.C. 20315	1
Commander Edgewood Arsenal ATTN: SAREA-TS-A Aberdeen Proving Ground Maryland 21010	1	Naval Research Laboratory ATTN: Dr. M. M. Krafft Code 8430 Washington, D.C. 20375	1
Commander US Army Materiel Command ATTN: DRCQA-V Mr. Smart Alexandria, Virginia 22333	1	Commander Wright Air Development Division ATTN: ASRC Wright-Patterson AFB, Ohio 45433	2
Commander Frankford Arsenal ATTN: SARFA-A2000 SMUFA-T4300 Philadelphia, Pennsylvania 19137	1 1	Director, Army Materials and Mechanics Research Center ATTN: DRXMR-PL DRXMR-M DRXMR-P DRXMR-RA, Mr. F. Valente DRXMR-MD DRXMR-MN, Mr. H. Hatch Watertown, Massachusetts 02172	2 1 1 1 2 1
Commander Picatinny Arsenal ATTN: SARPA-TS-S, Mr. M. Costello Dover, New Jersey 07801	1		
Commander Rock Island Arsenal Research and Development ATTN: 9320 Rock Island, Illinois 61201	1		

	No. of Copies
DRSMI-MS	1
-QLS	2
-FR, Mr. Strickland	1
-R, Dr. McDaniel	1
Dr. Kobler	1
-RK	1
-RT	1
-RE	1
-RG	1
-RFE	1
-RD	1
-RR	2
-RL, Mr. Lewis	1
-RLA, Mr. Pettey	1
-RLT, Dr. Mullinix	25
-RH	1
-RL (Record Set)	1
-RBD	3
-RPR	1
-RC	1

